Quantitative diffusion-weighted J-difference spectroscopy of common brain metabolites.

Master's Thesis

Department of Chemistry,

University of Bergen

Magnus Svensen

December 2021

Supervisor

John Georg Seland

Abstract

The use of magnetic resonance imaging and spectroscopy has become a routine and invaluable diagnostic method for detecting a variety of medical conditions of the human brain, and it is also one of the best tools for understanding the brain's pathways and its other functions. The field of study is in constant development, and particularly with respects to *in vivo* spectroscopy, the aim of which is to allow for non-invasive and efficient profiling of the brain's metabolic profile. The average metabolite concentrations of a healthy brain are known, and there has been found correlations between altered brain metabolite concentrations and neurological diseases. There are a number of challenges to this method. One of which being spectral overlap of metabolite signals. Another is the fact that the brain contains macromolecules (e.g., liposomes) with broad NMR signals which overlap with metabolite signals. There are also problems regarding patient movement, the human skull's magnetic susceptibility, as well as the space between the spectrometer coil and the patient. This thesis explores the use of two diffusion-weighted, J-edited difference spectroscopy techniques to measure the diffusion of important brain metabolites such as GABA, Cr and NAA. The same pulse sequences will be used – without diffusion weighting – to construct calibration curves based on increasing GABA concentration in order to ascertain linear response.

Acknowledgments

I wish to extend my sincerest gratitude to my supervisor John Georg Seland at the Department of Chemistry, University of Bergen. He has invested a lot of time helping me throughout this project, whether through fixing technical issues surrounding the spectrometer, educating me on the vast field of NMR or even spending his free time reviewing my work. Beginning a master's degree in the middle of a global pandemic brought with it its own set of challenges, especially relating to lockdown. Writing at home and being away from my student peers affected my motivation deeply, but with the help from friends & family (especially my mother, siblings and partner), I was able to overcome these troubles and finish a thesis that I am proud of.

Lastly, I would like to dedicate this thesis to the loving memory of my father Yngve. A physics teacher by trade, he inspired me already from a very young age to get into the field of natural science. Thank you for the late nights spent stargazing, at-home physics experiments and for teaching me to how to wonder. This is for you.

Table of contents

List of symbols and abbreviations

MRI – Magnetic Resonance Imaging

MRS – Magnetic Resonance Spectroscopy

NMR – Nuclear Magnetic Resonance

MOI – Metabolites of interest

Cr / tCr – Creatine (metabolite) / total creatine

NAA – *N*-Acetyl-L-aspartic acid (metabolite)

Cho / tCho – Choline (metabolite) / total choline

mIns – *myo*-Inositol (metabolite)

Glu – L-glutamic acid (metabolite)

Lac – L-lactic acid (metabolite)

GABA – γ-Aminobutyric acid (metabolite)

RF – Radiofrequency

$\boldsymbol{B_0}$ – Static magnetic field (+z direction) (Tesla)

$\boldsymbol{B_1}$ – Magnetic field associated with RF pulse (Tesla)

$\boldsymbol{v_0}$ – Larmor frequency (Hz)

$\boldsymbol{v_1}$ – RF radiation frequency (Hz)

CNS – Central Nervous System

Cr – Creatine (metabolite)

$mmol/kg_{ww}$ – millimole per kilogram wet muscle.

DW – Diffusion-weighted(-ing)

VMA – Vector Model Approach

POF – Product Operator Formalism

FID – Free Induction Decay

ROI – Region of interest

MFG – Magnetic Field Gradient

PRESS – Point RESolved Spectroscopy

MEGA-PRESS – MEscher-GArwood-PRESS

PFGSE – Pulsed Field Gradient Spin Echo

Overview of formulas

Overview of tables

Overview of Figures

1 Introduction

1.1 Background

The basic principles of magnetic resonance have been known since 1946 through the work of Purcell et al.[1] and Bloch et al.[2], but it took about 40 years until anyone found a way to employ the technique to perform spectroscopy of the human body due to technical difficulties. MRI technology had become a ground-breaking addition to modern diagnostic methods, but it was limited by its disability to yield metabolic information. This changed around the 90s when NMR software become accessible for personal computers, which in combination with pre-existing NMR hardware made *in vivo* magnetic resonance spectroscopy an easily accessible and viable method of acquiring metabolic information. The earliest studies on *in vivo* MRS focused on measuring ^{31}P involved in tissue metabolism, but this proved to be a disadvantageous method due to the low sensitivity and natural abundance of the ^{31}P-nucleus. Today, ^1H-NMR is by far the most employed spectroscopy mode due to both maximal sensitivity and high natural abundance *in vivo*[3].

In a pioneer study in 1989, Frahm et al.[4] used proton-NMR to measure brain metabolite concentrations *in vivo* of healthy patients, reporting high regional selectivity and measurement accuracy of voxel-based stimulated echo techniques.

"Localized proton NMR spectroscopy has been demonstrated to resolve regional distribution patterns of metabolites in the normal human brain *in-vivo*. Its high sensitivity and relatively short measuring times allow multiple spectroscopic recordings at different echo times and repetition times. NMR relaxation times T_1, and T_2 may indicate dynamical and structural differences in the cellular organization of certain metabolites in different parts of the brain. They also serve to noninvasively determine relative (and absolute) steady-state concentrations."[4]

Since then, a number of studies have shown that, when combined with MRI techniques, NMR is a highly efficient tool for diagnosing pathologies in the human brain. With the help of magnetic field gradients precise regional selectivity may be achieved, which then may reveal regional concentration differences in tissue. This allows for discrimination between healthy tissue and brain tumors[5]. Abnormal metabolite concentrations in various cerebral regions are

also associated with certain neurodegenerative diseases such as Alzheimer's disease[6] or in psychiatric disorders such as schizophrenia[7]. This has led to MRS becoming an area of focus as personalized medicine develops, with the aim being early, non-invasive diagnosis of neuropathologies based on significant deviations in brain metabolite concentrations.

1.2 Brain metabolites

In order to test a pulse sequence's ability to quantify metabolites a phantom solution is prepared using selected metabolites at realistic *in vivo* concentrations[8].

Table 1 - Overview of MOI with in vivo concentrations in the normal human brain

Metabolite	Abbreviation	Molarity (mM)
Creatine	tCr	10,0
Choline	Cho	3,0
N-acetyl-L-aspartatic acid	NAA	12,5
myo-Inositol	m-Ins	7,5
L-glutamic acid	Glu	12,5
L-lactic acid	Lac	5,0
γ-aminobutyric acid	GABA	2,0

Information about the metabolites of interest (MOI) in this thesis is gathered from *The Human Metabolome Database*[9]. Structures are generated in ChemDraw Professional 16.0[10].

Information regarding NMR signals and chemical shifts are gathered from an article by Govindaraju et al. (2000)[11].

1.2.1 – Creatine
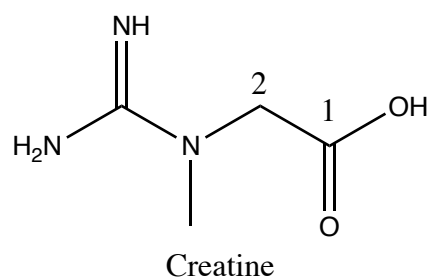
Creatine

Figure 1 - The molecular structure of creatine

Creatine (Cr) is an α-amino acid derivate found in all living organisms. It is involved in various enzymatic reactions in the human body, within which it exists in various forms, such as regular

creatine and phosphocreatine (through the creatine kinase b-type enzymatic reaction). Total creatine content in the brain is reported to be approximately 4,0-5,5 mmol/kg$_{ww}$ for phosphocreatine and 4,8-5,6 mmol/kg$_{ww}$ for free creatine[11]. This is metabolite is obtained at a rate of about 1g per day in an omnivorous diet, and it is taken as a dietary supplement among some athletes. It is a potentially toxic compound that is associated with diseases such as frontotemporal dementia as well as cancers of the colon and pancreas. Although creatine exists in different forms in the brain, the NMR signals are almost identical. Therefore, it is commonplace to measure the total creatine content (tCr) instead of attempting to differentiate between different derivates.

Table 2 - NMR data for creatine

Resonance	Group	Structure	δ (ppm)	*J* (Hz)	Connectivity
H$_A$	$^2CH_2$	s	3,913	None	
H$_C$	N(CH$_3$)	s	3,027	None	
H$_B$	NH	s	6,649	None	
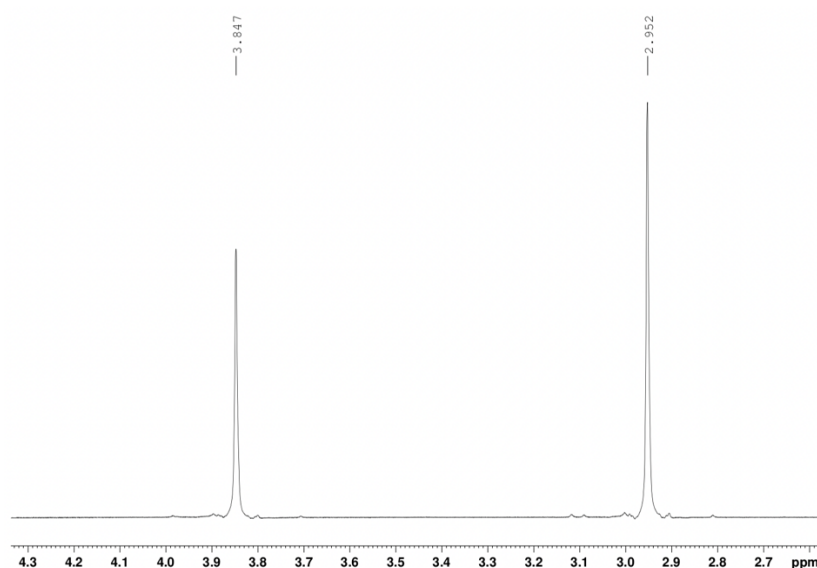
Figure 2 - NMR spectrum of Creatine[8]

1.2.2 – Choline
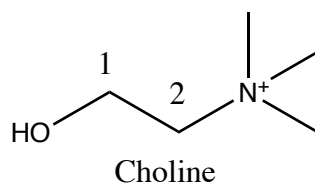
Choline

Figure 3 - The molecular structure of choline

Choline (Cho) exists in the brain as mainly phosphatidylcholine, a component of lecithin, which is found in many plant and animal cells. The reported concentration of choline is about 1-2 mmol/kg$_{ww}$. It is an important precursor to acetylcholine, forming muscarinic acetylcholine receptors in the cholinergic system which controls, e.g., heart rate and memory[12,13]. Other cerebral choline-containing biomolecules include free choline, phosphorylcholine and glycerophoshorylcholine[11]. It is also an important methyl donor and is involved in many lipid metabolic pathways. The human body can biosynthesize small amounts of choline, but primarily obtain the metabolite through ingestion. It is present in dairy products, eggs, peanuts and more. Lack of choline in the diet may lead to fatty liver disease and other liver damage. Low levels of choline are also associated with liver cancer. The Cho *in vivo* signal stems from free choline, phosphorylcholine and glycerophosphorylcholine and is therefore often referred to as total choline (tCho). Phosphatidylcholine is not detected due to its very short T_2 relaxation time[14].

Table 3 - NMR data for choline

Resonance	Group	Structure	δ (ppm)	*J* (Hz)	Connectivity
H$_A$	N(CH$_3$)	s	3,185	None	
H$_B$	^{1}CH$_2$	m	4,054	3,140	1-2
H$_C$	^{2}CH$_2$	m	3,501	6,979	1-2'
				3,168	1'-2'
				7,011	1'-2
				2,572	1-N
				2,681	1'-N
				0,57	N-CH$_3$
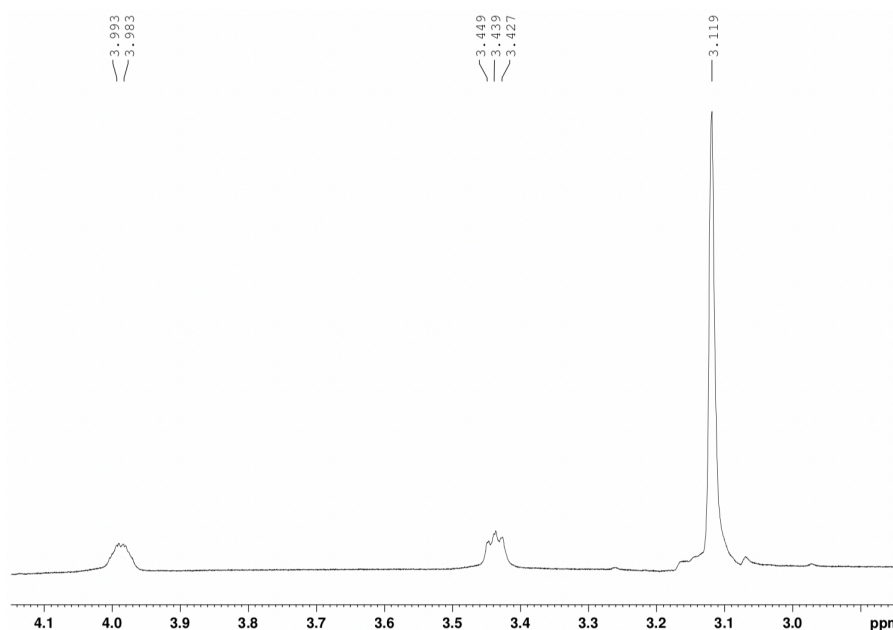
Figure 4 - NMR spectrum of choline[8]

1.2.3 *N*-acetyl-L-aspartatic acid

N-acetyl-L-aspartic acid
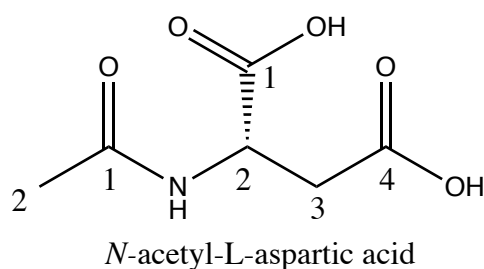
Figure 5 - The molecular structure of N-acetyl-L-aspartic acid

N-acetyl-L-aspartic acid (NAA) is a secondary amide derivate of the amino acid aspartic acid. It is the second most concentrated metabolite in the human brain, preceded only by L-glutamic acid. Its cerebral concentration is reported at $7,0 - 16,0$ mmol/kg$_{ww}$. Biosynthesis of NAA occurs in neural mitochondria by reaction of aspartic acid with acetyl coenzyme A. Therefore, decreased NAA levels are associated with diseases causing loss of neurons such as in glioma, ischemia and degenerative diseases[3]. Its functions in the brain are still being investigated, but it is theorised that NAA is involved as an osmolyte regulating cerebral fluid balance as well as being an important precursor to important neurotransmitters such as *N*-acetylaspartylglutamate (NAAG). Elevated levels of NAA are associated with Canavan disease.

Table 4 - NMR data for NAA

Resonance	Group	Structure	δ (ppm)	J (Hz)	Connectivity
H_A	$^2CH_3$	s	2,008	None	
H_B	^2CH	dd	4,3817	3,861	2-3
H_C	$^3CH_2$	dd	2,6727	-15,592	3-3'
				9,821	2-3'
H_D	NH	d	7,8205	6,400	NH-2
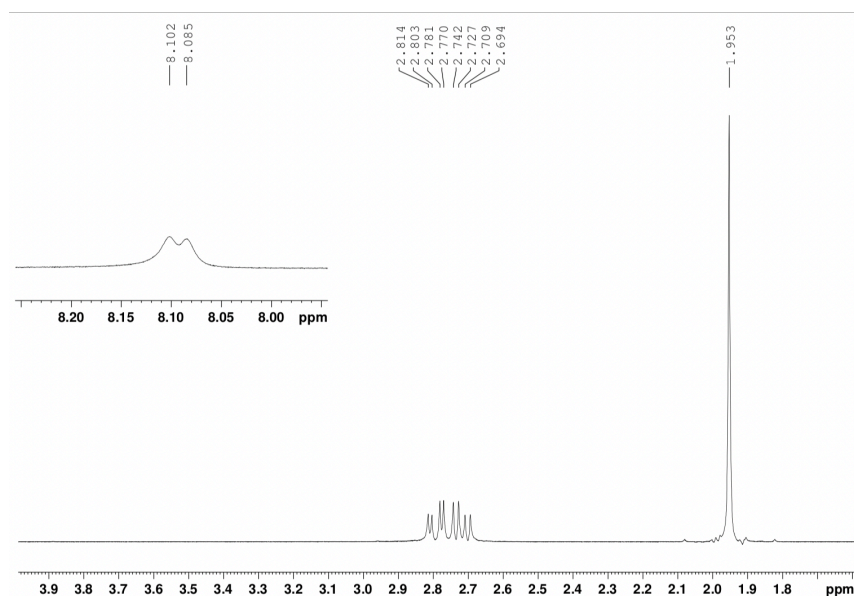
Figure 6 - NMR spectrum of NAA[8]

The H_B-resonance is close to the water resonance and is therefore often affected by water suppression schemes.

1.2.4 – myo-Inositol
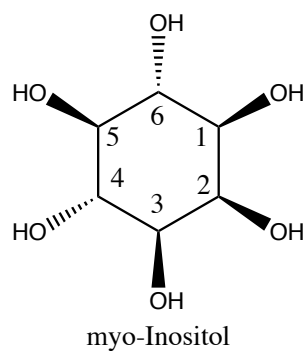
myo-Inositol

Figure 7 - The molecular structure of myo-inositol

Myo-inositol (mIns) is a cyclohexane derivative with a hydroxy group substitution on each of the six carbon atoms. It is therefore also a sugar alcohol. The molecule was previously classified as vitamin B8, but it has since been discovered that the human body biosynthesises mIns from glucose, and as such it can no longer be considered an essential nutrient. mIns exists naturally in many high bran-content cereals. It is an important precursor to secondary messenger molecules such as various inositol phosphates. It is also present in important lipids known as phosphatidylinositols. Normal concentration of mIns in the brain ranges from 4,0 to 8,0 mmol/kg$_{ww}$. Reduced levels of mIns in cerebrospinal fluid are associated with depression, and there has been found significantly reduced levels of mIns in the brains of victims of suicide. The asymmetric stereochemistry present in mIns results in a complex spectrum of several overlapping triplets and doublets of doublets.

Table 5 - NMR data for myo-inositol

Resonance	Group	Structure	δ (ppm)	J (Hz)	Connectivity
H_A	^{1}CH	dd	3,5217	2,889	1-2
H_B	^{2}CH	t	4,0538	9,998	1-6
H_C	^{3}CH	dd	3,5217	3,006	2-3
H_D	^{4}CH	t	3,6144	9,997	3-4
H_E	^{5}CH	t	3,269	9,485	4-5
H_F	^{6}CH	t	3,6144	9,482	5-6
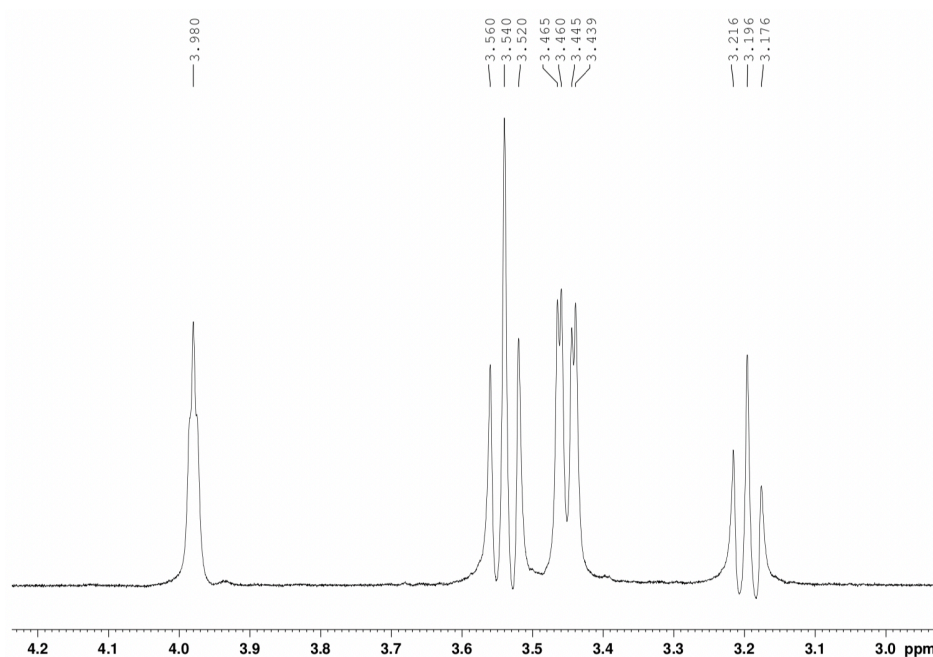
Figure 8 - NMR spectrum of myo-inositol[8]

1.2.5 – L-glutamic acid
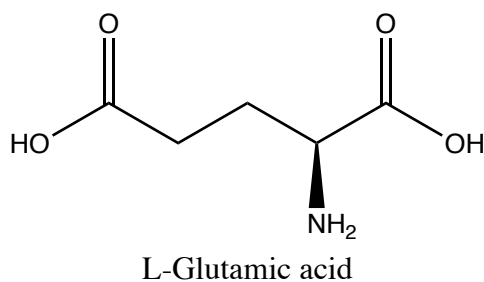
L-Glutamic acid

Figure 9 - The molecular structure of L-glutamic acid

L-glutamic acid (Glu), also referred to by its anion form glutamate, is a non-essential amino acid, meaning that it is produced in the human body. It is an important part of cellular metabolism, being the fastest and most plentiful neurotransmitter in the human nervous system, as well as in other mammals. Glu is theorised to serve an important function in cognitive functions such as memory and learning. It is involved in many brain diseases since so-called glutamate transporters in neuronal and glial membranes – which usually remove Glu from extracellular space – may malfunction and cause Glu to accumulate instead, which leads to neuronal damage and cell death (excitotoxicity). Glu accumulation in the extracellular space is associated with diseases such as stroke, amyotrophic lateral sclerosis and Alzheimer's disease. The metabolite is also implicated in epileptic seizures. Glu and NAA form *N*-acetylaspartylglutamate (NAAG) through a reaction mediated by NAAG synthetase. This

metabolite is largely present in the brain and has many overlapping signals with NAA and Glu, but it is not of interest in this thesis. Glu is present in the brain at a concentration of approximately 12 mmol/kg$_{ww}$.

Table 6 - NMR data for L-Glutamic acid

Resonance	Group	Structure	δ (ppm)	*J* (Hz)	Connectivity
H$_A$	^{2}CH	dd	3,7433	7,331	2-3
H$_B$	^{3}CH$_2$	m	2,0375	4,651	2-3'
			2,12	-14,849	3-3'
H$_C$	^{4}CH$_2$	m	2,3378	8,406	3-4'
			2,352	6,875	3'-4'
				6,413	3-4
				8,478	3'-4
				-15,915	4-4'
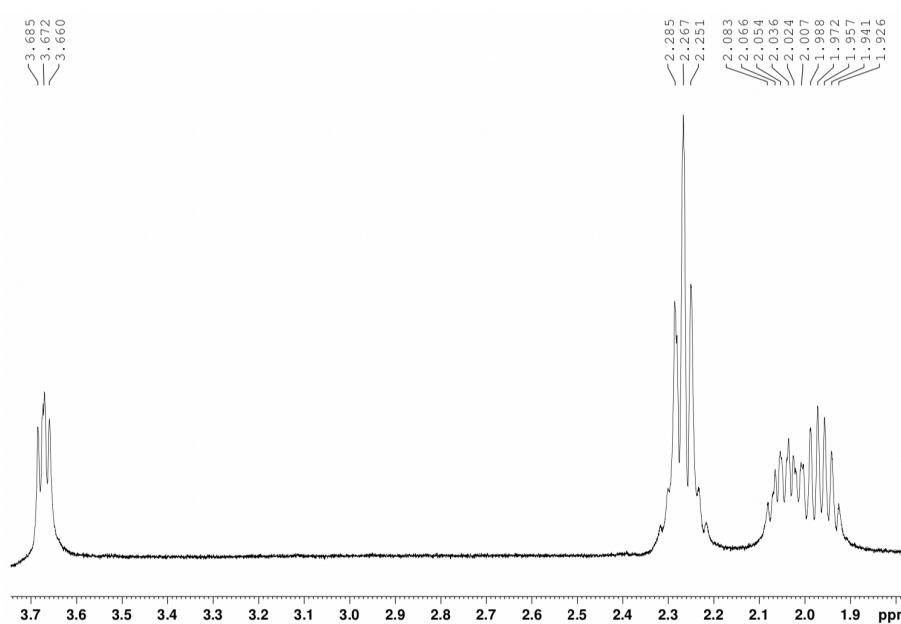
Figure 10 - NMR spectrum of L-Glutamic acid[8]

1.2.6 – L-Lactic acid
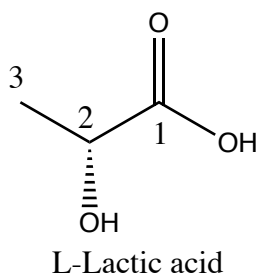
L-Lactic acid

Figure 11 - The molecular structure of L-lactic acid

Lactic acid (Lac) is an organic acid and exists in nature mainly as a product of fermentation. It has two optical isomers, with the laevorotatory isomer being the most abundant in organisms. In the human body lactic acid formation is experienced as an uncomfortable sensation in the muscles during exercise. During anaerobic glycolysis, glucose molecules are oxidised to a lower extent, and pyruvate is formed instead, which then forms converts to lactate. L-lactic acid is also be present in the brain at a concentration of ca. 1 mmol/L (usually non-detectable *in vivo*) in healthy cerebral tissue[15], where abnormal concentrations is a sign of disease such as hypoxia and tumours. Chronically high levels of serum L-lactate levels are a sign of various metabolism-related diseases. It is a rather difficult metabolite to quantify for mainly two reasons; the first being the quartet lying close to the water resonance at 4,7 ppm, which may interfere with the signal. The second challenge is that the doublet at ~1,3 ppm is sufficiently far away from the chemical shift range targeted by shift-selective pulses that it experiences a weaker RF field compared to what is desired in a pulse sequence.

Table 7 - NMR data for lactate

Resonance	Group	Structure	δ (ppm)	*J* (Hz)	Connectivity
H_A	^2CH	q	4,0974	6,933	2-3
H_B	$^3CH_3$	d	1,3142		
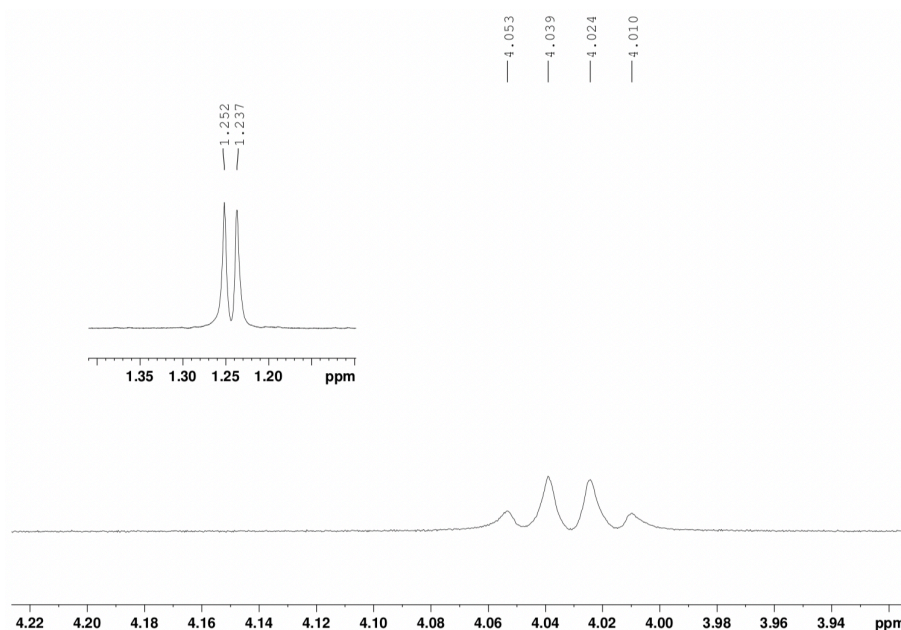
Figure 12 - NMR spectrum of lactate[8]

1.2.7 – γ-aminobutyric acid (GABA)

gamma-Aminobutyric acid
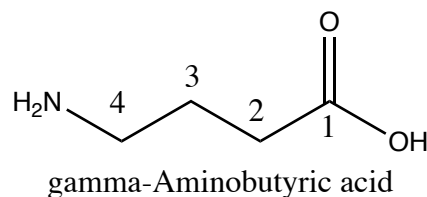
Figure 13 - The molecular structure of gamma-aminobutyric acid

γ-Aminobutyric acid, commonly referred to as GABA, is the chief inhibitory neurotransmitter of the human CNS as well as that of other vertebrates. Its main function is binding to transmembrane receptors in neurons that facilitate transfer of chloride ions into the cells, and potassium ions out of the cell. In short, GABA inhibits electrical impulses (thus, regulating neurotransmitter release) in the brain by creating a net charge across the neuronal cell membrane. Many psychoactive medications such as benzodiazepines and barbiturates act on certain GABA-receptors. These medications act by stimulating GABA receptors to reduce neuronal excitability, therefore acting as anxiolytics. GABA is associated with fear arousal, a chief symptom of anxiety, panic disorders and acute stress syndrome. The metabolite is synthesised from L-glutamic acid in the brain. The GABA concentration in the brain is approximately 1 mmol/kg$_{ww}$. Abnormally low concentrations are found in CSF and in the brain of patients suffering from epilepsy, and in the serum of patients with depression and other mood disorders.

Table 8 - NMR data for GABA

Resonance	Group	Structure	δ (ppm)	J (Hz)	Connectivity
HA	$^2CH2$	m	3,0128	5,732	2-3
				7,127	2-3'
HB	$^3CH_2$	qu	1,8890	10,578	2'-3
				6,982	2'-3'
HC	$^4CH_2$	t	2,2840	7,755	3-4
				7,432	3-4'
				6,173	3'-4
				7,933	3'-4'
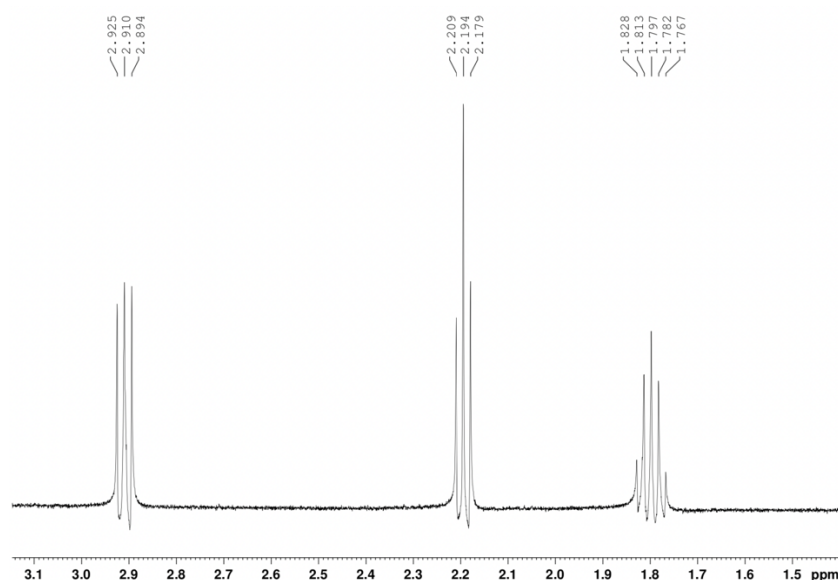
Figure 14 - NMR spectrum of GABA

GABA is hard to quantify *in vivo* due to signal overlap with other metabolites, combined with its low abundance in the brain. The H_B resonance overlaps with NAA at 1,8-2,0 ppm, and is often seen as a "shoulder" on the intense NAA singlet. The H_C resonance overlaps with the H_C resonance of Glu, and H_A overlaps with the H_A resonance of Cr. Because of the challenges caused by spectral overlap, J-edited difference spectroscopy is used to measure GABA, most commonly at the H_A resonance.

1.3 – Localised spectroscopy

When studying the metabolomics of the brain, it is very useful to be able to measure local variations in concentrations, as this is often associated with disease. Therefore, techniques

which combine MRI and MRS have been developed to perform such a localised measurement. Experiments involving localised spectroscopy started in the late 80s. Frahm et al.[4] obtained spectra from specific areas of the brain in healthy volunteers using a single-shot stimulated echo sequence with in-built gradient-enabled spatial localisation (Stimulated Echo Acquisition Mode, or STEAM). The patients' brains were scanned prior to acquisition using an MRI technique (FLASH; Fast Low Angle Shot). Using this image, the volumes of interest (VOI) – the areas giving rise to the NMR signal – were selected and set to 27 ml ($3\times3\times3$ cm^3) and 64 ml ($4\times4\times4$ cm^3). Frahm et al. were able to successfully obtain an *in vivo* metabolite spectrum while suppressing outside signals, thus allowing for quantitative analysis of metabolite concentrations in the chosen areas of the brain.

A few years prior, another single-shot method employing a spin echo (PRESS; Point RESolved Spectroscopy) was developed[16]. STEAM is preferential when measuring coupled metabolites with short T_2-times because shorter echo times (TE) may be used, and water suppression schemes do not cause an increase in TE[17], but the STEAM-generated stimulated echo is only half the amplitude of a PRESS-generated spin-echo (i.e., STEAM generates 50% of the signal PRESS does).

1.4 – J-edited difference spectroscopy

Because metabolite signals of MOI such as GABA overlap with signals from other signals (i.e., tCr, Glu), the PRESS sequence was modified to allow for spectral editing. In the so-called MEGA-PRESS (MEscher-GArwood Point RESolved Spectroscopy)[18] two separate experiments are run: one with chemical-shift selective pulses and one without. Overlapping signals are removed by spectral subtraction.

1.5 – Diffusion-weighting

Certain metabolites are, ideally, compartmentalised in specific cellular- or subcellular structures. Thus, their diffusivity is affected, and this may be measured by diffusion-weighted MRS (DW-MRS). DW-MRS combines magnetic field gradients which sensitise the acquisition to diffusion with localised spectroscopy to give detailed information about the compartmentalisation of metabolites in tissue. Thus, the method can give valuable information in research of cerebral structure as well as in diagnoses. Measurements of the diffusivity of metabolites in relation to their compartmentalisation have been done[19–23]. However, there has

been very little research focussing on measuring the diffusivity of GABA based on the J-editing schemes proposed in this thesis.[23]

Magnetic Resonance Imaging (MRI) has become a routine diagnostic technique for the detection of various diseases (e.g., cancer, multiple sclerosis, internal haemorrhaging etc.). The technique is special in the sense that it employs hundreds of different sequences, each tailored for specific purposes, to provide detailed information of biological systems in a non-invasive manner (compared to other methods like biopsies and exploratory surgeries). In other industries, chemists employ NMR as a tool for perfect structural elucidation. Magnetic resonance techniques are an invaluable tool to any analytical chemist because it provides the foundation for both qualitative and quantitative analyses. As personalized medicine develops the field requires sophisticated methods for determining characteristic signal molecules to aid in diagnosing various pathologies.

2 Theory[24,25]

2.0.1 Different approaches to NMR theory

The topic of nuclear magnetic resonance may be approached in two different manners, depending on the required complexity and rigor of explanation. For the simplest one-dimensional pulse sequences, the classical vector model approach (VMA) is sufficient. VMA uses combines a minimal amount of quantum mechanics with classical physics to depict nuclear spin properties as Cartesian vectors. For more complex, higher-dimension experiments, the vector model becomes limited in the sense that it cannot sufficiently express the necessary quantum mechanical terms with Cartesian vectors. Instead, the product operator formalism (POF) method is employed. The POF approach uses more complex quantum mechanical calculations in tandem with trigonometry to derive all necessary information from the spin's wavefunctions. A brief introduction to NMR using both VMA and POF will be given, as both will be used for different purposes in this thesis.

2.1 – The Vector Model

The vector model approach expresses nuclear spins as the vector sum of all magnetic moments within a system. It visualises the system's response to perturbations in the form of *pulses* as moving vectors in a Cartesian coordinate system. It is easier to grasp visually than POF while

also requiring less calculations, but it is not sufficient for fully describing coupled spin systems, especially in the presence of antiphase- or double-quantum coherence.

2.1.1 – Motion in a circle, phase and the rotating coordinate frame.

In the VMA, the nuclear spins are described as vectors rotating in Cartesian coordinate system. Thus, it is prudent to explain the behaviour of such a scenario. The motion of the vector as it precesses about the z-axis may be defined by two trigonometric functions. The vector component's projections onto the xy-plane will oscillate with time as sine and cosine functions of the form:

$$M_x = r \cos \theta \qquad M_y = r \sin \theta$$

Equation 1 - Magnetisation vector projection on the xy-plane

where r, the radius, is equal to the length of the magnetisation vector M_0, and θ is the angle the vector has moved during a given time interval.
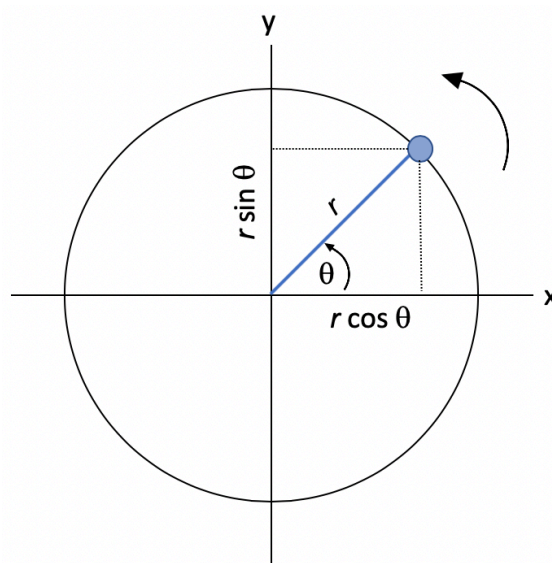
Figure 15 – Motion in a circle

The precessional frequency is defined as the time it takes for the vector to complete a movement of 2π. Note that it may be defined in either [rad s^{-1}] or in Hz, depending on what is more useful.

$$\omega = \frac{2\pi}{T} [rad \ s^{-1}] \qquad \nu = \frac{\omega}{2\pi} [Hz]$$

Equation 2 - Precessional frequency

Therefore, the angle θ may also be expressed as ωt. As the vector precesses over time, it will acquire a phase Φ. This phase may be represented similarly to θ in **Fig. 15**, but by representing the *x*- and *y*-coordinates as real and imaginary, respectively.
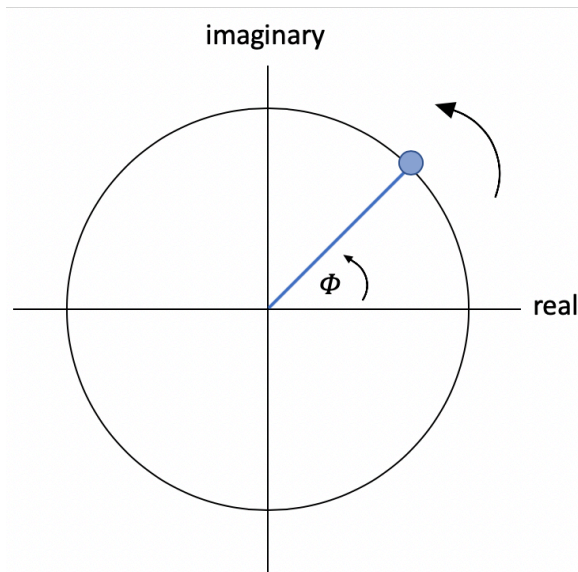
Figure 16 - The phase angle

Accounting for phase in **Eq. 2** yields so-called phase-modulated equations:

$$M_x = r\cos(\omega t + \Phi) \qquad M_y = r\, i \sin(\omega t + \Phi)$$

Equation 3 - Phase modulated precessional frequency

Using Euler's theorem, the vector's position may be expressed as a complex function:

$$\cos\theta + i\sin\theta \equiv \exp i\theta \implies M_x + M_y = r\exp(i\omega t + \Phi) = r\exp(i\omega t)\exp(\Phi)$$

Equation 4 - Vector projection onto xy-plane expressed as a complex function

In the VMA approach, spin vector illustrations are used frequently. If one were to account for the oscillating nature of these vectors, illustrations would be rather complicated. Therefore, spins are represented in a *rotating coordinate system*, marked with primed coordinates. The *x'*- and *y'*-coordinates are rotating *with* the Larmor frequency, so that spins with the same precession frequency appear static. The rotating coordinate frame will be employed in this thesis to discuss NMR pulse sequences.

2.1.2 - The nuclear spin

Most nuclei possess a nuclear angular momentum P which, according to classical physics, is assumed to be spherical, and rotating about an axis. This angular momentum is quantized:

$$P = \sqrt{I(I+1)}\,\hbar$$

Equation 5 – Quantization of nuclear angular momentum

Here I is the angular momentum quantum number. For spin ½ nuclei (e.g., ^{1}H, ^{13}C, ^{15}N), this number equals ½. Because nuclei carry a charge, a net magnetic moment μ will be generated:

$$\mu = \gamma P$$

Equation 6 - Microscopic magnetic moment

Here γ is the gyromagnetic ratio, a nucleus-specific constant describing the ratio between a nuclear spin's angular- and magnetic moments. It follows that μ is also quantized:

$$\mu = \gamma \sqrt{I(I+1)}\hbar$$

Equation 7 - Quantization of magnetic moments

2.1.3 - Directional quantization, energy levels and the resonance condition

The distribution of nuclear spins in a sample under standard conditions is completely random, so that there is zero average direction of any spin vector sum. Magnetic resonance, at its core, relies on the fact that nuclei with an intrinsic spin have a slight tendency to orient themselves along an externally applied magnetic field with flux density B_0 so that their angular momentum z-component P_z is an integral – or half-integral – multiple of $\hbar$. In other words, nuclear spins placed in a magnetic field with flux density B_0 become *directionally quantized* parallel to the direction of the field.

$$P_z = m\,\hbar \iff \mu_z = m\,\gamma\,\hbar$$

Equation 8 - Directional quantization of nuclear spins

Here the directional quantum number m = I, I-1, …., -I. There are (2I +1) possible values for m, meaning that a spin ½ nucleus will have two available values corresponding to + ½ (α) and −½ (β). Classical mechanics express the energy of a magnetic dipole in a magnetic field with flux density B_0 as:

$$E = -\mu_z\,B_0 = -m\,\gamma\,\hbar\,B_0$$

Equation 9 - The energy of a magnetic dipole in magnetic field B0

It follows that the energy difference between two adjacent energy levels α and β is:

$$\Delta E = E_\beta - E_\alpha = \gamma\,\hbar\,B_0$$

Equation 10 - Nuclear spin energy difference between adjacent levels

It has been shown that nuclear spins may populate one of two energy states, α and β. Although it is impossible to determine the exact number of spins populating either state at any given time, molecular thermodynamics state that the *most probable* equilibrium spin distribution at such time is expressed by Boltzmann's law:

$$\frac{n_\alpha}{n_\beta} = e^{-\frac{(E_\beta - E_\alpha)}{k_B T}} = e^{-\frac{\Delta E_{\alpha\beta}}{k_B T}} \approx 1 - \frac{\gamma \hbar B_0}{k_B T}$$

Equation 11 - Boltzmann distribution of spins

where k_B is the Boltzmann constant.

This distribution shows that there is a slight surplus of spins populating the α state when the system is in equilibrium. It follows that this slight surplus is aligned parallel to B_0 (+z). It is important to note that this distribution changes when the system is not in equilibrium, and that the surplus is in the parts per million (ppm) range.

Magnetic resonance techniques work because bursts of high-powered radiofrequency (RF) waves with frequencies corresponding to ν_0 interact with the magnetic moments, causing $\alpha \rightarrow \beta$ transitions. This is called the *resonance condition.* The emitted energy following the corresponding relaxation gives rise to spectral lines on the NMR spectrum. Only transitions which involve a transition of $\Delta m = \pm 1$ are permitted and will show on the spectrum.
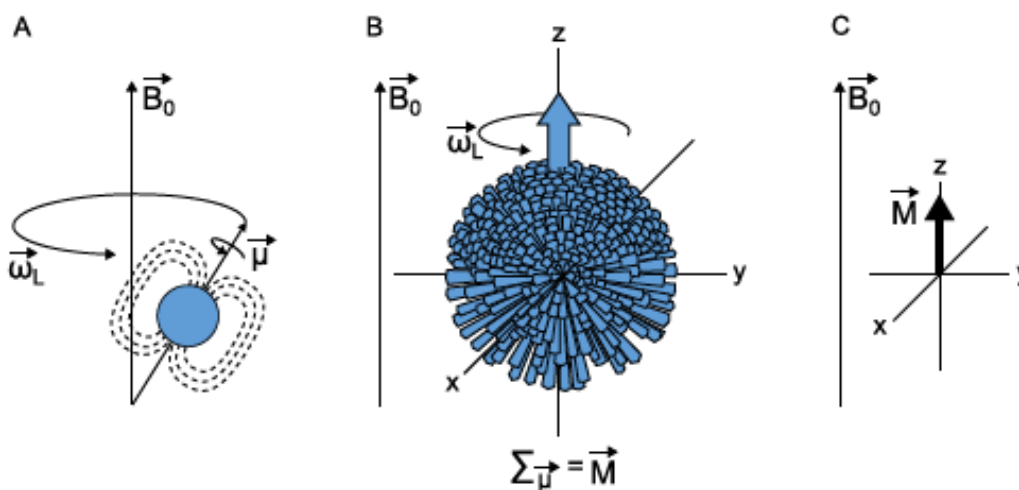
Figure 17 - Directional quantization of spins precessing about B₀

(A) A single spin with magnetic moment μ precessing around B₀. (B) Macroscopic example of spins showing a tendency to align with B₀ to form (C) the bulk magnetisation.[26]

The figure above shows three representations of the magnetisation along the $\boldsymbol{B_0}$-field. The leftmost representation shows the microscopic magnetic moment $\boldsymbol{\mu}$ is precessing around $\boldsymbol{B_0}$ with a frequency $\boldsymbol{\omega_L}$. In a rotating frame of reference this motion is described as:

$$\frac{d\vec{\mu}}{dt} = \vec{\mu} \times (\gamma \vec{B}_0 + \vec{\omega})$$

Equation 12 - Microscopic magnetisation moments precessing around a static magnetic field

In real systems there are many spins. The summation of each magnetic moment generates a macroscopic *bulk magnetisation M_0* oriented parallel to $\boldsymbol{z}$ ($P_z = |\tfrac{1}{2}\boldsymbol{\hbar}|$). This bulk magnetisation may be thought of as a magnetic field precessing parallel to $\boldsymbol{B_0}$ at the Larmor frequency ($\boldsymbol{\omega}$).

$$\frac{d\vec{M}}{dt} = \vec{M} \times (\gamma \vec{B}_0 + \vec{\omega})$$

Equation 13 - Macroscopic magnetisation moments precessing around a static magnetic field

If one defines the Larmor frequency as $-\boldsymbol{\gamma B_0}$, $\frac{d\vec{M}}{dt} = 0$, meaning that:

$$\omega_L = -\gamma B_0 \,(rad) \Leftrightarrow \nu_0 = \left|\frac{\gamma}{2\pi}\right| B_0 \,(Hz)$$

Equation 14 - The Larmor equation in expressed in Hz

Note that the Larmor frequency may be converted to radians (ω_L) by multiplying the term by 2π.

2.1.4 –The RF field and flip angles.

NMR signal detection happens in the *xy*-plane, and $\boldsymbol{M_0}$ must therefore be flipped away from its equilibrium orientation precessing around $\boldsymbol{B_0}$. This is achieved by applying an RF field $\boldsymbol{B_1}$ orthogonally to $\boldsymbol{B_0}$. The $\boldsymbol{B_1}$ magnetic field may be described as two vectors $\boldsymbol{B_1^+}$ and $\boldsymbol{B_1^-}$. The effect of the pulse is that $\boldsymbol{M_0}$ orients itself along it, causing the bulk magnetisation to leave equilibrium magnetisation and enter the transverse plane.

$$\frac{d\vec{M}}{dt} = \vec{M} \times \gamma \vec{B}_1$$

Equation 15 - The bulk magnetisation's orientation around B_1
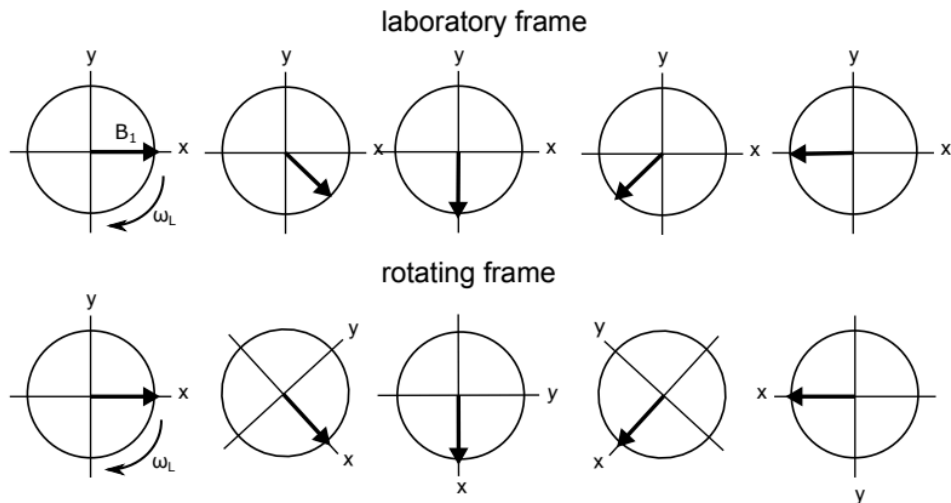
Figure 18 - The motion of B_1 shown in the laboratory frame and the rotating frame of reference

The other B_1-vector is simply rotating counter-clockwise and need not be considered.

B_1 is applied, most commonly, from the **+x** direction. The bulk magnetisation is drawn towards *-y*. The angle by which **M_0** is drawn towards *-y* depends on the *pulse angle, θ,* which is defined as follows:

$$\theta = \gamma \, B_{1i} \, \tau_p$$

Equation 16 - The pulse angle

The desired pulse angle may be achieved by modifying either the field strength (**B_{1i}**), or the duration of the applied pulse (pulse width), **τ_p**. Because the signal varies with (sin *θ*), the positive and negative signal maxima are found at *θ* = (π/2) and (3π/2) (sin = 1, -1). Furthermore, flip angles of π and 2π (sin *θ* = 0) place the bulk magnetisation along *-z* and *+z*, respectively. In these cases, no signal is achieved.
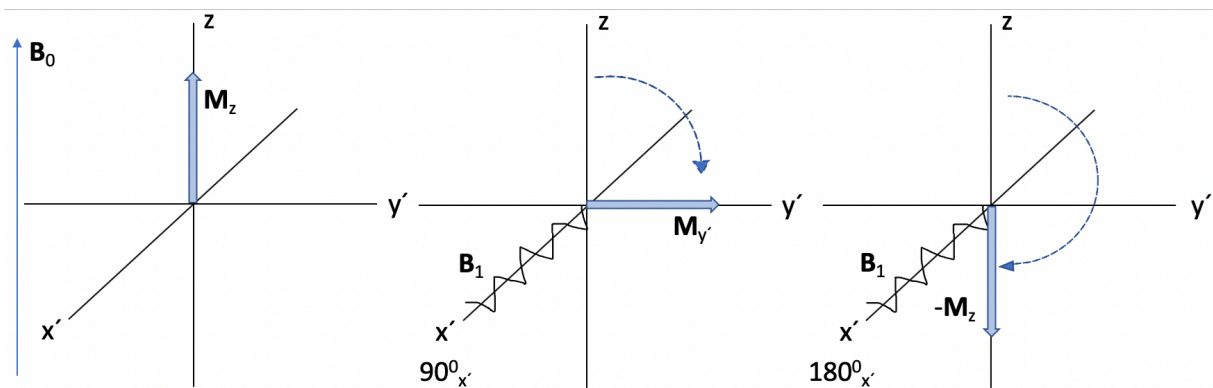
Figure 19 - Change to the bulk magnetisation following Θ = 90°x' and Θ =180°x' pulses. [8]

2.1.5 - Relaxation Mechanisms

By looking at the raw signal acquired in NMR experiments – called the *Free Induction Decay* (FID) – one notices a steep drop in signal as a function of time. This is owed to the fact that excited spins undergo relaxation to return to thermal equilibrium. In other spectroscopic methods, relaxation is often of lesser interest because the process usually happens too quickly for it to be associated with any meaningful information. In NMR, however, as the protons are shielded by an electron cloud, the spins can have very long lifetimes in excited states, allowing the chemist to manipulate the relaxation processes in pulsed NMR experiments. In NMR, the relaxation process is split into two different types, T_1 and T_2, and they are explained by a well-known set of equations known as the Bloch-equations.

$$\frac{dM_x}{dt} = -\frac{dM_x}{T_2}, \qquad \frac{dM_y}{dt} = -\frac{dM_y}{T_2}, \qquad \frac{dM_z}{dt} = -\frac{M_0 - M_z}{T_1}$$

Equation 17 - The Bloch Equations

M_x, M_y and M_z are the xyz-components of the bulk magnetisation

T_1-relaxation, also called spin-lattice relaxation, can be viewed as the restoration of z-magnetisation; that is, the time it takes for a system to return to thermal equilibrium. This is achieved by exchange of energy between excited spins and the 'lattice' (surroundings). This loss of information is irreversible. T_1 depends on many factors, but most importantly on the size of the molecule in which spins have been excited. As a general rule, T_1 is inversely proportional to molecular size, as molecular movement speed greatly affects the rate for dipole-dipole interactions which lead to the transfer of energy and subsequent loss of information in the system. The definition of T_1 is given by the Bloch equation for M_z.

$$M_z = M_0(1 - e^{-\frac{t}{T_1}})$$

Equation 18 - T_1-relaxation

T_2-relaxation, also called spin-spin relaxation, encompasses the reduction of transverse magnetisation caused by loss of phase coherence. The bulk magnetisation is represented as a singular vector $\boldsymbol{M_0}$, which may give the impression that all spins are pointing in the direction of the vector. However, the vector simply represents a small majority of spins in the system that point in a direction parallel to the vector, i.e., the vector represents the net sum of many spins bundled together. Immediately following excitation – for simplicity's sake, a 90° pulse – the spins that form $\boldsymbol{M_0}$ are all bundled together, precessing with frequency $\boldsymbol{v_0}$. In this state, the spins

are all in phase; a phase coherence is established. However, as time T_2 develops, these bundled spins start to fan out; the spins start to lose phase coherence. Eventually, all phase coherence is lost, and there is no longer an observable net magnetisation.

The relaxation process is explained by solving the Bloch equations for M_{xy}.

$$M_{xy} = M_0 e^{-\frac{t}{T_2}}$$

Equation 19 - T₂ relaxation

T_2 is often represented as $T_2{}^*$ because it may be split into two parts: reversible and irreversible. The irreversible dephasing happens as a result of spins interacting with each other, while the reversible dephasing occurs due to magnetic field inhomogeneity. The spin-spin relaxation process is of the most interest in this project as the process is partly reversible as opposed to T_1. Due to its reversible nature, signal loss due to T_2-relaxation may be eliminated through clever use of RF pulses in so-called *spin-echo sequences*.

$$T_2^* = \frac{1}{T_2} + \gamma \Delta B_0$$

Equation 20 - T₂* - relaxation
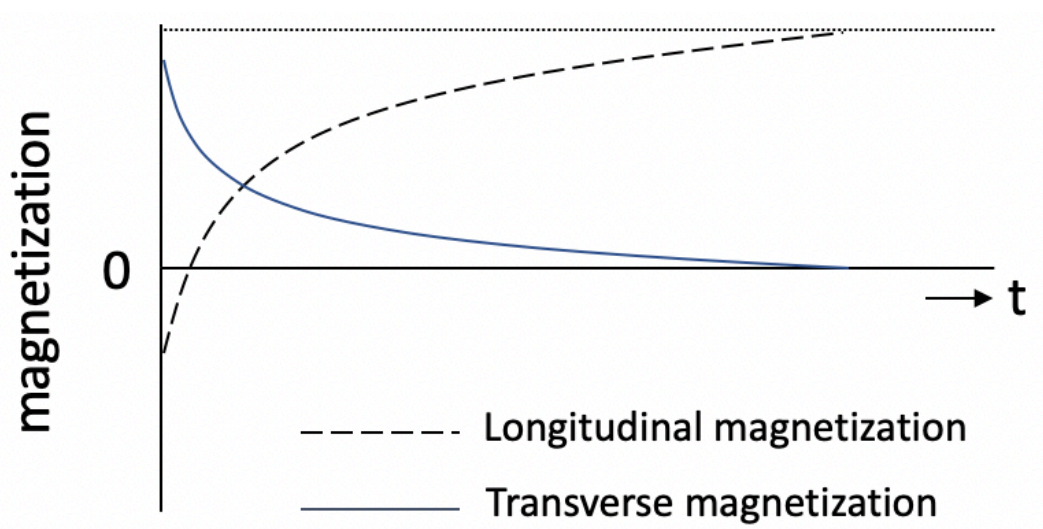
Figure 20 - T₁ and T₂ relaxation effects on system magnetisation as a function of time[8]

2.1.6 - Chemical Shift

In NMR one observes how charged nuclear spins behave in a magnetic field. One should remember that these spins exist in molecules with surrounding electrons that – to varying degrees – shield the nuclei from B_0. This shielding effect is explained by introducing the *effective magnetic field* B_{eff} induced by the electrons:

$$B_{eff} = (1 - \sigma)B_0$$

Equation 21 - The local magnetic field

where σ is the *shielding constant*, which is dimensionless and increases with the number of nearby electrons.

This is the reason why resonance lines in NMR spectra appear at different frequencies. It is possible for a nucleus to be either *shielded* or *de-shielded*, depending on its chemical environment. A shielded nucleus is one that is close to – or part of – an electropositive moiety. This nucleus is heavily surrounded by electrons that generate an effective magnetic field antiparallel to B_0. Remembering that the Larmor frequency is directly related to flux density B_0, it becomes evident that these spins precess at a *lower* frequency than one might expect. Oppositely, a nucleus said to be de-shielded is situated close to – or is part of – an electronegative moiety. In this case, the effective magnetic field is parallel to B_0, causing the de-shielded nucleus to precess at a frequency *higher* than the expected value. This knowledge is crucial in structural elucidation, as the chemical shift of a resonance is directly related to its electronegativity.

Because the frequency is dependent on magnetic flux density B_0, the chemical shift of a certain chemical environment will be found at different frequencies depending on the operator field strength of the spectrometer used. To circumvent this problem, an operator frequency-independent *chemical shift scale* has been constructed. This scale measures the shift in frequency from a reference standard, v_{ref}, in parts per million (ppm).

$$\delta(ppm) = \frac{v - v_{ref}}{v_{ref}}$$

Equation 22 - The Chemical Shift Equation

With this scale, different functional groups may be classified in terms of chemical shift ranges. This makes it easier to identify a functional group, but chemical shifts alone are often not enough to elucidate a structure.

2.1.7 - J-couplings

Whereas surrounding electrons shield nuclei from B_0, the bonding electrons within a molecule of interest produce another characteristic of many spectra, namely splitting patterns. These splitting patterns arise due to scalar couplings between the NMR-sensitive spins. These couplings may be either direct through space or indirect through chemical bonds. Direct couplings happen only in high-viscosity liquids or solids and are therefore of no interest in this thesis. Indirect couplings, however, are very important in structural elucidation. Spins will exchange information with nearby spins that are chemically equivalent. Keeping in mind that spins may be either parallel (*α*) or antiparallel (*β*) to B_0, summation of all possible states lead to several distinct splitting patterns separated by coupling constants *J* (Hz), and with intensity distributions in accordance with Pascal's triangle (**Fig.21** & **22**). If the nuclei are *magnetically inequivalent* as well as chemically, other splitting patterns than those shown in **Fig. 22** may occur, such as a doublet of doublets.

It should be noted that this is only the case when dealing with weakly coupled spin systems, where the coupling constant *J* is much smaller than the chemical shift differences (*J* ≫ *Δv*). This is of no importance as spin systems examined in this thesis are all weakly coupled.
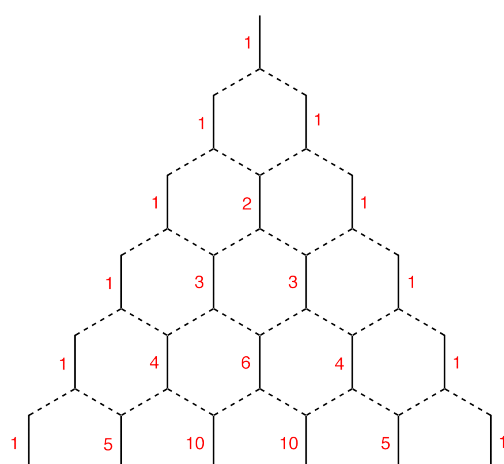
splitting pattern	the ratio of heights of llines in the peak
singlet	1
doublet	1:1
triplet	1:2:1
quartet	1:3:3:1
quintet	1:4:6:4:1
sextet	1:5:10:10:5:1

Figure 21 - NMR signal intensity distributions as given by Pascal's triangle[27]
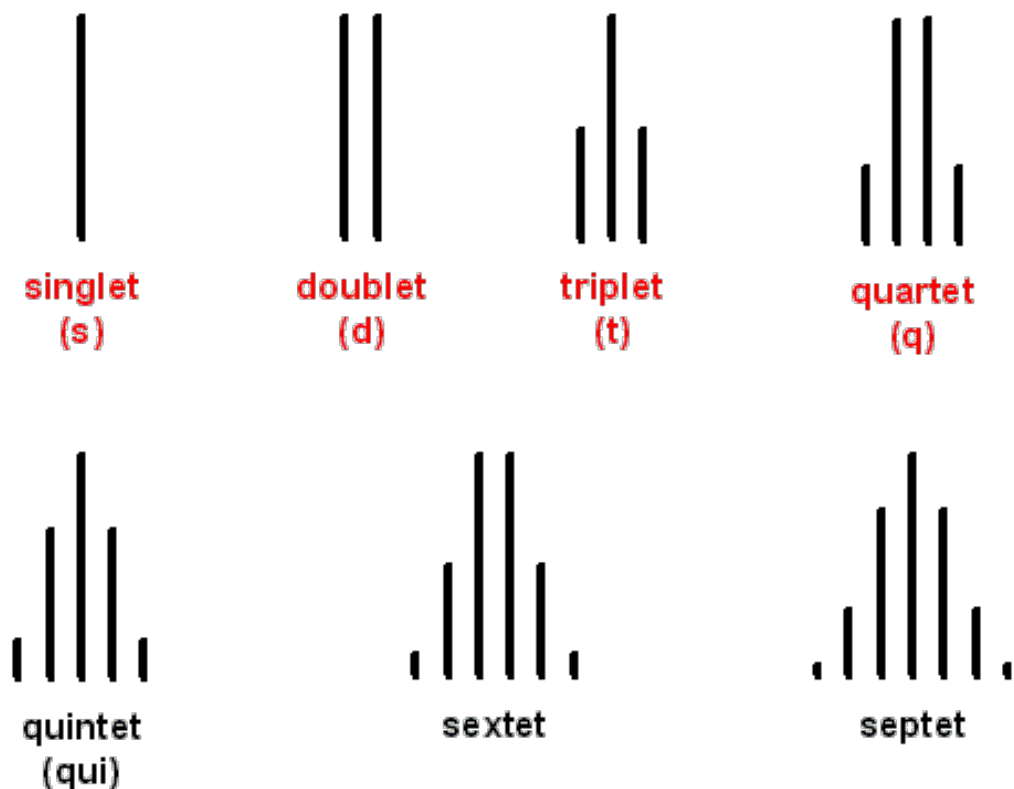
Figure 22 - NMR splitting patterns according to the (n+1) rule[28]

2.2 – Product Operator Formalism

Unlike VMA, the product operator formalism approach relies on extracting information from the spins' wavefunctions using operators or products of operators, hence the name. This method is superior to the vector model when explaining weakly coupled systems, especially when the spin transformations are mathematically complex.

2.2.1 – Basis of POF – Operators, eigenfunctions and observables.

According to quantum mechanics, all the properties of a nuclear spin may be gathered from its wavefunction. As wavefunctions are eigenfunctions, various QM operators will regain the wavefunction along with an associated eigenvalue:

$$\hat{\Omega}\psi = \omega\psi$$

Equation 23 - Eigenfunction equation

where $\hat{\Omega}$ is the operator, ψ the eigenfunction and ω the eigenvalue.

In a sample, a large number of spins form what is known as an *ensemble*. All the information pertaining to these spins may be calculated using the *density operator*, $\hat{\rho}$:

$$\hat{\rho} = a_x(t)\hat{I}_x + a_y(t)\hat{I}_y + a_z(t)\hat{I}_z$$

Equation 24 - The density operator

Where $\hat{I}_x$, $\hat{I}_y$ and $\hat{I}_z$ represent spin x,y- and z-angular momentum components, respectively. The associated coefficents a are simply numbers that vary with time t. They are proportional to the magnetisation x,y- and z-components:

$$M_x(t) \propto a_x(t) \qquad M_y(t) \propto a_y(t) \qquad M_z(t) \propto a_z(t)$$

Equation 25 - Density operator coefficients

Knowing the coefficients, one can determine the overall magnetisation of the sample as well as its variation with time. Thus, the density operator provides complete information of the spin system. To show how the magnetisation varies with time, the density operator equation is expressed as a function of t:

$$\hat{\rho}(t) = \exp\left(-i\hat{H}t\right)\hat{\rho}(0)\exp i\hat{H}t$$

Equation 26 – The density operator as a function of time

where $\hat{H}$ – the Hamiltonian – is the operator for observable energy quantity. It has been shown that the Hamiltonian expresses spin evolution for time period t. $\hat{H}$ is an operator which acts according to the rotating frame model. There are different versions of the Hamiltonian depending on the system it describes.

For a particle in free precession, the Hamiltonian is as follows:

$$\hat{H}_{free} = \Omega I_z$$

Equation 27 - Hamiltonian for free precession

Where Ω, the offset, is difference in frequency of the rotating frame and the Larmor frequency of the nuclear spin.

In a situation where a hard pulse about the x-axis is applied to a nuclear spin, the Hamiltonian is as follows:

$$\hat{H}_{x,pulse} = \omega_1 I_x$$

Equation 28 - Hamiltonian for a hard pulse about the x-axis

Suppose that a nuclear spin vector lies along $+z$, and that a 90° pulse is applied from $+x$. It has already been explained by the vector model that this will generate complete transverse

magnetisation along the *y*-axis. Using POF, the changes to the system may be explained solving **Eq. 26** for pulse width, t_p:

$$\hat{\rho}(t_p) = \exp\left(-i\widehat{H}_{x,pulse}\, t_p\right) \hat{\rho}(0) \exp i\widehat{H}_{x,pulse}\, t_p$$

Which may be solved using the following trigonometric identity:

$$\exp\left(-i\theta \hat{I}_x\right) \hat{I}_z \exp\left(i\theta \hat{I}_x\right) \equiv \cos\theta\, \hat{I}_z - \sin\theta\, \hat{I}_y$$

Equation 29 - Trigonometric identity describing rotation of $\hat{I}_z$ through an angle θ.

Using **Eq. 28** we may rewrite $(\widehat{H}_{x,pulse}\, t_p)$ as $(\omega_1 t_p)$:

$$\exp\left(-i\omega_1 t_p \hat{I}_x\right) \hat{I}_z \exp\left(i\omega_1 t_p \hat{I}_x\right) \equiv \cos\left(\omega_1 t_p\right) \hat{I}_z - \sin\left(\omega_1 t_p\right) \hat{I}_y$$

As one can see, the equations that arise in the POF approach may become rather cumbersome to write down. Because of this, a simpler notation is employed:

$$\hat{I}_z \xrightarrow{\omega_1 t_p \hat{I}_x} \cos\left(\omega_1 t_p\right) \hat{I}_z - \sin\left(\omega_1 t_p\right) \hat{I}_y$$

Equation 30 - Effect of a hard 90°x pulse on z-magnetisation.

After the pulse is applied, the spins may undergo a period of free precession according to **Eq. 27**. The effect of free precession will be calculated for both the cosine and sine terms separately.

First, the cosine term:

$$\cos\left(\omega_1 t_p\right) \xrightarrow{\Omega t \hat{I}_z} \cos(\Omega t) \cos\left(\omega_1 t_p\right) \hat{I}_z - \sin(\Omega t) \cos\left(\omega_1 t_p\right) \hat{I}_y$$

Now, the sine term:

$$\sin\left(\omega_1 t_p\right) \xrightarrow{\Omega t \hat{I}_z} -\cos(\Omega t) \sin\left(\omega_1 t_p\right) \hat{I}_y - \sin(\Omega t) \sin\left(\omega_1 t_p\right) \hat{I}_z$$

Adding these terms together will give the end result of a simple experiment where a *one spin system* experiences a hard pulse and subsequent free precession. It is important to note that

many spin systems contain more than one spin, and there will usually be some form of coupling between these spins. The Hamiltonian for a weakly coupled two-spin system is as follows:

$$\hat{H}_{two\ spins} = \Omega_1\hat{I}_{1z} + \Omega_2\hat{I}_{2z} + 2\pi J_{12}\hat{I}_{1z}\hat{I}_{2z}$$

Equation 31 - The Hamiltonian for two weakly coupled spins.

The first two terms are the free precession terms for spins 1 and 2 respectively, and the last term accounts for the evolution of scalar coupling. This term involves the coupling constant J_{12}.

Suppose that, after a 90°x pulse, a nuclear spin vector $-\hat{I}_y$ evolves under the scalar coupling. If one, for the time being, ignores the period of free precession, the calculation becomes:

$$-\hat{I}_y \xrightarrow{2\pi J_{12}t\hat{I}_{1z}\hat{I}_{2z}} -\cos(\pi J_{12}t)\,\hat{I}_y + \sin(\pi J_{12}t)\,2\hat{I}_{1x}\hat{I}_{2z}$$

From the calculation it may be seen that a new angular momentum term *(2$\hat{I}_{1x}\hat{I}_{2z}$)* occurs. This is known as an *anti-phase* term, while terms such as $\hat{I}_y$ are known as *in-phase* terms. Anti-phase magnetisation does not lead to any transverse magnetisation and will therefore not yield an NMR signal, but in-phase magnetisation *does*. If antiphase magnetisation is allowed to evolve over time it will convert to in-phase magnetisation at a rate depending on *t*. As can be seen from the previous calculation, complete conversion to anti-phase magnetisation occurs when $\sin(\pi J_{12}t)2\hat{I}_{1x}\hat{I}_{2z} = 1$, which is achieved by letting the magnetisation evolve for a time equal to $\frac{1}{2J_{12}}$.

This anti-phase magnetisation is extremely important in the POF approach and is used to explain NMR phenomena where the VMA becomes insufficient.

2.3 – Selective excitation

If the offset and RF field strengths are comparable in size, the effective field – around which the magnetisation precesses – follows a complex curved path towards the *xy*-plane following excitation. This can be used for selective excitations of spins. The image below shows the evolution of equilibrium magnetisation following excitation by RF pulses about *+x* with different resonance offsets. As the offset increases, and one moves further away from on-resonance conditions, the evolution of *M_0* curves so that it loses *y*-character and gains *x*-

character. This causes phase errors in the spectrum. In addition, the amount of *xy*-magnetisation generated by the pulse decreases along with increasing resonance offset of the applied pulse, and thus the overall signal is expected to be weaker than that of an on-resonance pulse.

Because the magnetisation produced by a 90°$_x$ pulse is a function of the offset, it is possible to excite specific parts of the NMR spectrum by changing the transmitter frequency so that it is on resonance with the desired spectral area (e.g., a multiplet). A subsequent reduction of the RF field strength can be made so that the magnetisation in all the non-selected areas of the spectrum is minimal, but maximal within the selected region. Because the RF-field is reduced, the pulse duration required to generate a flip angle of 90° must be increased. Pulses such as these are referred to as *selective pulses* or *soft pulses*.

In addition to phase errors due to an *xy*-character, soft pulses face another problem. The excitation of non-selected areas falls off rather slowly, and some co-excitation of these areas are to be expected. This causes wiggles to appear on the spectrum. A solution to this problem is to use *shaped pulses*, i.e., pulses with specifically shaped envelopes. The most common variation is a bell-shaped gaussian envelope which suppresses the wiggles at large offsets, leading to a smoother decay. Another alternative is to use sinc pulses, which after a Fourier transformation yield narrow square excitation profiles[29].
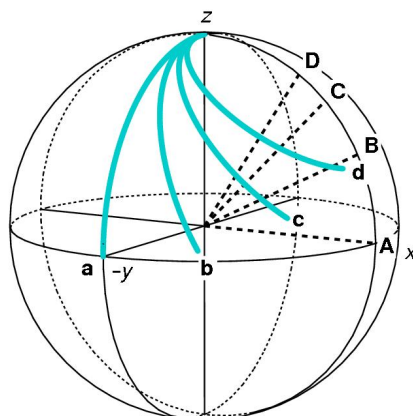
Figure 23 - Three-dimension representation of equilibrium magnetisation follow 90°$_x$ pulses of various offsets[25]

*The blue lines represent the evolution of equilibrium magnetisation, and the dashed lines represent the effective field. Path **a** represents the on-resonance case, where the resulting bulk magnetisation is completely parallel to **-y**. Paths **b** through **d** represent off resonance cases. The pulse duration is chosen so that the flip angle is 90° in **a**.*
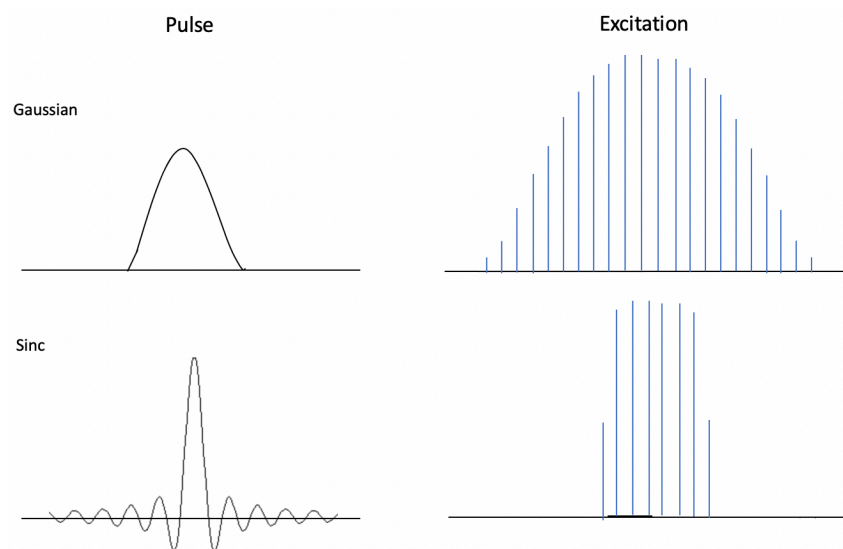
Figure 24 - Gaussian and sinc pulses along with their respective excitation profiles[8]

There are two ways in which selective pulses are applied. One can apply magnetic field gradients (MFG) to selectively excite sample space depending on the MFG bandwidth. This is the basis of the *voxel* (volume element) in single-voxel spectroscopy, where spatial localisation is achieved by gradient-mediated selective excitation in the *x-*, *y-* & *z*-planes. Sinc pulses are commonly used for this purpose as one wants pulses that are uniform over their entire area, and because square voxels are usually desirable. Spatial localisation is explained further in **2.4**. The other type of selective excitation involves the use of soft pulses in order to target specific resonances depending on its offset. Gauss pulses or pseudo-Gauss pulses are often used for this approach. This is the basis for *J*-editing techniques, as will be demonstrated in **2.6**.

2.4 - Magnetic field gradients and Single Voxel Spectroscopy[30]

The NMR signal can be made spatially dependent by applying a magnetic field gradient (MFG) G_z applied along the *z*-axis.

$$v(z) = v_0 - \gamma G_z = \left|\frac{\gamma}{2\pi}\right| B_0 - \gamma G_z$$

Equation 32 - Spatial dependency of the Larmor frequency in the presence of a pulsed field gradient

It follows that the resonance condition also becomes spatially dependent depending on a spin's position along the *z*-axis in the sample. By applying MFGs along all three axes, the resonance condition will only be met at the intersection of the three pulses. This is area is known as a *voxel*. The ability to gather information from certain localisations is paramount to *in vivo*

spectroscopy as cellular compartmentalisation leads to local variations in metabolites and their concentrations.

2.5 The Spin-echo Experiment, J-modulation and difference spectroscopy

In NMR experiments one cannot avoid loss of signal over time due to T_1-relaxation, but it is possible to avoid loss of signal due to some of the T_2-relaxation by employing a spin-echo sequence. The sequence, in its simplest form, may be expressed as $90° - \tau - 180° - \tau$.
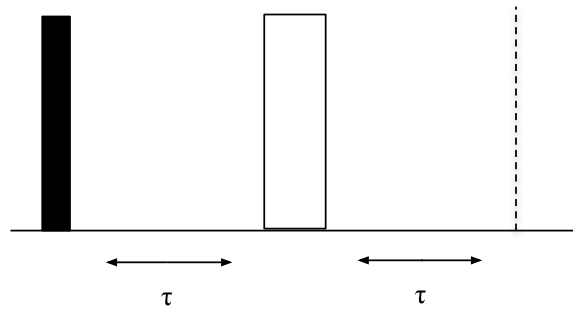
Figure 25 - The spin-echo pulse sequence

The filled in rectangle represents a $90°_x$ pulse, and the broad transparent rectangle represents a 180° pulse. The echo forms at the dashed line.

Imagine a homonuclear (^1H-^1H) spin system of two weakly coupled spins. Following a $90°_x$ excitation pulse applied to spin one, the bulk magnetisation is aligned parallel to -y.

$$\hat{I}_{1z} \xrightarrow{\frac{\pi}{2}\hat{I}_x} \cos\left(\frac{\pi}{2}\right)\hat{I}_{1z} - \sin\left(\frac{\pi}{2}\right)\hat{I}_{1y} = -\hat{I}_{1y}$$

Following the hard pulse, the scalar coupling evolves as described by the Hamiltonian for two coupled spins (eq. 27). If one again ignores the evolution under the offsets, the situation after τ is

$$-\hat{I}_{1y} \xrightarrow{2\pi J_{12}\tau \hat{I}_{1z}\hat{I}_{2z}} -\cos(\pi J_{12}\tau)\,\hat{I}_{1y} + \sin(\pi J_{12}\tau)\,2\hat{I}_{1x}\hat{I}_{2z}$$

After τ, a $180°_x$ pulse is applied to spin one and two. The only effect of this pulse is to change the sign of both terms.

$$-\cos(\pi J_{12}\tau)\,\hat{I}_{1y} + \sin(\pi J_{12}\tau)\,2\hat{I}_{1x}\hat{I}_{2z} \xrightarrow{\pi\hat{I}_{1x}+\pi\hat{I}_{2x}} \cos(\pi J_{12}\tau)\,\hat{I}_{1y} - \sin(\pi J_{12}\tau)\,2\hat{I}_{1x}\hat{I}_{2z}$$

During the second time delay τ the scalar coupling evolves again, while the evolution of offsets is ignored. The reason we may ignore the evolution of offsets is because the sign change due to the 180° pulse leads to an offset evolution in the *opposite direction* compared to during the first time delay, thus cancelling each other out. At the end of 2τ the system is in the current state:

$$\cos(\pi J_{12}\tau)\,\hat{I}_{1y} - \sin(\pi J_{12}\tau)\,2\hat{I}_{1x}\hat{I}_{2z}$$

$$\xrightarrow{2\pi J_{12}\tau\hat{I}_{1z}\hat{I}_{2z}} \cos^2(\pi J_{12}\tau)\hat{I}_{1y} - \sin^2(\pi J_{12}\tau)\hat{I}_{1y} - 2[\sin(\pi J_{12}\tau)\cos(\pi J_{12}\tau)]\,2\hat{I}_{1x}\hat{I}_{2z}$$

This term may be simplified by the two following trigonometric identities:

$$\cos^2\theta - \sin^2\theta = \cos 2\theta \qquad\qquad 2\cos\theta\sin\theta = \sin 2\theta$$

$$\therefore \cos(\pi J_{12}\tau)\,\hat{I}_{1y} - \sin(\pi J_{12}\tau)\,2\hat{I}_{1x}\hat{I}_{2z} \xrightarrow{2\pi J_{12}\tau\hat{I}_{1z}\hat{I}_{2z}} \cos(2\pi J_{12}\tau)\,\hat{I}_{1y} - \sin(2\pi J_{12}\tau)\,2\hat{I}_{1x}\hat{I}_{2z}$$

It can be seen that the overall result of the homonuclear spin echo is to allow the coupling to allow for a period 2τ (the *echo time*), as well as applying a 180° pulse. Both offsets and the phase coherence are refocused in the pulse sequence, but true T_2 effects, as well as T_1 effects, cause inevitable signal loss. Furthermore, one can select either complete conversion to in-phase- or anti-phase magnetisation depending on the value of τ. Complete in-phase magnetisation is achieved by choosing $\tau = 1/2J_{12}$. The anti-phase conversion is achieved by choosing $\tau = 1/4J_{12}$. The signal is said to be *J-modulated* by the phase angle $\theta = (2\pi J_{12}\tau)$.

The GABA resonances of interest are triplets (HC) and a pseudo-triplet caused by a superimposed doublet-of-doublets (HA)[31]. Both resonances are expected to be similarly modulated by the coupling. A triplet may be thought of as a combination of a singlet and a doublet (inner and outer resonances respectively). The inner resonance behaves as other singlets; uncoupled. The outer resonances behave as a doublet with each peak separated by 1J from the inner resonances, creating a doublet of coupling distance 2J. The phase angle thus becomes $\theta = (4\pi J_{12}\tau)$. In-phase triplets are achieved by choosing $\tau = 1/J_{12}$. Anti-phase triplets are chosen by $\tau = 1/2J_{12}$.

The J-modulation is useful because it allows for the removal of unwanted signals through *difference spectroscopy*, which means subtracting two differently J-modulated spectra from

each other. With the help of selective excitation pulses, one can effectively hinder the J-evolution of a chosen spin system. Subtraction will then lead to all other resonances cancelling out, while a *subtraction signal* remains for all spins coupled to the selectively excited resonance.

2.6 – The MEGA-PRESS sequence

In order to isolate the GABA signal in the phantom solution, the MEGA-PRESS pulse sequence was used. This pulse sequence is a spin-echo featuring a soft pulse before and after the 180° pulse.
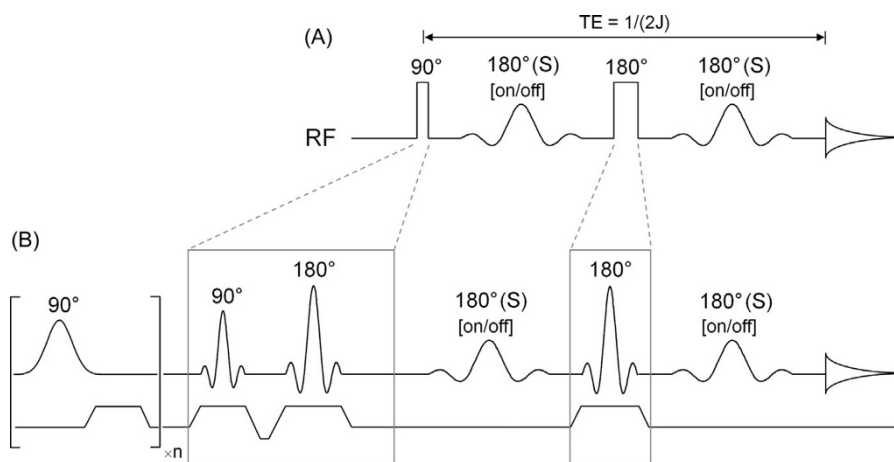
Figure 26 - The MEGA-PRESS sequence[32]

(A) Shows the basic J-difference experiment. (B) shows the 3D-localized, water-suppressed MEGA-PRESS experiment. The initial water suppression scheme may be CHESS, VAPOR or others.

By applying the soft pulses on the GABA HB resonance, the HA and HC resonances will not undergo J-evolution during the sequence. This is known as the ON-experiment. Another experiment is run with these pulses off in the OFF-experiment. In this experiment, anti-phase triplets are chosen so that subtraction will lead to an addition of the outer resonances. Subtracting the OFF- from the ON-spectrum removes the inner resonance and all other non-GABA resonances, while the outer resonances appear as a doublet of doubled intensity.
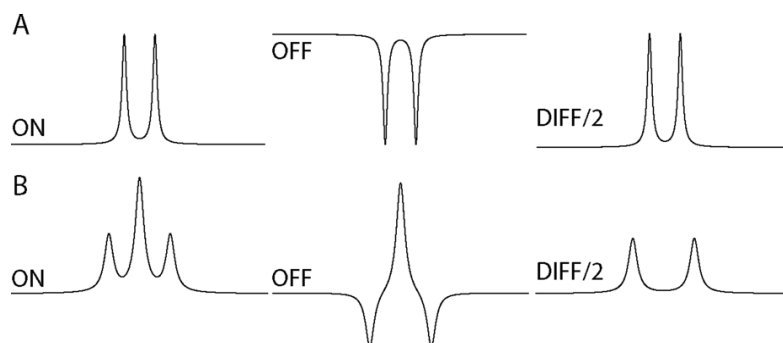
Figure 27 - Illustration of J-difference editing for doublets and triplets[33]
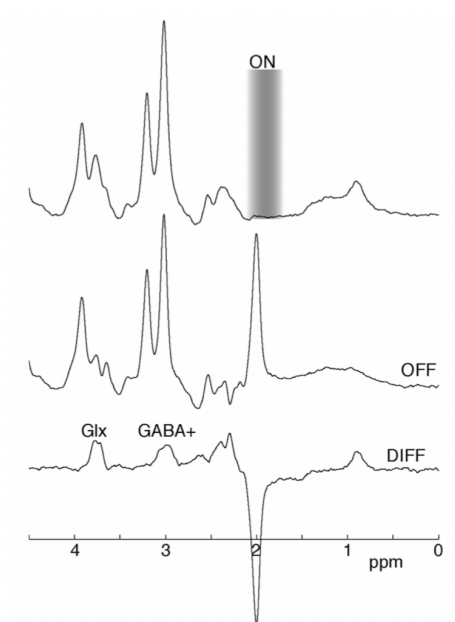
Figure 28 - Example of in vivo J-difference editing using the MEGA-PRESS sequence[33].

2.8 – The NMR signal; acquisition, detection and processing.

2.8.1 – The NMR signal equation and Fourier transformation

The spectrometer measures both x-and y-magnetisation simultaneously, and yields signals of the form:

$$S_x = S_0 \cos \omega t \qquad S_y = S_0 \sin \omega t$$

Equation 33 - The NMR signal components

When nuclear spins oscillate around $\mathbf{B_0}$ with a $\boldsymbol{xy}$-component, they induce a current in the spectrometer's receiver coil. This signal, known as the Free Induction Decay $\mathbf{S_{FID}(t)}$, consists of both x- and y-components. This signal may be expressed as:

$$S_{FID}(t) = S_X + iS_y$$

$$S_{FID}(t) = S_0 \cos(\Omega t) \exp\left(-\frac{t}{T_2}\right) + i[S_0 \sin(\Omega t) \exp\left(-\frac{t}{T_2}\right)]$$

$$S_{FID}(t) = S_0 \left(\cos(\Omega t) + i \sin(\Omega t)\right) \exp\left(-\frac{t}{T_2}\right)$$

$$\boldsymbol{S_{FID}(t) = S_0 \exp(i\Omega t) \exp\left(-\frac{t}{T_2}\right)}$$

Equation 34 - NMR signal equation

The FID measures the NMR signal in the *time-domain* as a wave function. This makes NMR unique compared to other spectroscopic methods which always measure signal as a function of frequency. In order to interpret the NMR signal, it needs to presented as a function of frequency. This is achieved by Fourier transformation.

The Fourier transformation involved multiplying the FID waveforms with trial cosine waves of the form $\cos(2\pi f t)$ varying in frequency.

Mathematically, this process may be explained as follows:

$$S_{spectrum}(f) = \int_0^{+\infty} S_{FID}(t) \cos(2\pi f t) \, \mathrm{d}t$$

Equation 35 - Fourier transformation of time-domain signal function

In this equation, $\boldsymbol{S_{spectrum}(f)}$ is the frequency-domain signal and $\boldsymbol{S_{FID}(t)}$ the time-domain signal. In essence, one multiplies the area under the FID curve by trial cosine waves of varying frequency. However, because computers are used to manipulate the FID, the signal is digitised and stored as a series of numerical values rather than a curve. In this case, the Fourier transformation uses a summation of cosine wave products instead of integration.

$$S_{spectrum}(f) = \sum_{i=1}^{i=N} S_{FID}(t_i) \cos(2\pi f t_i)$$

Equation 36 - Fourier transformation of a series of numerical values
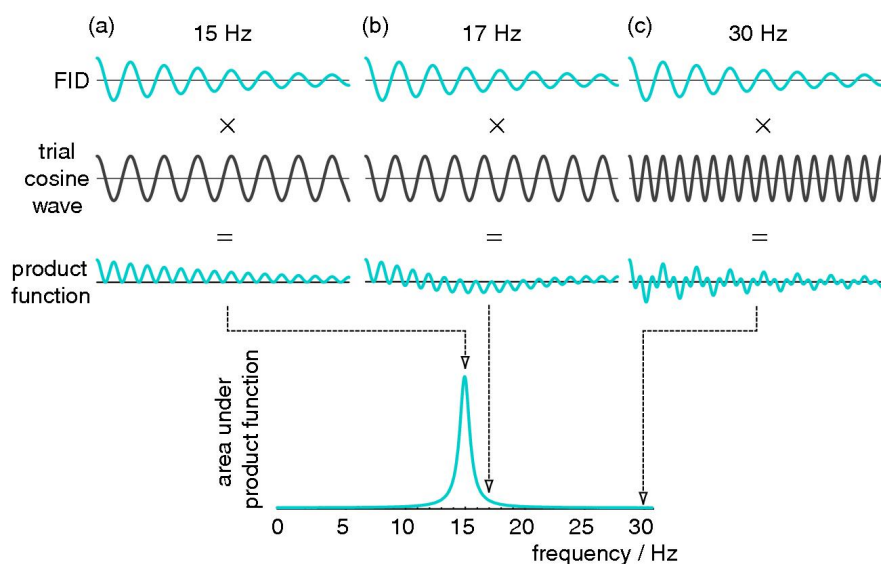
Figure 29 - Fourier Transformation illustration[25]

Demonstration of multiplying the FID with different cosine trial waves. In (a) the trial cosine wave matches the FID so that all areas are greater than zero. This corresponds to the signal maxima in the frequency domain. In (b) there is a slight surplus of area greater than zero, which creates the "tails" of the NMR signals. In (c) the trial wave does not match the FID, so that the resulting frequency-domain area contains no signal except noise.

2.8.2 – Signal processing: phasing the spectrum

The frequency-domain signal (NMR spectrum) will most likely have an arbitrary phase error which distorts the lines. Therefore, the FID is multiplied by a phase-correction factor $e^{i\phi}$. This factor is difficult to calculate and is therefore commonly found empirically. This phasing is applied to the whole spectrum and is therefore known as *frequency independent-* or *zero order* phase correction.

The NMR signal will sometimes also have a *frequency-dependent* phase errors arising from x-magnetisation generated by a selective excitation pulse. Selective soft pulses in NMR will often affect a slightly wider frequency range than intended due to their sine bell shape. Therefore, a selective $90°_x$ pulse may generate *some* off-resonance x-magnetisation in addition to the desired y-magnetisation. As signal detection happens along the y-axis, any x-magnetisation arising from unwanted excitation will be offset-dependent and shifted by 90°. Off-resonance effects are approximately proportional to the transmitter offset $\boldsymbol{\Omega}$ so that it may be accounted for by multiplication by a phase-correction factor $\boldsymbol{k}$. Similar to zero-order phase correction, frequency-dependent – or *first order* – phase correction is a tentative approach (in this case adjusting $\boldsymbol{k}$).

$$\phi_{corr} = k \, \Omega$$

Equation 37 - First order phase correction

2.8.3 – Noise

NMR-spectroscopy is sensitive to noise, which is mainly generated by the receiver coil. Thus, all recordings of FIDs come with a certain amount of noise which may disrupt the signal. The noise is Gaussian with zero mean, which means that may be expressed by a Gaussian function that reaches a mean average of zero with time. As one records the FID, the NMR signal dies out relatively quickly due to relaxation processes. If the acquisition is kept going, one will record mostly electrical noise and little signal of interest, which will lead to poor signal-to-noise ratio (SNR). Therefore, one should aim to keep acquisition times short. In addition to shortening the acquisition times, the random nature of the electrical noise means that it will cancel itself out to some degree when adding several acquisition parallels together. It turns out that the noise is reduced by $1/\sqrt{N}$ where N is the number of acquisitions. Thus, keeping acquisition times as short as possible and sampling several acquisitions greatly improves SNR.
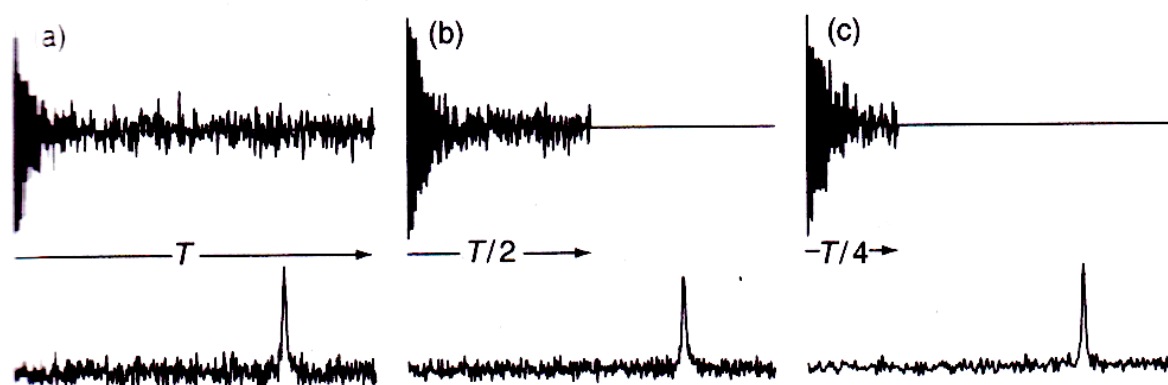
Figure 30 - Sampling time and electrical noise[25]

2.8.4 – Water suppression

In NMR spectroscopy signal intensity depends on concentration. It follows that the water signal will be very strong compared to anything else in aqueous solutions. The signal is, in fact, so much stronger that it dwarfs most other signals to the point where they become invisible. Therefore, it is important to either completely or partially remove the water signal, so that its signal intensity becomes comparable to signals. Various methods have been developed to accomplish this. The most common method involves selective saturation of the water resonance prior to acquisition in what is known as *presaturation.*

2.9 – Diffusion and diffusion-weighted Spectroscopy[22,30,34]

Particles suspended in a fluid undergo Brownian motion, i.e., they move randomly due to collisions with other particles. Einstein discovered that a particle's displacement in a 3D-space over time was expressed by

$$<r^2> = 6Dt$$

Equation 38 - The displacement of a particle due to Brownian motion.

D is known as a particle's *diffusivity* or simply the diffusion constant. These are usually given in (mm^2/s) or (m/s^2), and are given by the Einstein-Stokes equation:

$$D = \frac{k_B T}{6\pi\eta r}$$

Equation 39 - The Einstein-Stokes equation

where k_B is the Boltzmann constant, T the absolute temperature, η the viscosity of the fluid and r the particle radius.

Due to spatial dependency induced by an MFG, if a particle is displaced to another area of the sample during a spin echo sequence it may no longer have its phase coherence refocused, which is seen as attenuation of the signal on the spectrum.

In the Stejskal-Tanner sequence[35], which is a so-called PFGSE (pulsed field-gradient spin echo), magnetic field gradients of equal sign and magnitude are applied before and after a 180° pulse with the purpose of dephasing and rephasing M_{xy}, so that the overall loss of phase coherence due to MFG-induced B_0 inhomogeneities is reversed at the formation of the echo. Meanwhile, the loss of phase coherence caused by Brownian motion is *irreversible*. Therefore, the observed echo signal attenuation – governed by irreversible T_2-processes – in the Stejskal-Tanner sequence must be a result of diffusion. This signal attenuation is used to measure the diffusivity of a particle.
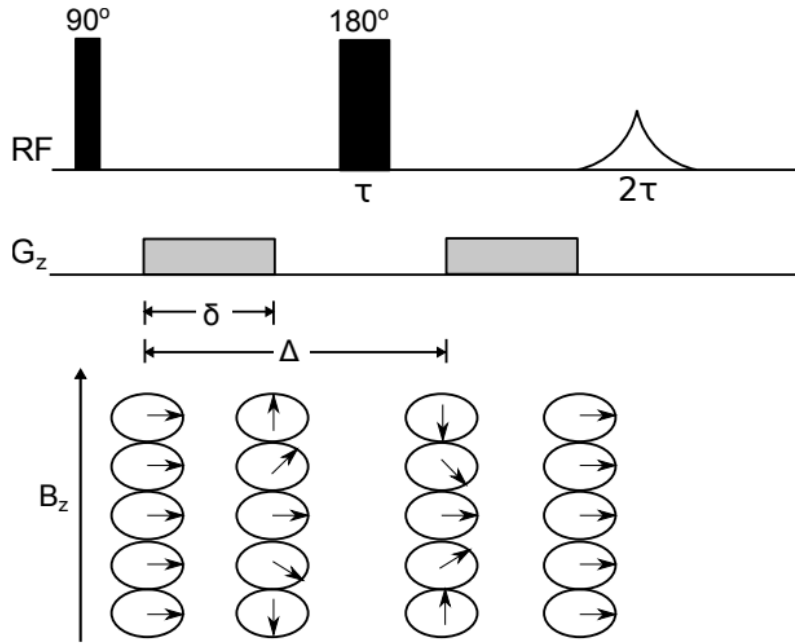
Figure 31 - The Stejskal-Tanner PFGSE experiment.[35]

MFGs are placed before and after the 180° pulse. At the formation of the echo all phase coherence loss not arising from diffusion is refocused, as is shown in the phase diagram below.

The diffusion-weighted signal is found by solving the Bloch equation for transverse magnetisation in a spin echo in which one multiplies the expression by e^{-bD}.

$$S(b) = M_0 \exp\left(-\frac{2\tau}{T_2}\right) \exp -bD$$

This signal may be normalised with respect to the signal without diffusion weighting, S_0.

$$S(b) = S_0 e^{-bD}$$

Equation 40 - Mono-exponential model for diffusion-related signal attenuation

where **b**, known as the b-factor (diffusion-weighting factor), explains the effect of the applied MFG in the sequence.

$$b = \gamma^2 g^2 \delta^2 (\Delta - \frac{\delta}{3})$$

Equation 41 - The b-factor

where γ is the gyromagnetic ratio, g the MFG amplitude, δ the amplitude duration and Δ the time between the dephasing and rephasing gradient pulses (diffusion time in z-direction). Increasing the b-factor causes higher signal attenuation.

In cells the diffusion will be anisotropic and can no longer be fully explained by the mono-exponential model, and therefore the Stejskal-Tanner sequence may only measure *apparent diffusion coefficients* (ADC) when used *in vivo*. By taking the logarithm of the signal attenuation and plotting it against -bD (-b*ADC *in vivo*), the diffusion coefficient can be found if the **b**-values are known.

$$\ln\left(\frac{S(b)}{S_0}\right) = -b * ADC$$

Equation 42 - The apparent diffusion coefficient

The **b**-value is:

$$b = \left[\delta^2 g^2 \left(E - A + 3(D - B) - \frac{2}{3}\delta\right)\right] + [\delta^2 g^2 S(4C - 2D - 2E)]$$

Equation 43 - Calculation of b-value

where **S** is the signal and **A-E** indicate the MFG timings in the diagram below
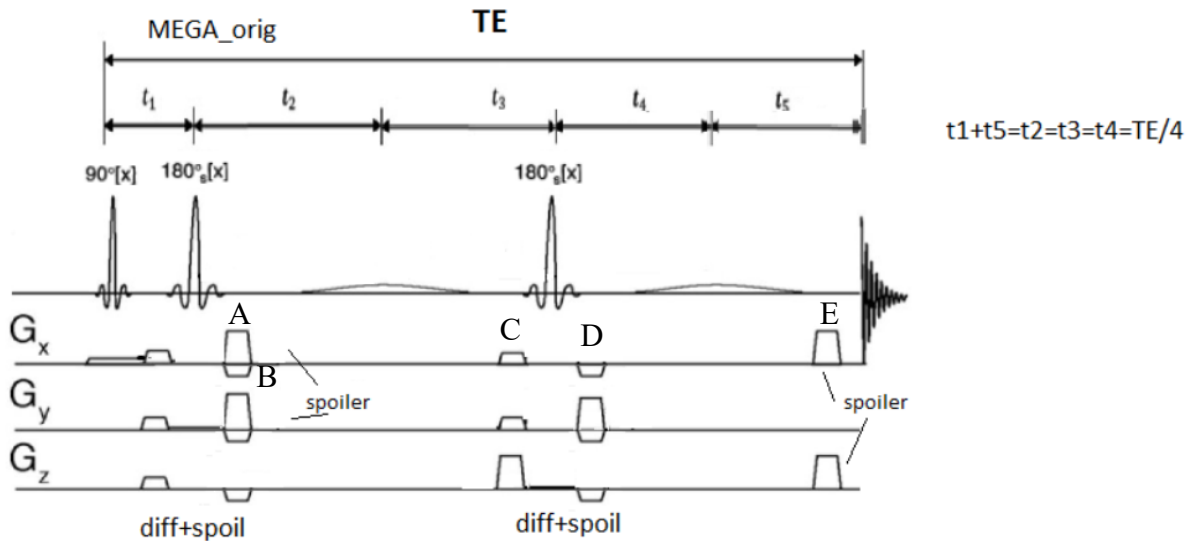
Figure 32 – Original-based DW-MEGA-PRESS schematic diagram with MFG labels

3 Experimental

3.1 – Preparation

Samples were analysed in 10mm NMR tubes on a *Bruker BioSpin* 500 WB system using a MICWB40 micro-imaging probe head. In-house software (*Paravision* 6.0.1[36], *TopSpin* 3.1PV) was used for MRI/MRS data acquisition, reconstruction and analysis. A *MATLAB* script created by doctoral student Emile Berg was used for metabolite diffusion constant analyses.

Following manual tuning and matching of the probe, an initial slice-selective MRI sequence (FLASH)[37] was used to place the voxel in the sample as well as check for any physical inhomogeneities (e.g., air bubbles, dust etc.) that would interfere with the signal. A B_0-mapping procedure determined the magnetic homogeneity in the sample, and a subsequent localized shimming routine was performed in order to obtain maximal magnetic homogeneity inside the region of interest (ROI). The water signal was suppressed using the VAPOR sequence as a built-in function in *ParaVision*.

3.2 – Phantom solution preparation example.

Phantom solutions and solutions with select metabolites were prepared in accordance with the following table:

Table 9 - Preparation of phantom solution + GABA with concentrations mimicking in vivo *values of the human brain.*

Compound	M (g/mol)	C (mmol/L)
Cr	149,15	10,02
Cho	139,62	2,92
NAA	175,14	12,49
m-Ins	180,16	7,50
Glu	187,13	12,45
Lac	112,06	5,26
GABA	103,12	2,16
GSH	307,12	3,02

3.3 – Calibration curves[1]

Calibration curves for GABA was constructed by creating six samples A-F with increasing GABA concentration. Any additional metabolites' concentrations were kept constant. For each sample, both the PRESS- and the MEGA-PRESS-experiments (ON/OFF) were run following the preparations detailed in section 3.1. The spectra were processed and manually integrated in *TopSpin* 4.0.9; the calibration curves were created in Microsoft Excel.

---

[1] See Appendix A for a complete overview of experimental data

The manual integration in *TopSpin* yields an S.I relative to the initially integrated signal. By systematically choosing the NAA peak at 2.0 ppm as the first integral, *TopSpin* associates a 3-proton signal with an S.I of 1.000. Thus, a one-proton signal should theoretically be 0.333, and a two-proton signal be 0.666. The GABA HA and HC resonances are both from CH_2-groups, so that the proton difference factor becomes 2/3. The concentration difference also affects the signal, so that the calibration curve signal is based on the formula:

$$SI_{GABA} = \left(\frac{2H}{3H}\right) * \left(\frac{[GABA]}{[NAA]}\right)$$

Equation 44 - Signal intensity equation used in the construction of NMR calibration curves

Thus, a linear response to increasing the GABA concentration is expected.

3.3.1 – Example of calibration curve experiment: NAA/GABA

Table 10 – Example of calibration curve experiment

The GABA concentration is increased by 2 mM for each sample while NAA concentration is kept constant.

Sample	[GABA]	[NAA]
A	0	12,5
B	2	12,5
C	4	12,5
D	6	12,5
E	8	12,5
F	10	12,5

3.4 – Diffusion measurements[2]

Metabolite solutions were prepared as detailed in section 3.1, and an initial PRESS sequence was used to ascertain good signal quality. Browsing relevant literature gave no absolute ADC values for the MOIs in aqueous solutions. Therefore diffusion probe experiment was run to serve as a theoretical value of the ADCs in SVS experiments.

3.4.1 – Acquisition example

A diffusion-weighted MEGA-PRESS sequence was run with dipolar spoiler gradients used to dephase and rephase the NMR signal in order to directly relate any signal attenuation to diffusion effects. The spoiler gradient amplitudes (**g**) were increased from zero to thirty percent

---

[2] See Appendix B for a complete overview of experimental data.

of maximal gradient amplitude (maximum = 1.4 T/m) with three-percent increments for a total of eleven ON/OFF experiments per parallel. MFG width (δ) and the time between them (Δ) were kept constant.

Below is a table showing the experimental setup of the diffusion measurement experiments. The selected chemical shift values for the editing pulses are *added* to the water resonance at 4.7 ppm. An easy way to run the OFF experiment is to simply place these pulses at an area where they will not affect the signal. A value of 3.0 ppm is chosen for editing pulses 1&2 so that they are applied at 7.7 ppm. In the ON experiments the pulse(s) are applied to the GABA H_B resonance by choosing a value of -2.9 ppm so that (4.7 – 2.9) ppm = 1.8 ppm.

Table 11 - Example of diffusion measurement experimental setup

G_z is the spoiler gradient amplitude applied along the z axis. Ep1 and Ep2 are the chemical shift selective editing pulses. A value of 3.0 ppm is chosen for editing pulses 1&2 so that they are applied at (4.7+ 3.0) ppm = 7.7 ppm in the OFF experiments. In the ON experiments the pulses are applied to the GABA H_B resonance by choosing a value of -2.9 ppm so that (4.7 – 2.9) ppm = 1.8 ppm.

Experiment	G_z (%)	Ep^1 (ppm)	Ep^2 (ppm)
OFF	0,0	3,0	3,0
ON	0,0	-2,9	-2,9
OFF	3,0	3,0	3,0
ON	3,0	-2,9	-2,9
...	...	...	...
OFF	30,0	3,0	3,0
ON	30,0	-2,9	-2,9

3.4.2 – Data analysis

A MATLAB script was used to read the FIDs and phase them before calculating the ADC values. A direct FID correction scheme was used, which is based on the assumption that a signal will have maximal amplitude when in-phase. An inverse Fourier transformation of the corresponding spectral area yields the FID which corresponds to this signal. One may then calculate the difference between the signal's actual and maximal amplitude in order to obtain the phase angle ϕ required to phase the spectrum. After FID processing the signal attenuation

was measured as a function of b-value. The signal attenuation was then used to calculate the ADCs of the metabolites.

3.5 – Pulse Sequences

The pulse sequences used for both the construction of calibration curves and the diffusion measurements are PRESS and a diffusion-weighted MEGA-PRESS.

3.5.1 – PRESS

PRESS (*Point RESolved Spectroscopy*) is a single-voxel spin-echo technique which utilizes slice-selective gradients G_x, G_y and G_z along the three axes so that excitation only happens at the intersection of the three axes, causing the resonance condition to only be met inside the defined voxel. A CHESS[38] sequence is run at the start of acquisition to minimize the water signal's dominance on the spectrum. The offsets of all protons inside the voxel are refocused, and coupling are *J*-modulated.
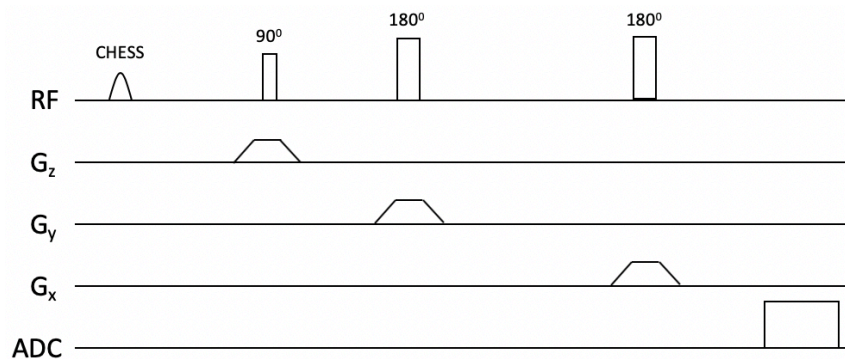
Figure 33 - The PRESS sequence[8]

Table 12 – Acquisition parameters shared for all pulse sequences

Parameter	Value
TR	5000 ms
AQ	10m42s
Voxel size	3x3x3 mm^3
Averages	128
Acquisition points	4096

3.5.2 – Diffusion-weighted MEGA-PRESS

Original:

The original diffusion-weighted MEGA-PRESS method achieves dephasing and rephasing through modified spoiler gradients placed around the hard 180° and at t=t1 and t=t5. The gradients are applied along all three axes so that one may measure diffusion in the desired direction. In this thesis the diffusion is only measured along the *z*-axis.
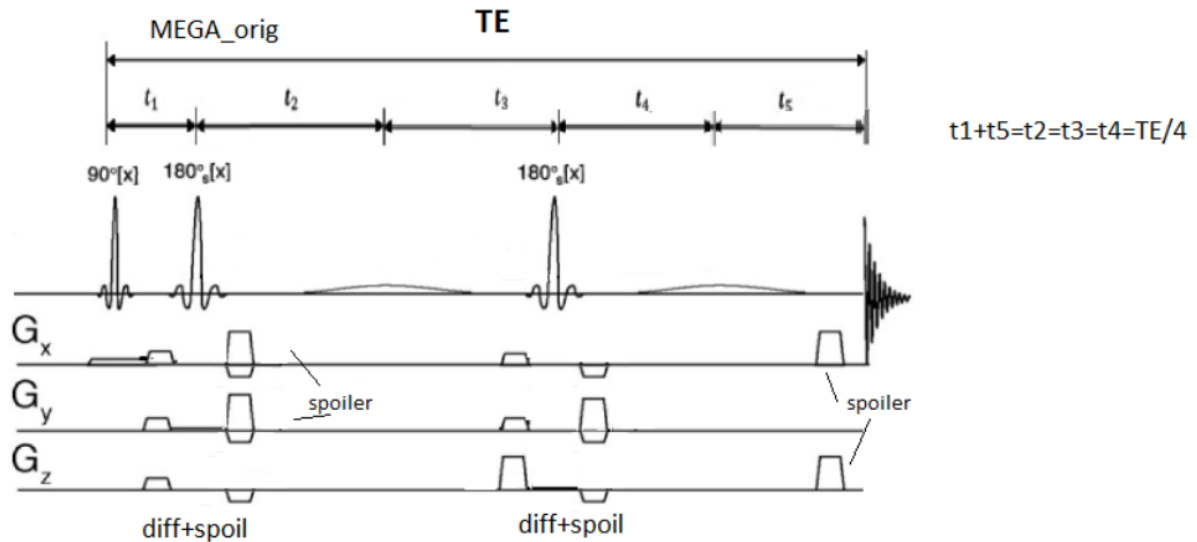
Figure 34 - Diffusion-weighted MEGA-PRESS sequence based on the original sequence.

The timings are shown on the right-hand side of the illustration. The "diff + spoil" gradients are applied along the z-axis. TE = 68ms

Siemens-*based MEGA-PRESS*:

The *Siemens*-based method is similar to the original method, but it features fewer spoilers around the second hard refocussing pulse. The timings are also different.
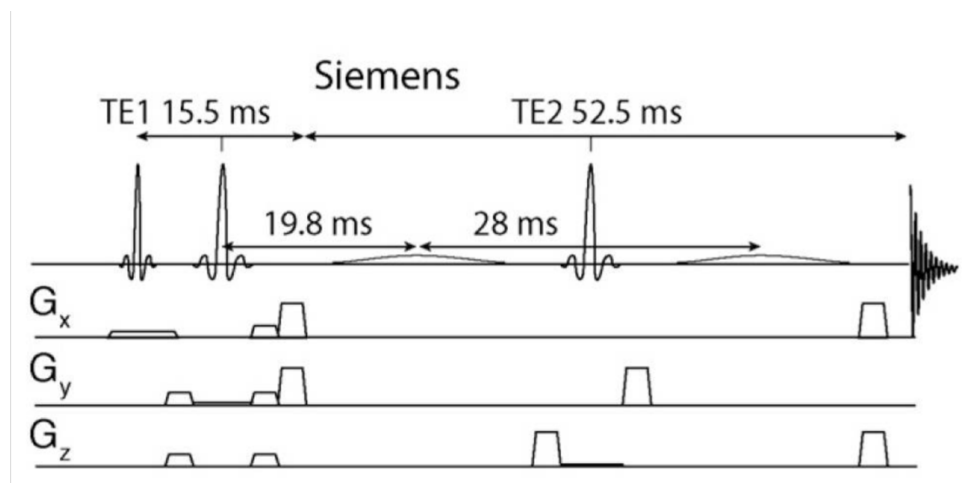
Figure 35 - The Siemens-based diffusion-weighted MEGA-PRESS sequence[39]

Similarly to the original-based diffusion-weighted MEGA-PRESS sequence, the diffusion spoilers are applied along the z-axis. TE = 68 ms

3.5.3 – Degree of refocussing in the MEGA-PRESS sequence

Both MEGA-PRESS sequences rely on two selective editing pulses in order to completely refocus the coupling so as to effectively hinder J-evolution of the MOI. If only one of these pulses is on resonance, there will be a partial refocussing of the coupling. The thought behind applying only one editing pulse is that the second pulse could, theoretically, target a second, different MOI resonance. There would thus be a trade-off between signal phase and editing capability of the pulse sequence. Below is a POF approach to a dual-editing scheme. For simplicity the second editing pulse is simply assumed to be turned off.

In the original MEGA-PRESS sequence, assume that a $90°x$ pulse has been applied to equilibrium magnetisation. The resulting magnetisation is described by the product operator - $\hat{I}_{Iy}$. Due to the hard $180°$ pulses, the evolution of chemical shifts is refocussed and is thus ignored. The coupling evolves for a time t' = t1 + t2 = (4 + 17) ms = 21 ms.

$$-\hat{I}_{1y} \xrightarrow{2\pi J_{12}\hat{I}_{1z}\hat{I}_{2z}} -\cos(\pi J_{12}t')\hat{I}_{1y} + \sin(\pi J_{12}t')\, 2\hat{I}_{1x}\hat{I}_{2z}$$

The effect of the editing pulse may be described as a $180°x$ pulse applied to spin 2.

$$\xrightarrow{\pi\hat{I}_{2x}} -\cos(\pi J_{12}t')\hat{I}_{1y} - \sin(\pi J_{12}t')\, 2\hat{I}_{1x}\hat{I}_{2z}$$

Because there is no second editing pulse, the coupling evolves freely for period t" = t3 + t4 + t5 = (17 + 17 + 13) ms = 47 ms. Looking at the terms separately:

i. $\quad -\cos(\pi J_{12}t')\hat{I}_{1y} \xrightarrow{2\pi J_{12}\hat{I}_{1z}\hat{I}_{2z}} -\cos(\pi J_{12}t'')\cos(\pi J_{12}t')\,\hat{I}_{1y} +$
$$\sin(\pi J_{12}t'')\cos(\pi J_{12}t')\, 2\hat{I}_{1x}\hat{I}_{2z}$$

ii. $\quad -\sin(\pi J_{12}t')\, 2\hat{I}_{1x}\hat{I}_{2z} \xrightarrow{2\pi J_{12}\hat{I}_{1z}\hat{I}_{2z}} -\cos(\pi J_{12}t'')\sin(\pi J_{12}t')\, 2\hat{I}_{1x}\hat{I}_{2z} -$
$$\sin(\pi J_{12}t'')\sin(\pi J_{12}t')\,\hat{I}_{1y}$$

The terms for $-\hat{I}_{Iy}$ and $2\hat{I}_{Ix}\hat{I}_{2z}$ become:

i. $\quad [-\cos(\pi J_{12}t'')\cos(\pi J_{12}t') - \sin(\pi J_{12}t'')\sin(\pi J_{12}t')]\,\hat{I}_{1y}$

ii. $[\sin(\pi J_{12} t'') \cos(\pi J_{12} t') - \cos(\pi J_{12} t'') \sin(\pi J_{12} t')] 2\hat{I}_{1x}\hat{I}_{2z}$

J_{12} for the GABA triplet and pseudo-triplet is approximately 7.3 Hz. Because triplets may be expressed as doublets precessing at twice the speed of the internal singlet, the phase angle is multiplied by a factor of two. The two phase angles need to be calculated and solved for expression (i) and (ii).

i. $\theta_1 = 2\pi J_{12} t' = 2\pi * 7.3\ Hz * (4 + 17)\ ms = 0{,}306\pi$

ii. $\theta_2 = 2\pi J_{12} t'' = 2\pi * 7.3\ Hz * (17\ +\ 17\ +\ 13)\ ms\ =\ 0{,}686\pi$

Thus, substitution gives the following state of the spin system at the start of acquisition:

$$-0.36\ \hat{I}_{1y} + 0.93\ 2\hat{I}_{1x}\hat{I}_{2z}$$

It can be seen that the signal will be dominated by anti-phase magnetisation.

In the *Siemens*-based sequence, the timings are: t1=7.75, t2= 19.8, t3 = 14, t4= 14, t5 = 12.45. This gives the following phase angles:

i. $\theta_1 = 2\pi J_{12} t' = 2\pi * 7.3\ Hz * (7.75 + 19{,}8)\ ms = 0.402\pi$
ii. $\theta_2 = 2\pi J_{12} t'' = 2\pi * 7.3\ Hz * (14\ + 14\ +\ 12.45)\ ms = 0.591\pi$

Which gives the following state of the spin system at the start of acquisition.

$$-0.65\ \hat{I}_{1y} + 0.56\ 2\hat{I}_{1x}\hat{I}_{2z}$$

Contrary to the original-based sequence, the *Siemens*-based sequence yields a signal that is mostly comprised of in-phase magnetisation, but the anti-phase magnetisation component is still significant.

3.6 – Experimental challenges

As this thesis has regarded itself with method testing of a new pulse sequence, it is prudent to give a robust description of what did *not* work as planned.

3.6.1 – Hardware/software problems

As with all types of measurements, NMR acquisitions rely on hardware and software working perfectly together in order to obtain good quality of data. Sadly, several challenges presented themselves along the way. Initially, *ParaVision* was unable to read the correct shim file from *TopSpin*, causing shimming errors. A new shim file with the appropriate parameters was constructed, and it was read manually in *TopSpin* prior to acquisition. This, however, still often led to a localized shimming protocol failing in *ParaVision*. Acquisition was still possible by using a built-in shimming function in the PRESS and MEGA-PRESS routines, but in these cases water suppression was of poor quality as the presaturation schemes rely on good shimming beforehand. Therefore, a lot of experiments were simply discarded as the water suppression failed, causing the water signal to completely dominate the metabolite signals. The problem was eventually solved so that acquisitions with adequate water suppression could be run.

Other problems presented themselves in relation to the NMR hardware, as the RF cable became partly broken and unstable. Although a workaround of this issue was eventually found it led to a lot of wasted experimental time, and the cable became more and more damaged from use, so that in the end changing samples became very difficult. Things were not made any easier when the matching and tuning of the probe started to cause the *ParaVision* to freeze, requiring a full system reboot. All in all, these hardware- and software problems spanned over the entire experimental period, which unfortunately resulted in a lot of time wasted and acquisitions ruined.

3.6.2 – Calibration curves

The calibration curve experiments were performed at the very start of this project in order to ascertain a good linear response of the measurement as theory predicts. Metabolite solutions were prepared using a commercial biological phosphate buffer which had too low of a buffer capacity, which caused the metabolite solution to have a pH value of around 3.6, which is far below *in vivo* levels. Since NMR is pH-sensitive and the metabolites are all acids, this unexpected deviation in pH was concerning. Therefore, a new in-house phosphate buffer solution with a much higher buffer capacity was prepared for the rest of the experiments. The pH of the metabolite solutions in this new buffer was in the range of 7.2-7.4, which was deemed acceptable.

Furthermore, the MEGA-PRESS method is supposed to be able to edit two different resonances during the same sequence, and this was attempted by applying only one of the editing pulses onto the GABA-H$_B$ resonance in the ON-experiment. Due to uncertainty regarding the resulting spectra, a new calibration curve was constructed with both editing pulses targeting the same resonance to compare the effects of dual- vs single-editing MEGA PRESS.

3.6.3 – Diffusion Measurements

Where diffusion measurements are concerned, there were several challenges relating to both acquisition and data analysis. Originally, a sequence based on the *Siemens* MEGA-PRESS using an MFG amplitude duration of $\delta = 1$ ms was used. Another pulse sequence based on the original MEGA-PRESS with $\delta = 3$ was used for comparison, as this is a more realistic duration for *in vivo* acquisitions. The code used to analyse the diffusion results had to be changed, as the tripling of δ leads to a ninefold increase in signal attenuation (δ^2). As with the calibration curves, a dual-editing scheme was attempted for diffusion measurements as well. Due to the similar concerns, single-experiments were run with both editing pulses on the GABA-H$_B$ resonance.

Several phasing methods were used in the analyses. In the end a direct FID correction scheme was used. Most of the data analysis had to be repeated several times when the phasing method changed.

4 Results

4.1 – Calibration curves

Because the theoretical curve varied between experiments (due to different concentrations), all calibration curve slopes were normalized with respect to the theoretical curve.

Table 13 - Normalised calibration curve slopes

Experiments marked with an asterisk (*) feature complete refocussing.

EXPERIMENT	GABA HA/T	GABA HC/T
GABA/NAA p1 (*Siemens*)	0,7156	0,9247
GABA/NAA/Cr p1 (*Siemens*)	0,4985	0,7889
GABA/NAA/Cr p2 (*Siemens*)	0,7440	0,9796
Full metabolite solution* (Original)	0,8492	0,8597
GABA/NAA p2 (Original)	0,2954	0,2186
GABA/NAA p2* (Original)	0,8932	0,8064
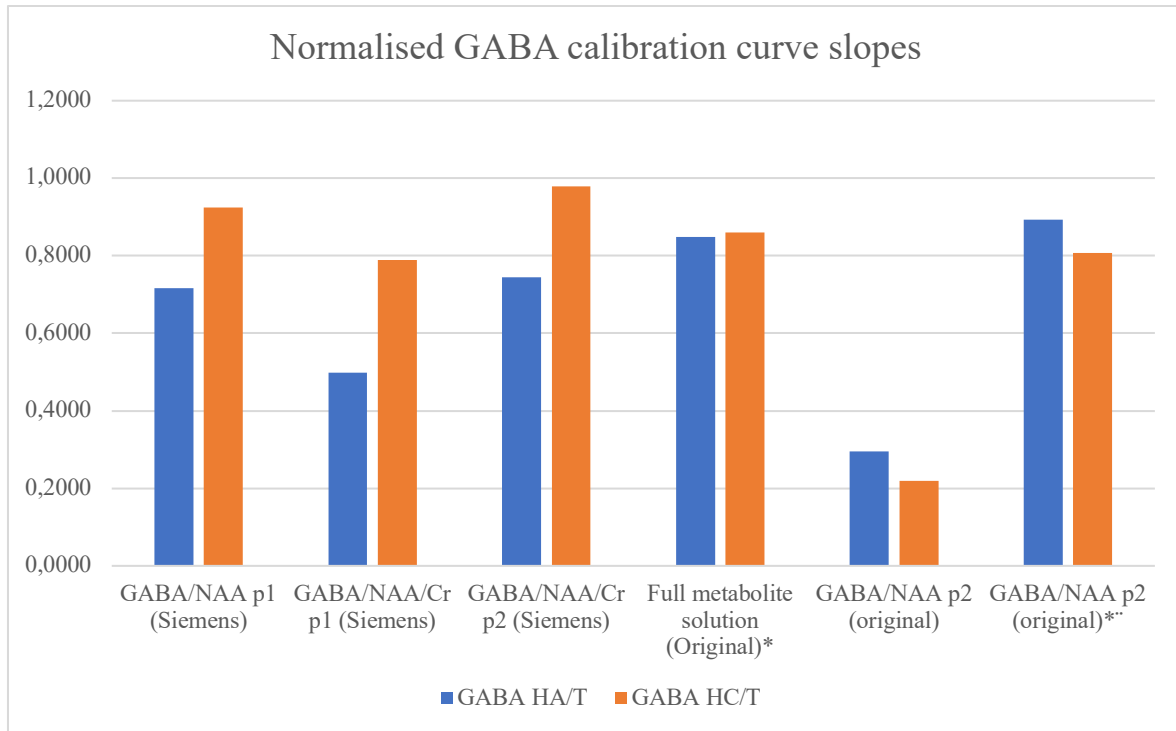
Figure 36 - Comparison of normalized GABA calibration curve slopes

*Experiments marked with * are completely refocussed, the others are only partially refocussed.*

4.1.1 GABA/NAA parallel 1 (*Siemens*, partial refocussing)
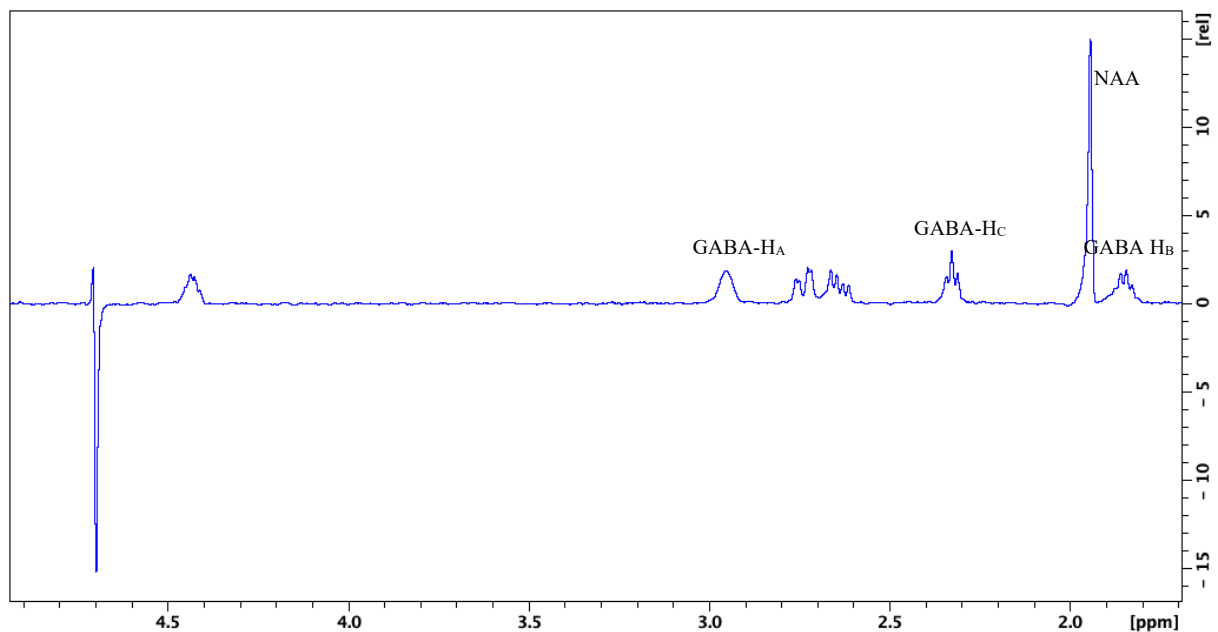
Figure 37 – PRESS spectrum; GABA/NAA Siemens p1

TE = 16.168 ms. LB = 3.00. Notice the shape of GABA-H_A, which is supposed to be a pseudo-triplet.
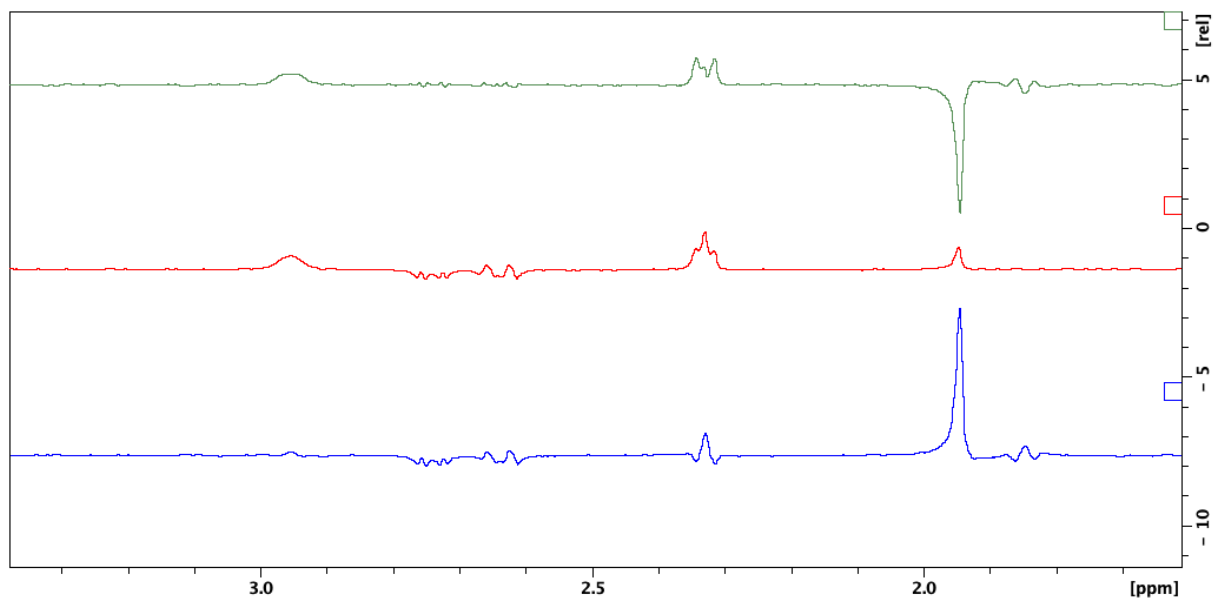
Figure 38 - MEGA-PRESS experiment for GABA/NAA p1 (Siemens, partial refocussing)

TE = 68 ms; LB = 3.00
The blue spectrum corresponds to the OFF- spectrum, red to the ON- spectrum & green the J-difference (DIFF)
spectrum.
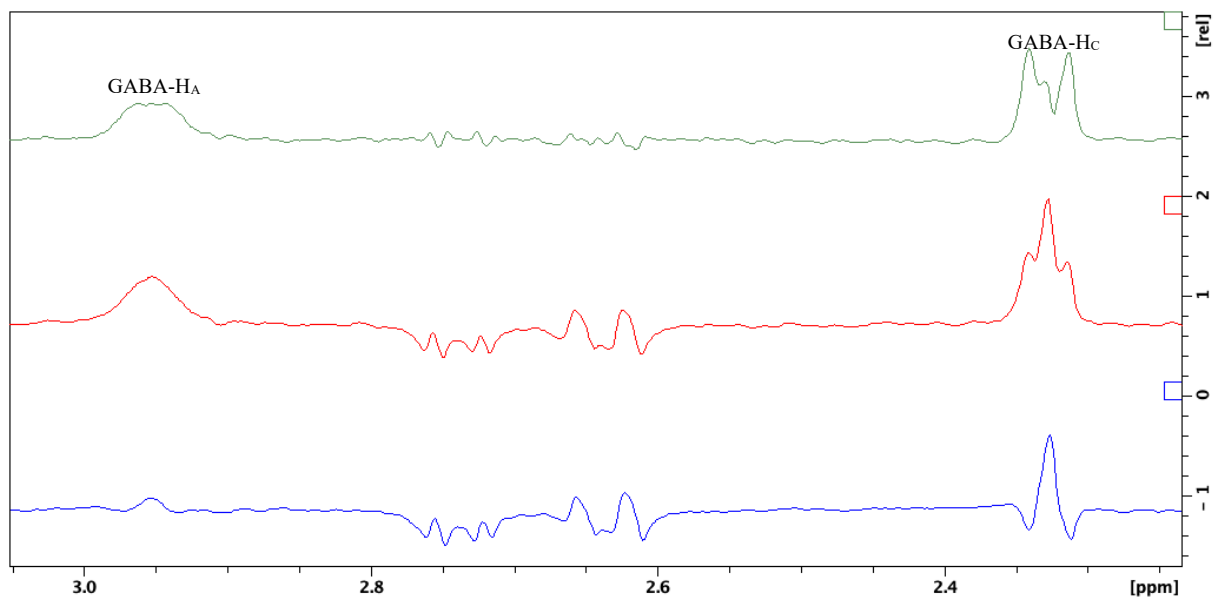
Figure 39 - GABA HA and HC resonances in the MEGA-PRESS experiment for GABA/NAA p1 (Siemens, partial
refocussing)

TE = 68 ms ; LB = 3.00
Blue = OFF, red = ON, green = DIFF
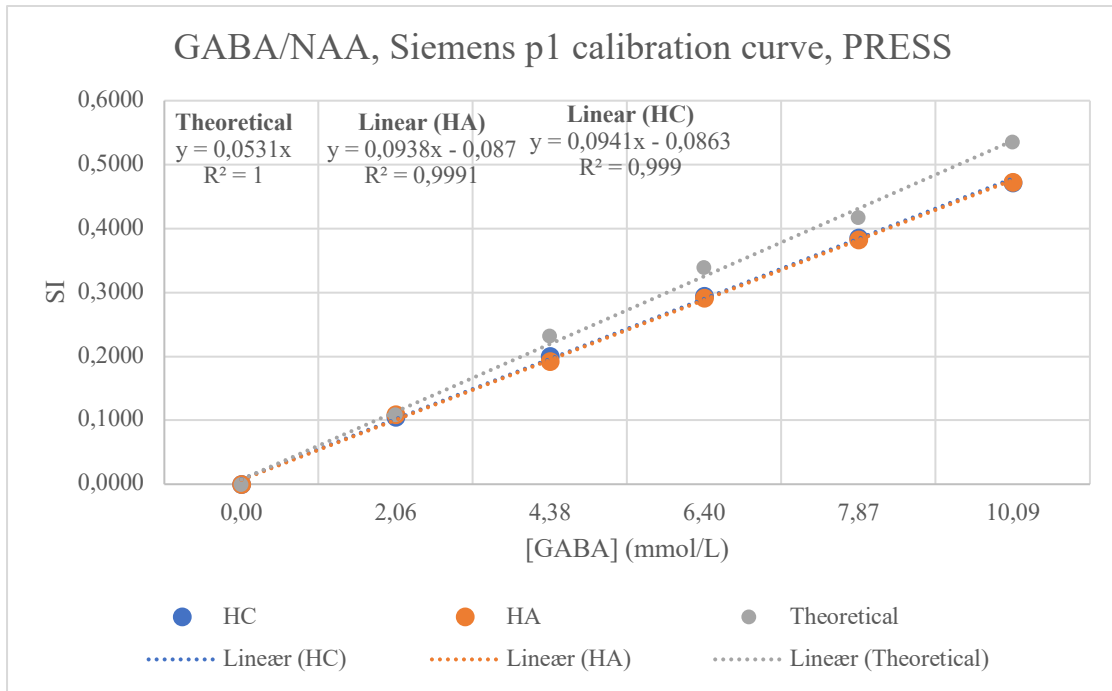
*Figure 40 – GABA/NAA p1 (*Siemens*, partial refocussing) calibration curve based on the PRESS sequence*

GABA concentration is plotted against measured SI of the GABA-HA and GABA-HC resonances. Some of the datapoints are completely overlapping. Notice that both calibration curves deviate similarly from the theoretical curve.
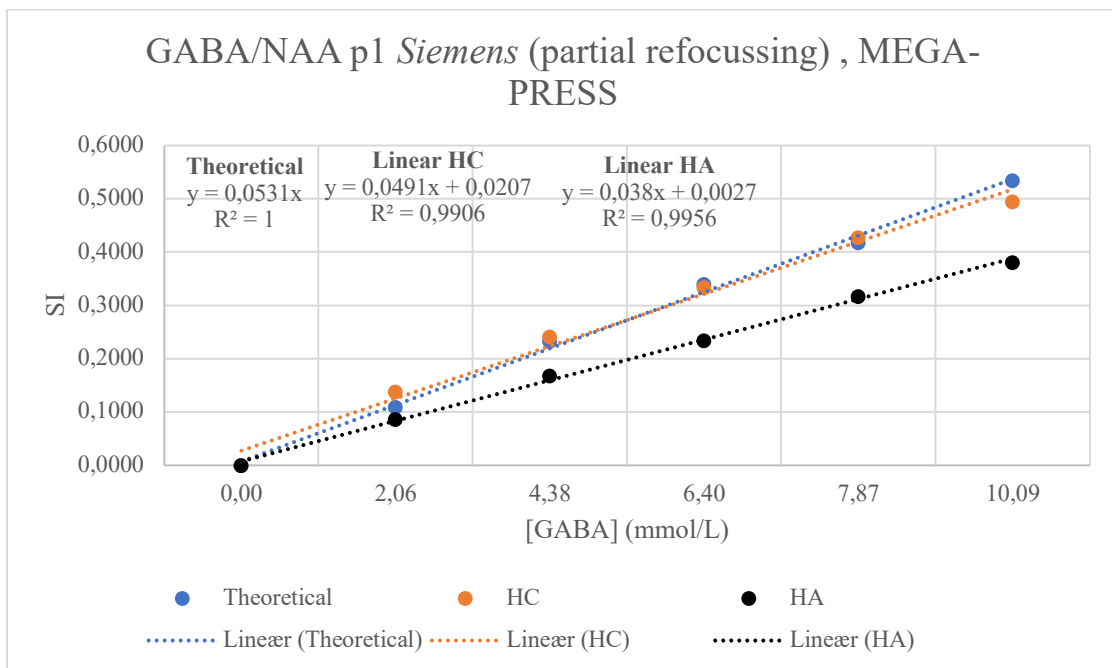
Figure 41 - GABA/NAA p1 calibration curve based on the Siemens MEGA-PRESS sequence with incomplete refocussing.

GABA concentration is plotted against the measured signal intensity of the edited, partially refocussed signals. Notice how the GABA-H_A curve deviates from the theoretical curve compared to the GABA-H_C curve.

4.1.2 - GABA/NAA p2 (original sequence)
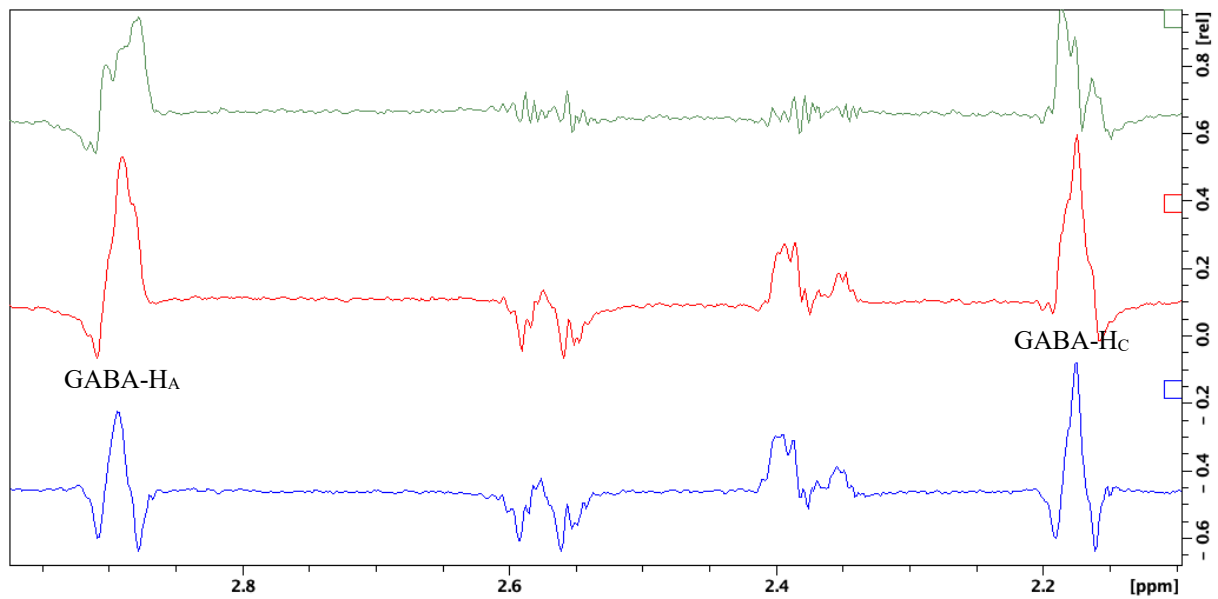
Figure 42 - MEGA-PRESS for GABA/NAA p2 (original) with incomplete refocussing

Blue = OFF, red = ON, green = DIFF
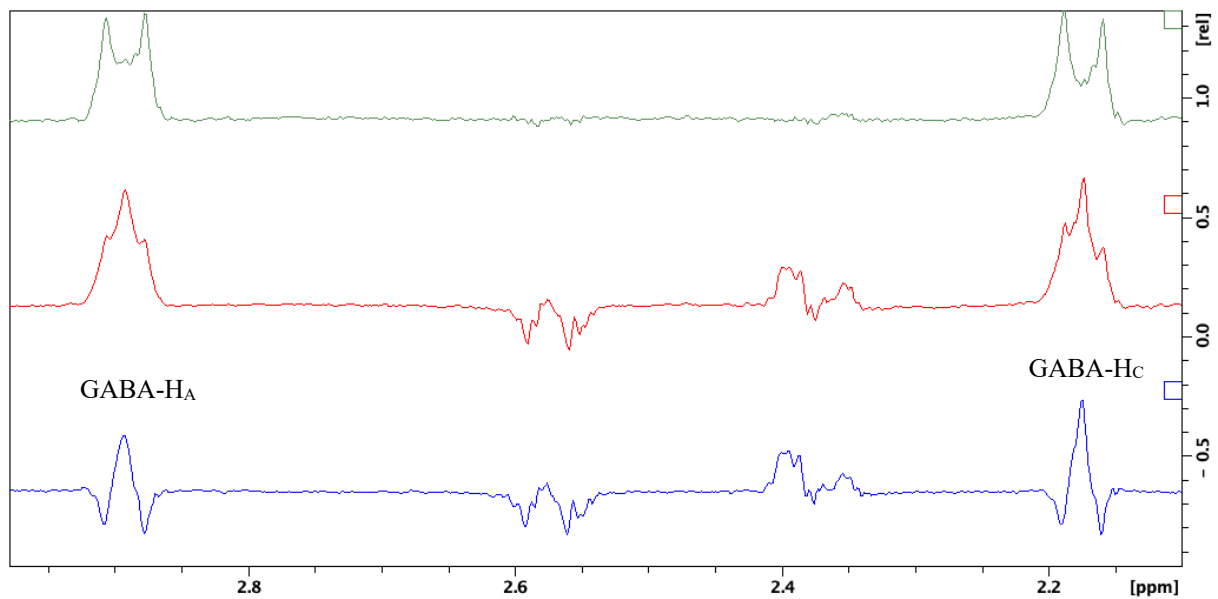
Figure 43 - MEGA-PRESS experiment for GABA/NAA p2 (original) with complete refocussing

TE = 68 ms
Blue = OFF, red = ON, green = DIFF
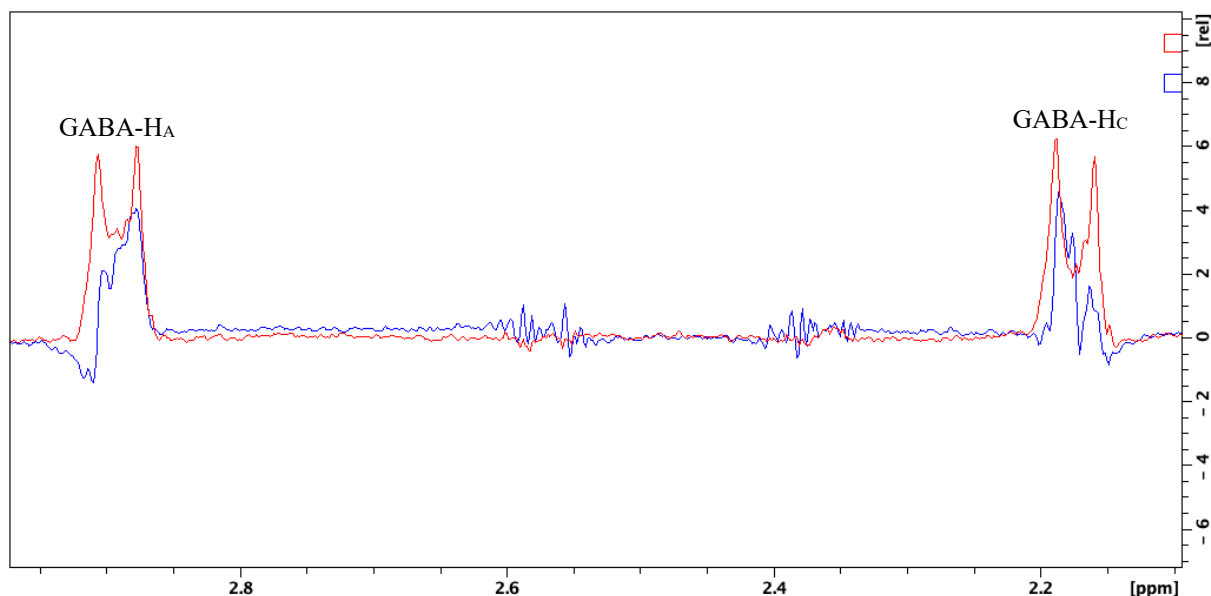
Figure 44 - Comparison of differently refocussed GABA resonances in the GABA/NAA p2 original experiment.

Red = complete refocussing (dual editing pulse), blue = incomplete refocussing (single editing pulse)
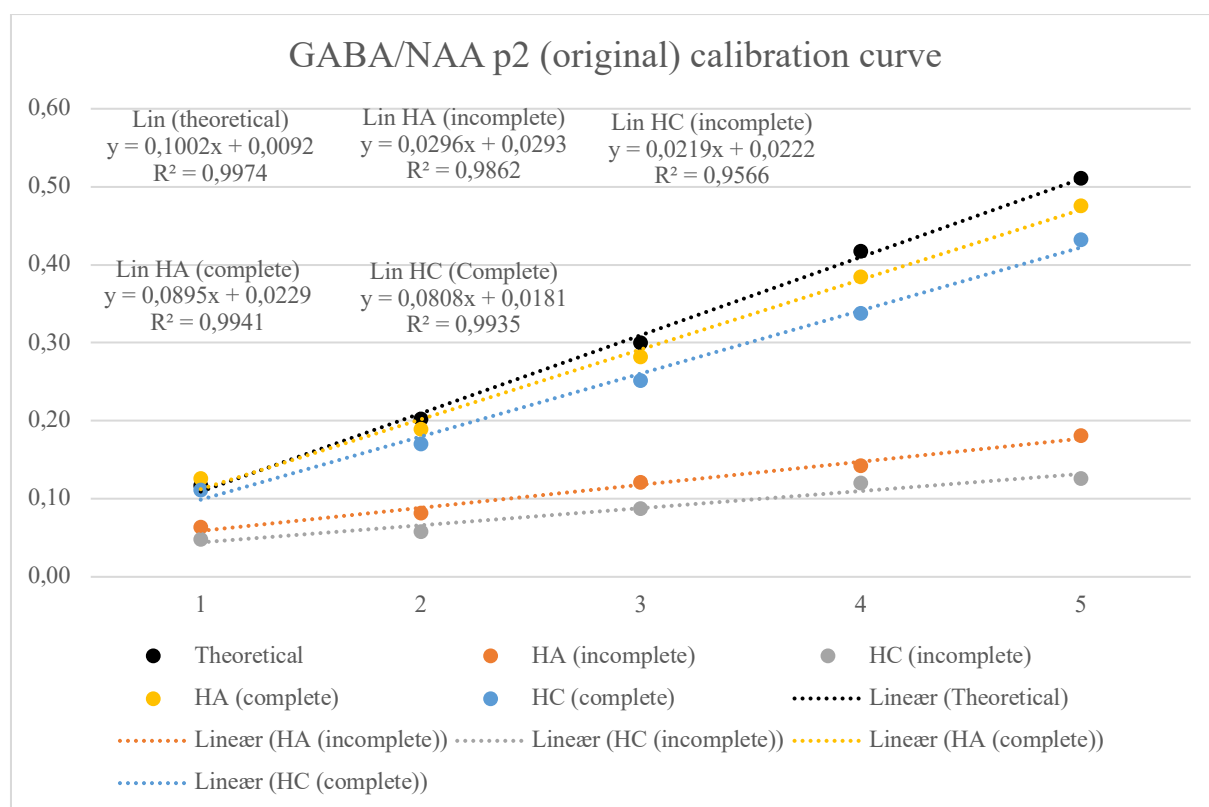
Figure 45 - GABA/NAA p2 (original) calibration curves

Calibration curves for both complete and incomplete refocussing are included. Notice how the curves based on incomplete refocussing deviate significantly from both the theoretical curve and the completely refocussed calibration curves.

4.2 – Diffusion Measurements

4.2.1 – Diffusion probe results
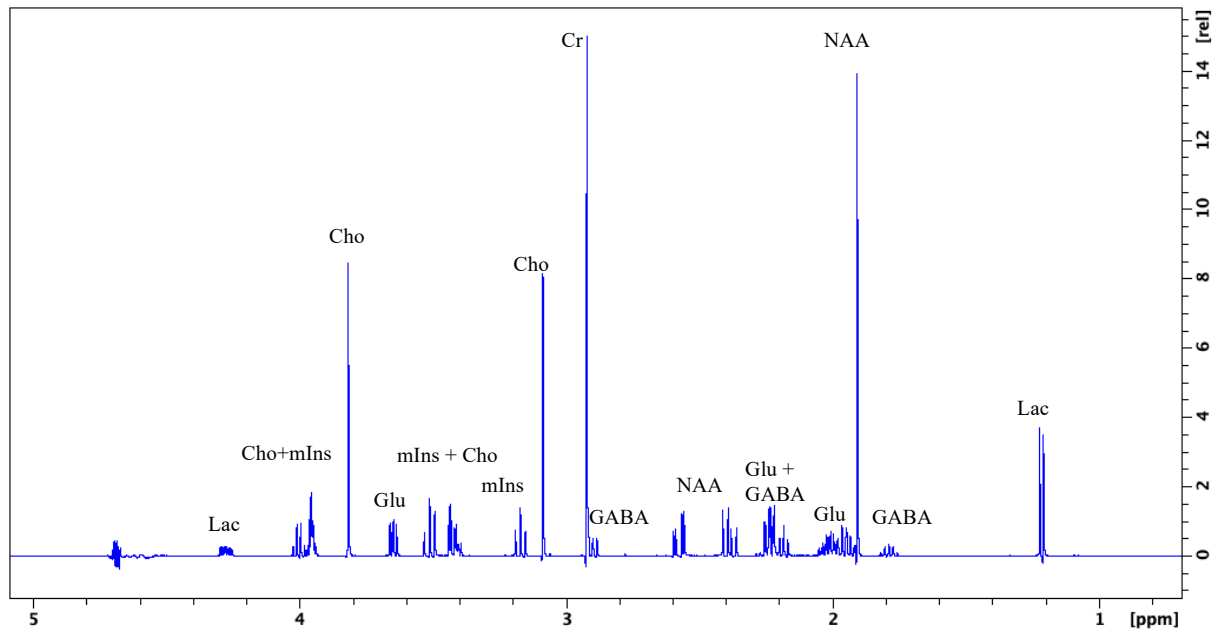
Equation 45 - Diffusion probe spectrum of brain metabolites with peak labels

Table 14 – Metabolite ADCs measured in the diffusion probe experiment

Metabolite	ADC
Water	2,30E-09
NAA	7,90E-09
Cr	9,50E-09
GABA	8,60E-09

4.2.2 – SVS diffusion measurements

The *Siemens*-based sequence features a MFG pulse with δ = 1 ms so that the attenuation is rather slow. These experiments therefore contain 11 data points (0 – 3% at intervals of 3%). The MATLAB code yields a waterfall plot that shows the signal attenuation as a function of z-axis diffusion gradient strength.
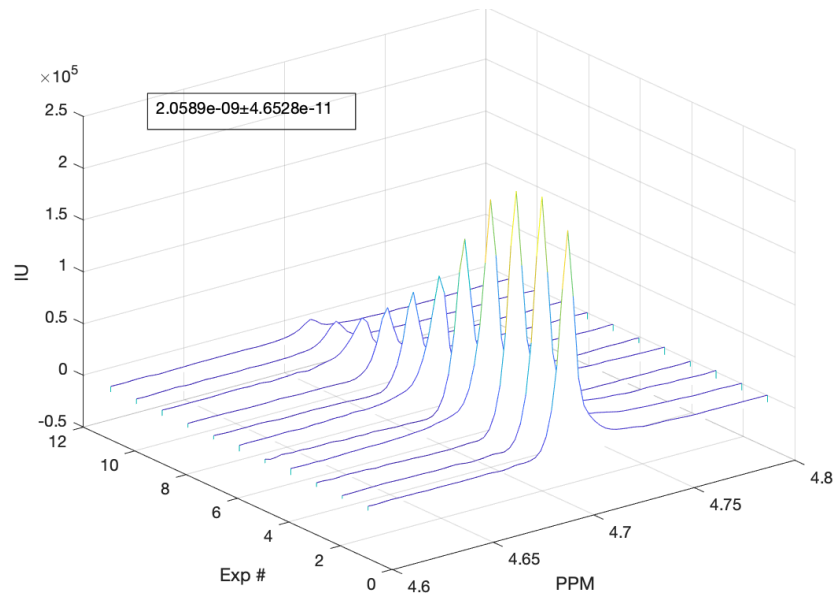
Figure 46 – Attenuation of the water signal in the GABA p1 Siemens experiment with incomplete refocussing.

The signal intensity decreases for each experiment as the diffusion gradient strength increases.
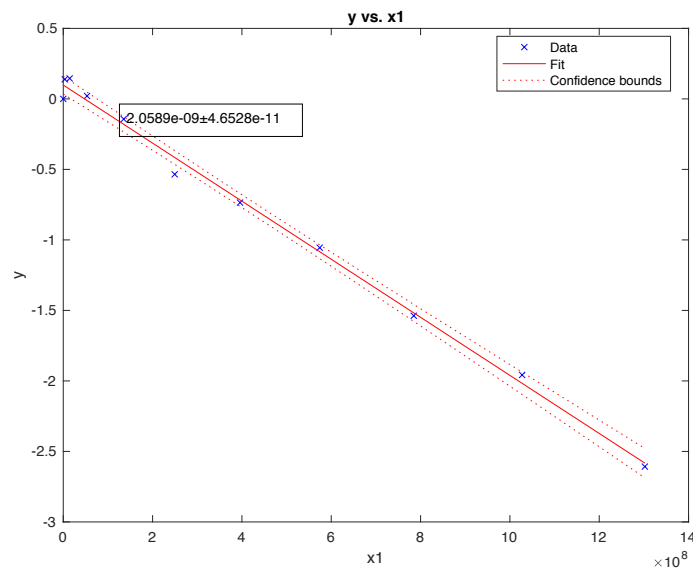
Figure 47 – Linear plot of water signal attenuation as a function of diffusion.

*The slope is used to calculate the ADC according to **Eq. 42**. These linear plots were helpful in locating eventual outliers which had to be removed from the experiments. All removed outliers for each experiment are included in Appendix B.*
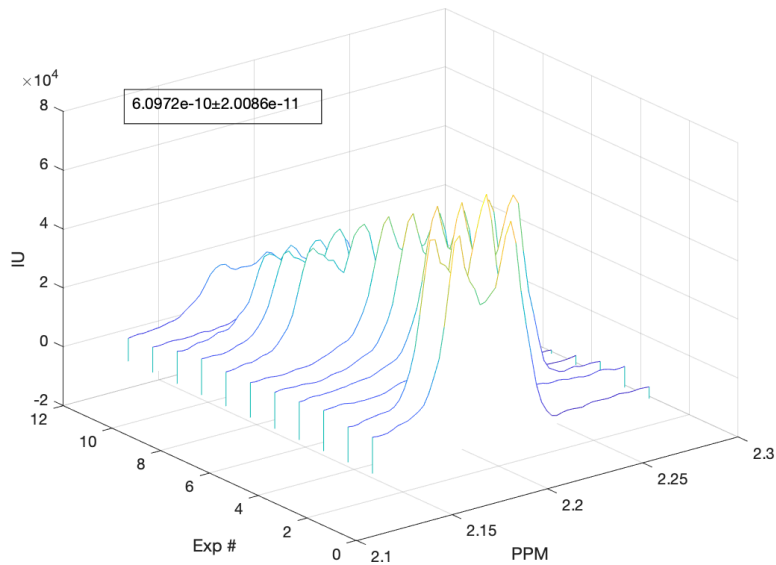
Figure 48 - Attenuation of GABA-HC signal in the Siemens-based MEGA-PRESS (GABA/NAA/Cr Siemens p1 experiment with complete refocussing)

The figure shows the edited GABA-H$_C$ resonance. The chemical shift displacement between experiments has no effect on the measurement if the ppm interval of integration is adequate.

The original-based MEGA-PRESS sequence features δ = 3 ms, so that the attenuation occurs 9 times faster than in the *Siemens*-based method. Therefore, only six datapoints were necessary to measure the diffusion as a function of z-gradient strength. Sometimes only five datapoints were necessary, in which case the sixth dataset was removed as it only contained noise which sometimes resulted in outliers.
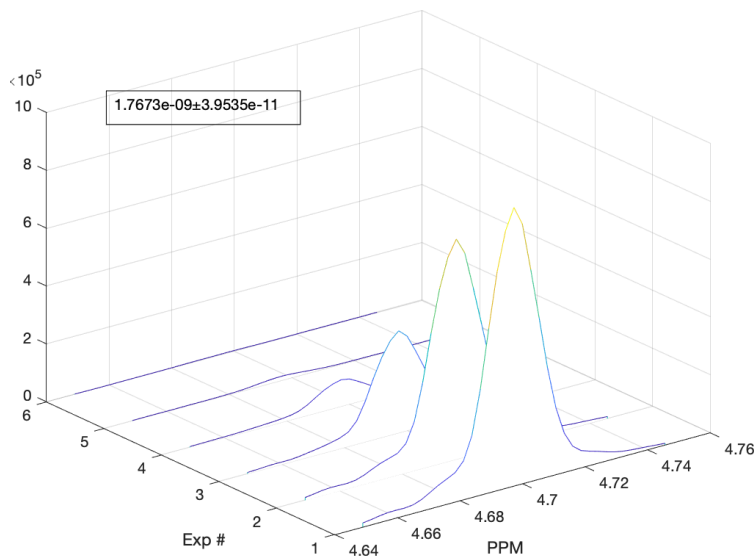
Figure 49 - Water resonance signal attenuation in the original-based MEGA-PRESS method (GABA/NAA/Cr original p1 with complete refocussing)

The signal attenuates at a much faster pace due to the increased MFG pulse width. The sixth acquisition is often excluded as there is no signal and sampling it simply introduces a reduction in SNR in the experiment.
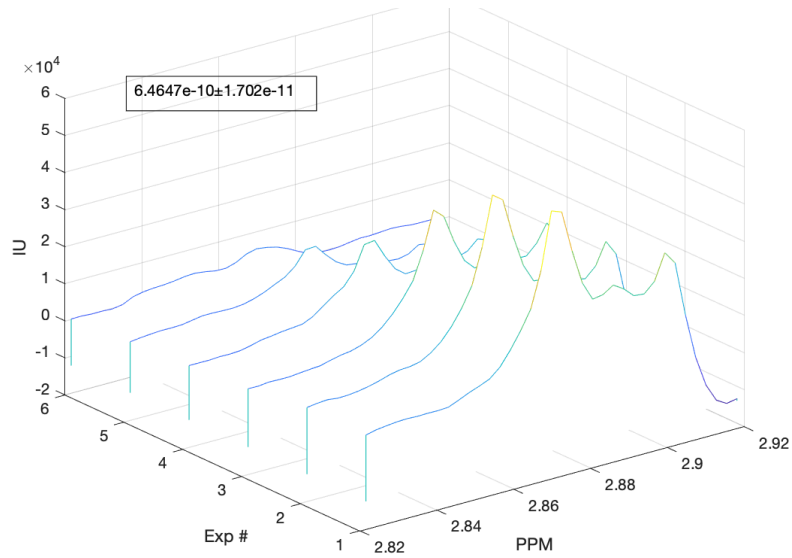
Figure 50 – Edited GABA-HA signal attenuation in the original-based MEGA PRESS (GABA/NAA/Cr original p1 with complete refocussing)
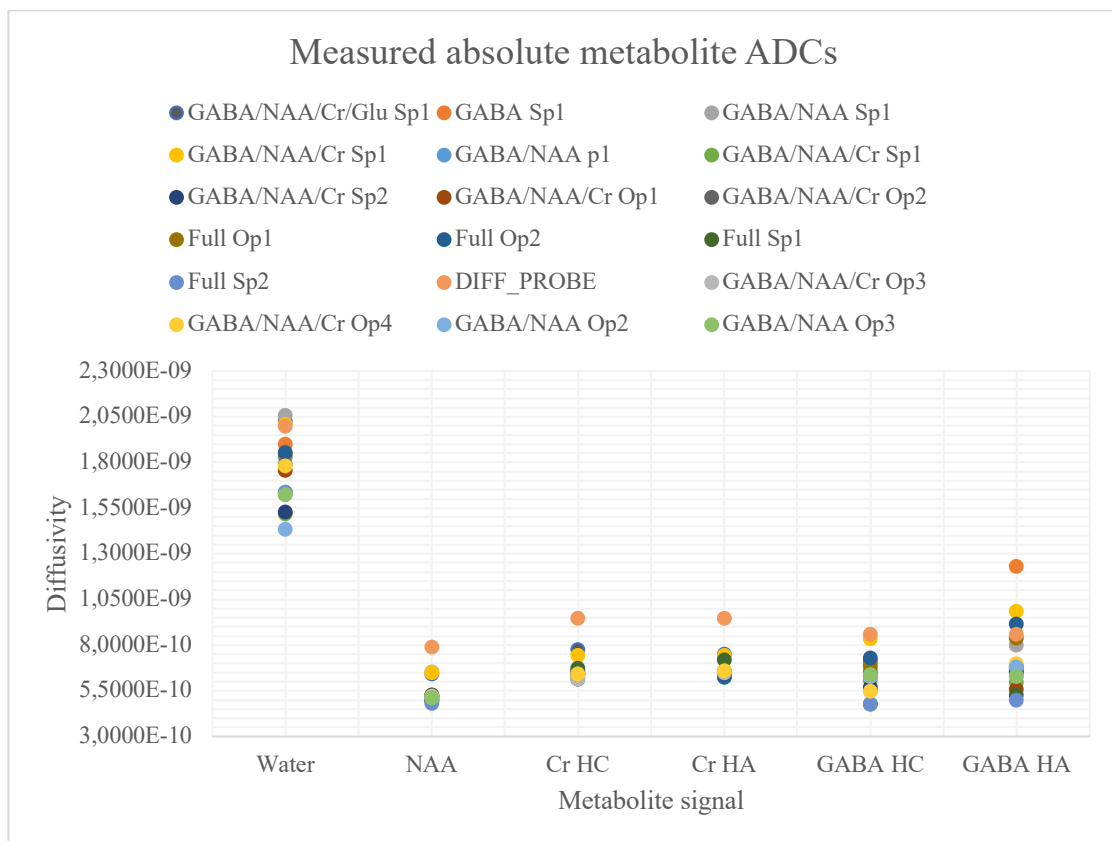
Figure 51 - Overview of all diffusion measurement results.

"Sp" = parallel based on the Siemens pulse sequence; "Op" = parallel based on the original pulse sequence "Full" = a solution with all the metabolites present.

Table 15 - Mean- and median metabolite ADC data

The GABA Sp1 experimental data for the GABA resonances are outliers and are therefore excluded from calculations.

Metabolite signal	ADC, mean	ADC, median	Standard deviation
Water	1,7702E-09	1,8117E-09	2,6630E-10
NAA	5,2280E-10	5,1977E-10	8,1762E-11
GABA-H_A	6,9971E-10	6,7072E-10	1,3674E-10
GABA-H_C	6,4140E-10	6,3373E-10	1,0512E-10
Cr-H_A	6,8975E-10	6,5665E-10	8,9391E-11
Cr-H_C	6,8593E-10	6,4500E-10	9,2085E-11
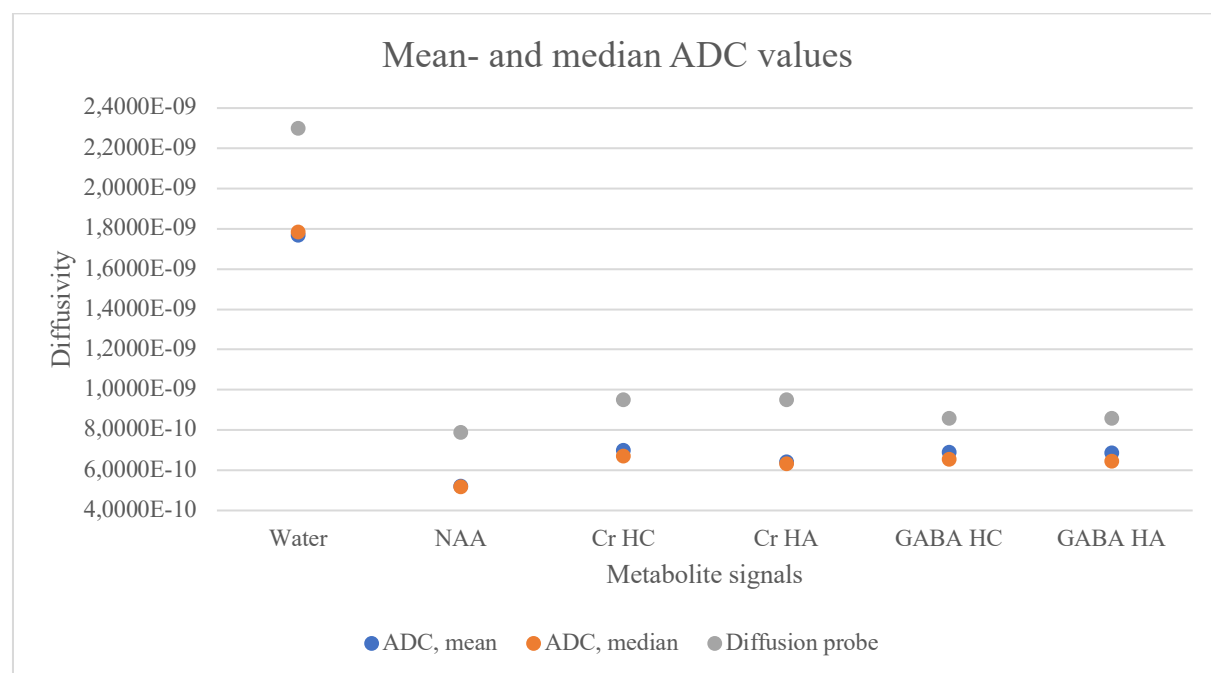
Figure 52 - Mean- and median metabolite ADC data based on absolute ADCs from each experiment.

Both mean and median values are included due to the variance seen in the data set, although there is not much of a difference between the two in terms of value.
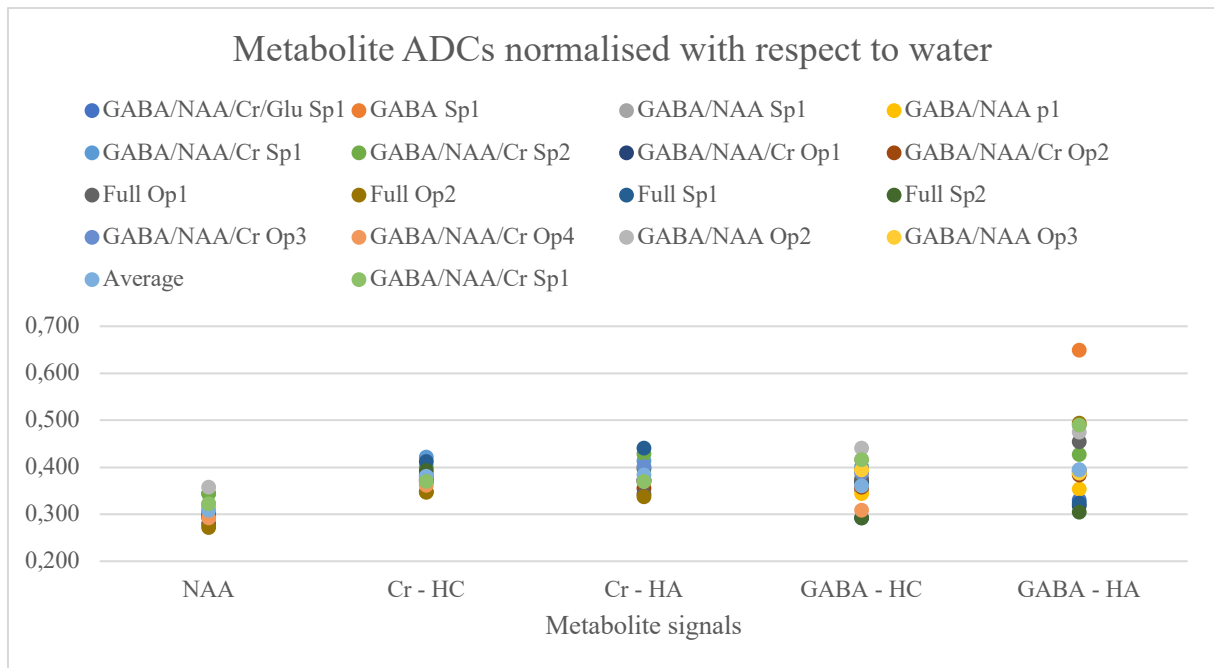
Figure 53 - ADC values normalised with respect to water

*The outlier on GABA-H$_A$ resonance is experiment GABA sp1 which measures the **unedited** GABA signal at 68ms.*
"Sp" = parallel based on the Siemens pulse sequence; "Op" = parallel based on the original pulse sequence
"Full" = a solution with all the metabolites present.
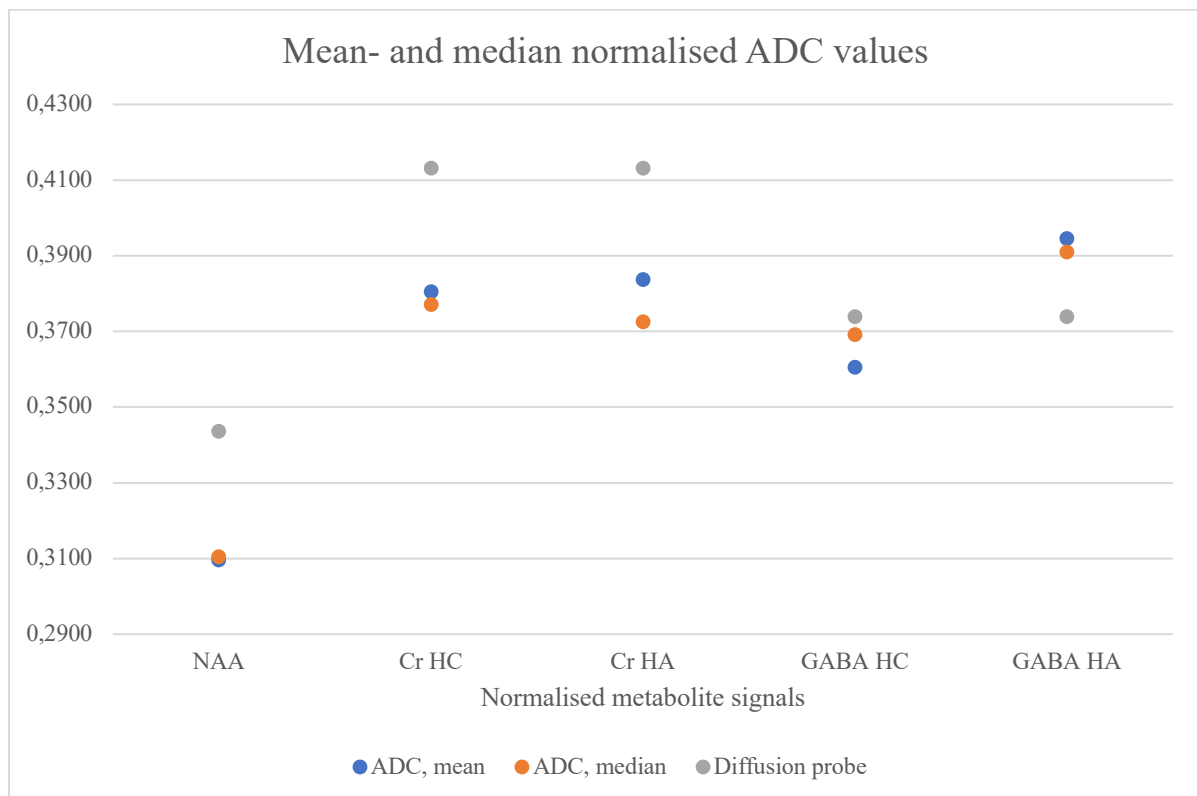
Figure 54 - Mean- and median values of normalised ADCs
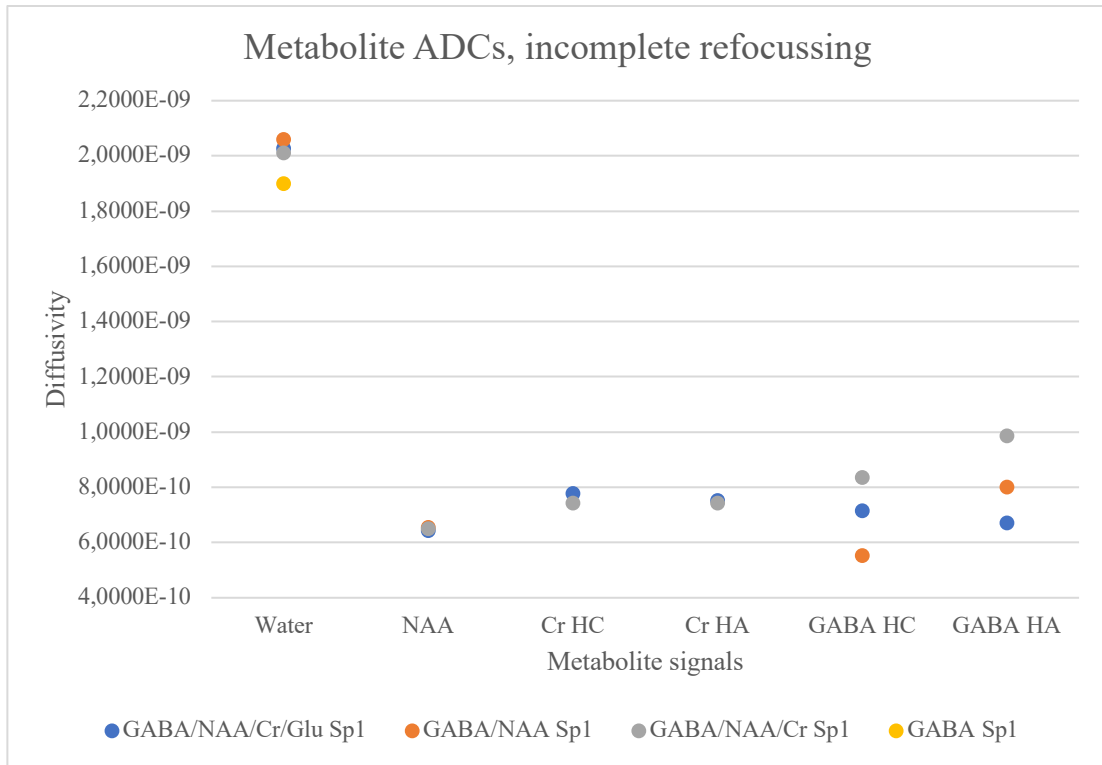
Figure 55 - Mean ADC values for experiments featuring incomplete refocussing

"Sp" = parallel based on the Siemens pulse sequence; "Op" = parallel based on the original pulse sequence
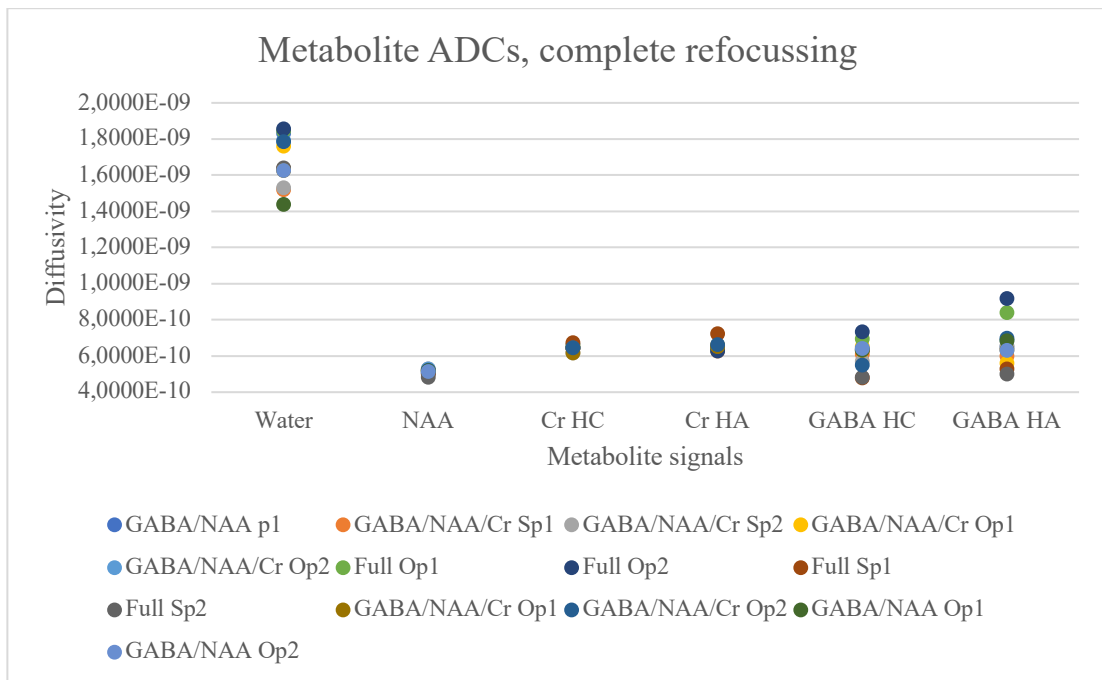
Figure 56 - Mean ADCs for experiments with complete refocussing

Notice the variance in measured water ADCs
"Sp" = parallel based on the Siemens pulse sequence; "Op" = parallel based on the original pulse sequence
"Full" = a solution with all the metabolites present.
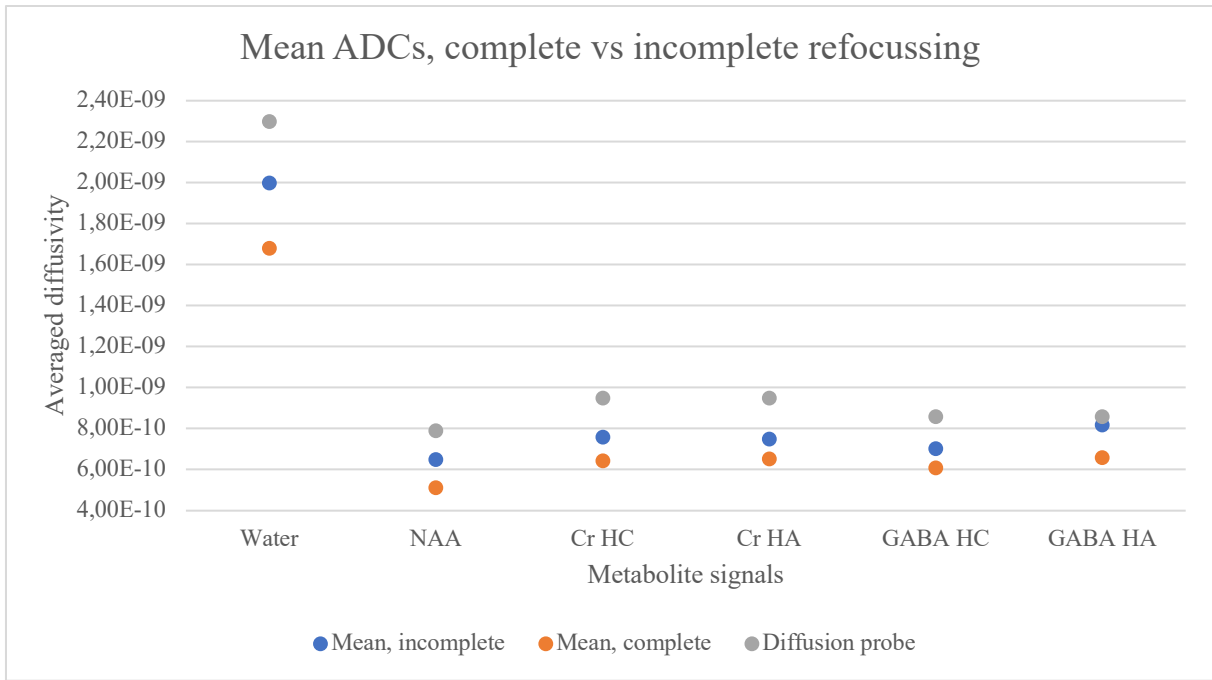
Figure 57 - Comparison of complete and incomplete refocussing effect on ADC
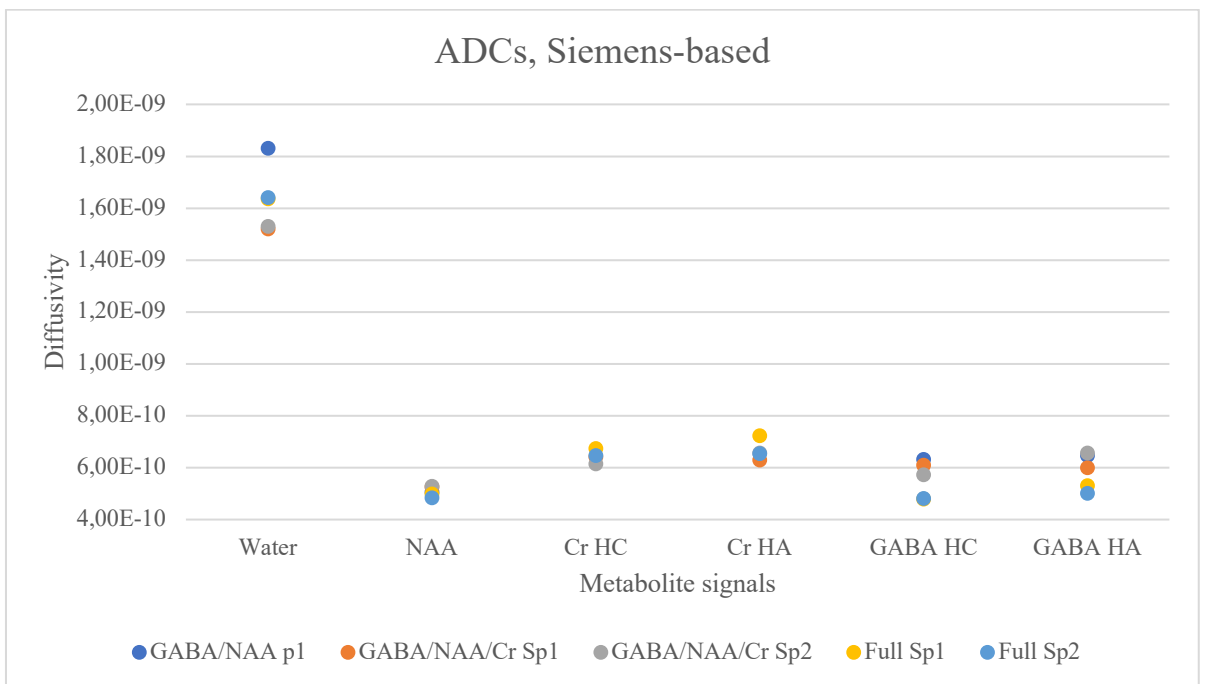
Figure 58 - ADCs from the Siemens-based experiments

"Sp" = parallel based on the Siemens pulse sequence; "Op" = parallel based on the original pulse sequence
"Full" = a solution with all the metabolites present.
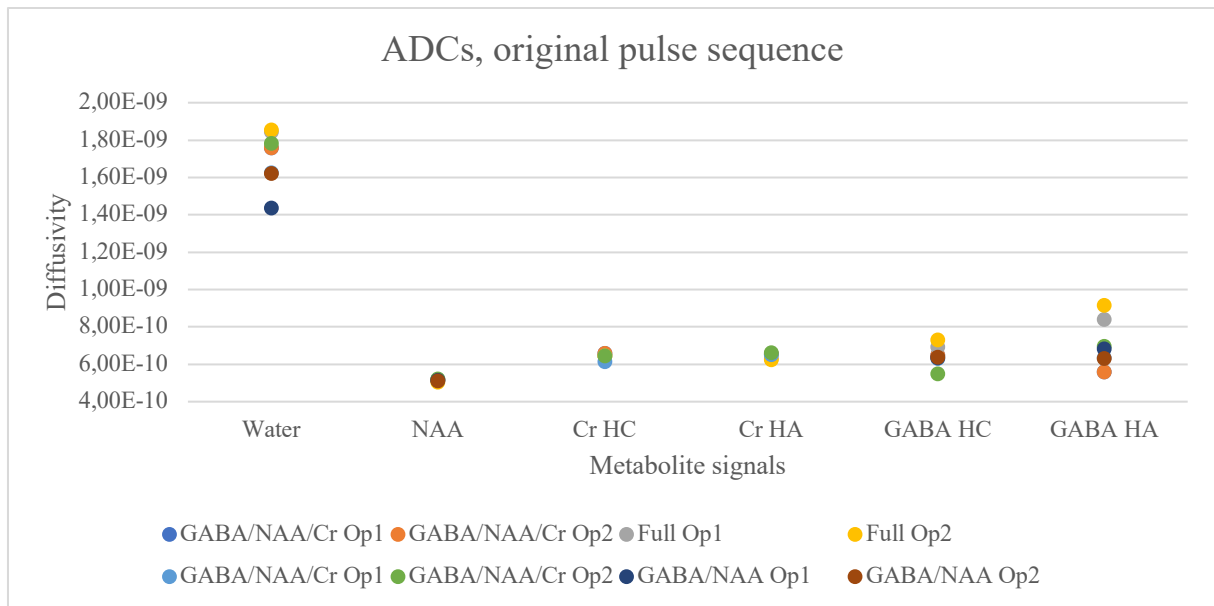
Figure 59 - ADCs from the original pulse sequence experiments

"Sp" = parallel based on the Siemens pulse sequence; "Op" = parallel based on the original pulse sequence
"Full" = a solution with all the metabolites present.
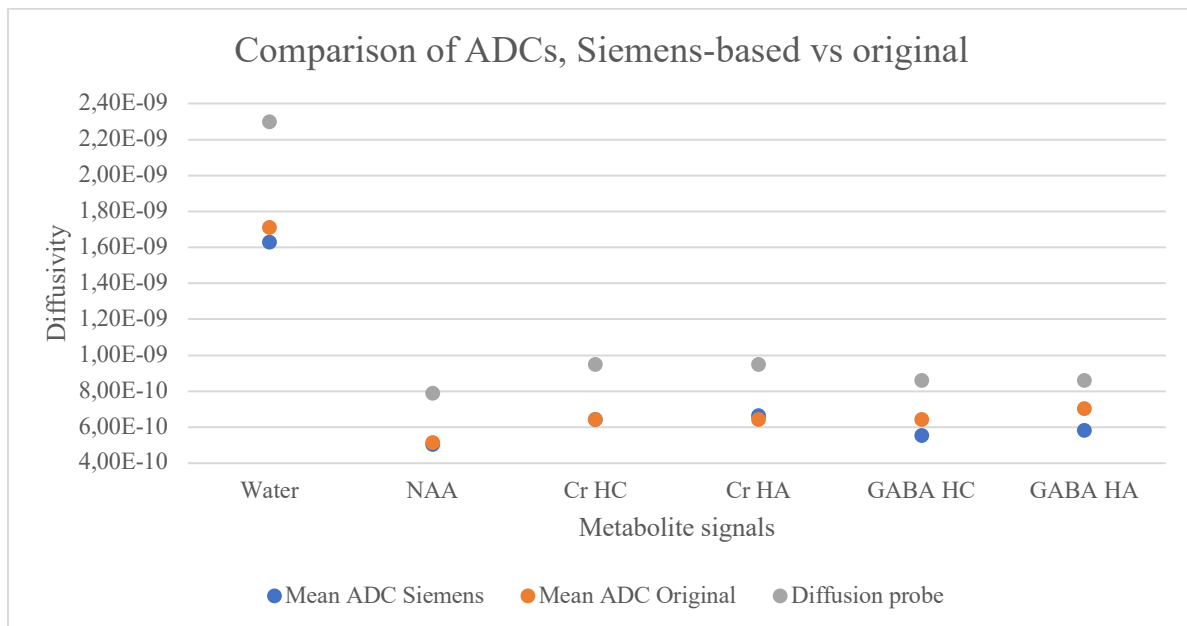
Figure 60 - Comparison of ADCs based on the two pulse sequences

No distinction is made between complete and incomplete refocussing in this comparison.

5 Discussion

5.1 – Calibration Curves

5.1.1 – PRESS calibration curves

The PRESS-based calibration curve systematically misrepresents both GABA resonances' S.I by approximately **-12%.** Lower signal is expected in single-voxel spectroscopy experiments

because the gradients used to select the voxel are not perfectly uniform. This leads to an uneven excitation of the voxel volume, which causes signal loss. Compared to PRESS, the STEAM sequence uses sharper 90° pulses for voxel selectivity, which results in more uniform selective excitation. However, due to the low concentration of GABA in the 2mM and 4 mM samples it is expected that the low SNR from STEAM would lead to larger quantification errors.

The MEGA-PRESS calibration curves show that the measured GABA S.I depends on the degree of refocussing in the sequence. The table below shows the amount of which the measured SI deviates from the theoretical SI in the calibration curve experiments. It is seen that, with complete refocussing, the original-based pulse sequence measures the SI with good precision. However, with incomplete refocussing the SI deviates largely from the theoretical SI. The misrepresentation of SI in the *Siemens*-based experiments is lower than those in the original-based. Sadly, no experiments featuring completely refocussed *Siemens*-based pulse sequences were run due to time constraints and technical difficulties (see section 3.6). *It is assumed that the Siemens experiments with complete refocussing would yield similar results to the original sequence, as the signal would be completely in-phase in both situations. Therefore the completely refocussed original-sequence results may be used as grounds for comparison.*

Table 16 – Average signal intensity deviations in the calibration curve experiments
No Siemens-based experiments with complete refocussing were run due to time constraints.

Resonance	Incomplete refocussing		Complete refocussing	
	Siemens	Original	Siemens	Original
GABA-HC	-10%	-70%		-8%
GABA-HA	-32%	-59%		-4%

5.1.2 – Effect of incomplete refocussing in the MEGA-PRESS

It has previously been shown that, in the original pulse sequence, the incomplete refocussing leads to a magnetisation of the system which can be expressed as

$$-0{,}36 \, \hat{I}_{1y} + 0.93 \, 2\hat{I}_{1x}\hat{I}_{2z}$$

The signal (**fig. 44**) is dominated by *anti-phase* magnetisation, and as the signal intensity (subsequently, the GABA concentration) is found by peak integration, the negative contributions will lead to a reduction in the overall SI, which results in the large underrepresentation of GABA concentration in experiments featuring incomplete refocussing.

In the *Siemens*-based pulse sequence the timings are different, and therefore the final state of the system becomes:

$$-0.65\,\hat{I}_{1y} + 0.56\,2\hat{I}_{1x}\hat{I}_{2z}$$

The signal (**fig. 39**) is dominated by *in-phase* magnetisation, and therefore the GABA misrepresentation due to partial refocussing is much lower in the *Siemens*-based version. This explains why the *Siemens*-based experiments with partial refocussing measure the GABA concentration with much greater precision than the original MEGA-PRESS sequence.

5.1.3 – Effect of overlap with creatine

The GABA-H_A resonance overlaps with the Cr–H_C resonance, which made quantification difficult. The spectra had to be both phased and shifted on the ppm axis so that they overlapped perfectly, leaving the smallest achievable remnants of the Cr signal before peak integration. Looking at **fig. 36**, the GABA-H_A calibration curve was systematically lower than the curve based on the GABA-H_c signal for all experiments with partial refocussing. This includes the *"GABA/NAA p1 (Siemens)"* experiment which did not contain Cr. With complete refocussing in experiment *"Full Metabolite Solution (original)*"*, both GABA resonances quantified GABA with similar accuracy. In the *GABA/NAA p2 (original)** (complete refocussing) the GABA-H_A curve fits the theoretical curve better than GABA-H_C. This indicates that Cr signal overlap is not an issue when the edited signal is completely refocussed, but more experiments with complete refocussing (including the *Siemens* sequence) is needed to verify these findings.

5.1.4 – Pitfalls and further work

Most of the calibration curves were constructed using the *Siemens*-based pulse sequence, whereas the two experiments featuring complete refocussing employed the original MEGA-PRESS sequence. Ideally there should have been *Siemens*-based experiments with complete refocussing, too. This would allow for a better comparison of the effect of the degree of refocussing, although it is expected that a completely refocussed *Siemens*-sequence yields similar results to that of the original sequence. Ideally a second parallel for the full metabolite solution experiment should also have been run, but technical difficulties and time constrictions made this impossible. An automated integration method would remove the uncertainty introduced when one chooses the area of integration in *TopSpin*.

Due to hardware- and software problems the shimming (and subsequent water suppression) was not always optimal, leading to somewhat poor SNR in some of the calibration curve experiment. Poor SNR leads to high levels of uncertainty and misquantification at low concentrations of GABA, which affected the results. In light of the methods' goal to be applied *in vivo*, the sequences' robustness is promising. One cannot expect optimal water suppression and shimming *in vivo*, and therefore one needs methods which work at sub-optimal conditions.

5.1.5 – Concluding remarks

Regardless of the refocussing, all calibration curves have good linearity ($R^2 \geq 0.9$). This indicates that both methods may be used to monitor changes to metabolite concentration reliably.

When the refocussing is complete, the GABA concentration is measured by the original MEGA-PRESS with a precision similar to that of the PRESS acquisition. The pulse sequence measures GABA-H_c SI with good precision with incomplete refocussing, but the GABA-H_A SI deviates by over 30% from the theoretical value. This is problematic for *in vivo* measurements as the GABA-H_A resonance is the one that is routinely measured. The original MEGA-PRESS acquisition is not able to measure GABA concentration with good precision when the refocussing is not complete.

It is expected that the *Siemens*-MEGA-PRESS would perform similarly to the original MEGA-PRESS under the same conditions because the differences between the two sequences are negligible when the signal is completely refocussed and the diffusion field gradients are not applied. The *Siemens* MEGA-PRESS performed much better than the original in the experiments featuring partial refocussing. This version is therefore recommended for any experiments where two resonances are to be edited simultaneously.

Some of the early acquisitions of GABA feature an unexpected shape of the GABA-H_A resonance. This may be due to lack of pH in the early experiments, but it is

5.2 – Diffusion measurements

The diffusion data shows that both the *Siemens*-based MEGA-PRESS and the original MEGA-PRESS underrepresent water- and metabolite ADCs. The measured ADCs vary significantly

(**fig. 51**). When normalised with respect to water (**fig. 53**), the variance decreases, indicating systematic variation, which is most likely due to lack of temperature control. Therefore, normalised data must be compared instead of the absolute ADC values. Normalised data are compared against normalised diffusion probe results. No literature values for ADCs in relevant conditions were found. Therefore, the ADCs measured in the diffusion probe experiment may be considered theoretical values as the method is both well-established and very accurate.

5.2.1 – Effect of refocussing

Contrary to what theory predicts, **Fig. 57** indicates that experiments with incomplete refocussing measure the metabolite ADCs better than the experiments with complete refocussing, but this is, again, due to the systematic variance introduced by lack of temperature control. Normalising the measured metabolite ADCs with respect to the water ADC shows that the degree of refocussing has little to no effect on the measured ADC (**fig. 61**). This is expected as the refocussing does not affect the signal attenuation in the Stejskal-Tanner sequence.
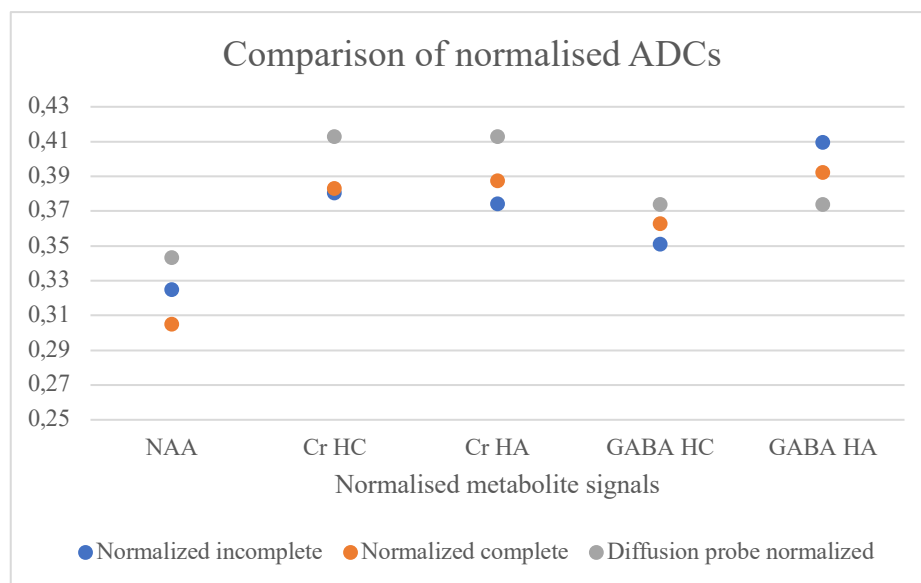
Figure 61 - Comparison of normalised metabolite signals with complete/incomplete refocussing

5.2.2 – Comparison of the two pulse sequences

Normalising the mean ADCs measured by each method and comparing them against normalised diffusion probe results shows that the two methods measure ADCs with about the same precision. The *Siemens*-based pulse sequence misrepresents the ADC of GABA by **-8 %** (GABA-H_C) and **-3 %** (GABA-H_A). The original-based pulse sequence misrepresents the ADC of GABA by **+2 %** and **+11 %**, respectively.
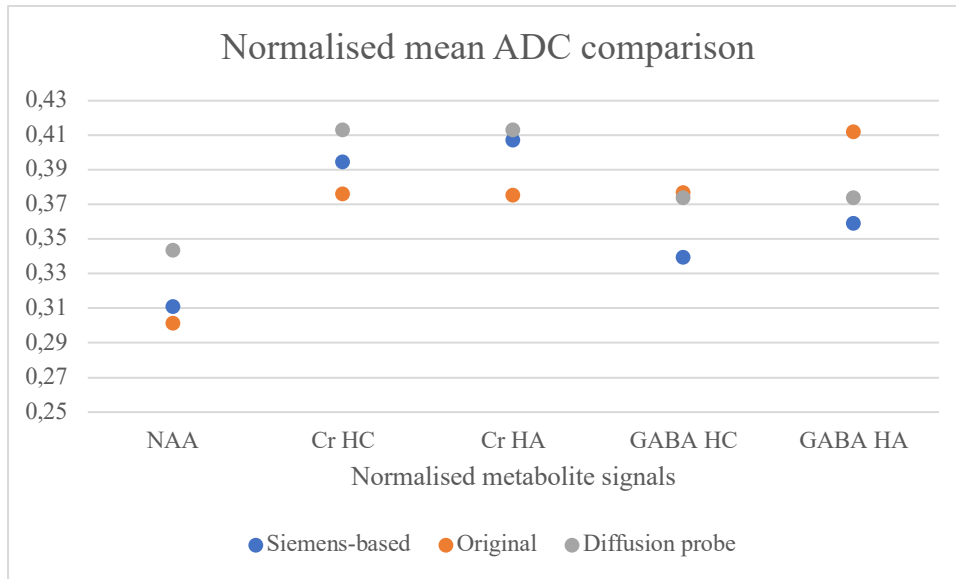
Figure 62 - comparison of normalised ADC values from each of the two pulse sequences

Table 17 - Comparison of normalised GABA ADC measurements of the two MEGA-PRESS sequences

Pulse sequence	Resonance	vs. Diffusion probe (%)
Siemens-based	GABA-HC	-8
	GABA-HA	-3
Original	GABA-HC	+2
	GABA-HA	+11

5.2.3 – Pitfalls and further work

The main pitfall in the diffusion measurement experiments is that there is no control of sample temperature. The diffusion constant of a particle is temperature dependent, and therefore all samples need to be the same temperature in order to directly compare the results. The normalisation of the data shows that temperature uncertainty drives a large part of the variance seen for the measurements, and in further work the samples' temperature ought to be held constant.

Lack of temperature control is not the only reason for the data variance. There are fewer experiments with incomplete refocussing (four in total) than there are experiments with complete refocussing (13 in total). Conducting more experiments with incomplete refocussing would improve the comparison of its effect against that of complete refocussing. When the data shows systematic variance, four experiments is not sufficient to be representative of said variance. Comparing **figs. 55** & **56** demonstrates the difference between available data for each

pulse sequence. If more experiments were performed with lower temperature (due to the lack of temperature control) then it is expected that the variance would become more similar.

The effective MFG strength was not measured, and therefore the *b*-value used in the calculation of metabolite ADCs is not calibrated.

The concentration of GABA differed between the experiments. Lower concentration of GABA equates to lower SNR, which increases the uncertainty of the measured ADC. Ideally, the pulse sequence should be able to handle fluctuations in metabolite concentration as altered metabolite concentrations are often the case in various neural pathologies. Running experiments with constant metabolite concentrations and comparing the results with this thesis' would be a good indication of the pulse sequences' tolerance of metabolite concentration variation.

Another pitfall regards itself with a degree of subjectivity in selecting the chemical shift interval within which one measures signal attenuation. For instance, selecting an interval of (4.65 – 4.75) ppm for the water signal will yield a slightly different result than when an interval of (4.5 – 4.8) is selected. Generally, the chemical shift intervals have been chosen so that there is room for chemical shift displacement between measurements, as the MATLAB code integrates over the entire interval area when measuring SI. However, in some cases such as where Glu is present, there is an overlap with other metabolite signals (in the case of Glu, the NAA singlet at 1.9 ppm). The presence of Glu/NAA singlet overlap may cause errors in subjective chemical shift interval selections, contributing to the overall variance of the dataset. This subjectivity is an inherent weakness of the method and can possibly be eliminated by automated interval selection based on *a priori* knowledge of MOI chemical shifts.

5.2.4 – Concluding remarks

Both the *Siemens*-based MEGA-PRESS and the original MEGA-PRESS underrepresented the ADC of water, NAA, GABA and Cr. The lack of temperature control introduced a systematic variance in the data which prohibits a direct comparison of the measured ADCs. However, when the metabolite ADCs are normalised with respect to the water signal in each experiment, the precision of GABA-ADC measurements is close to that of the diffusion probe. This is promising for the method's future application *in vivo*, but future *in vitro* experiments with adequate temperature control is needed for a direct comparison of the two methods' precision.

It is expected that other *in vivo* experimental challenges such as patient movement during ON/OFF acquisitions, macromolecule signal overlap, cranium magnetic susceptibility and coil-patient-distance will have a larger impact on the uncertainty of ADC measurements rather than the uncertainty relating to the pulse sequence itself.

Bibliography

1.	Purcell, E. M., Torrey, H. C. & Pound, R. V. Resonance absorption by nuclear magnetic moments in a solid [7]. *Physical Review* vol. 69 37–38 (1946).

2.	Bloch, F., Hansen, W. W. & Packard, M. The nuclear induction experiment. *Phys. Rev.* **70**, 474–485 (1946).

3.	Ramin, S. L., Tohnola, W. A. & Spotti, A. R. Proton magnetic resonance spectroscopy: Clinical applications in patients with brain lesions. *Sao Paulo Med. J.* **121**, 254–259 (2003).

4.	Frahm, J. *et al.* Localized proton NMR spectroscopy in different regions of the human brain in vivo. Relaxation times and concentrations of cerebral metabolites. *Magn. Reson. Med.* **11**, 47–63 (1989).

5.	Kwock, L. *et al.* Clinical applications of proton MR spectroscopy in oncology. *Technology in Cancer Research and Treatment* vol. 1 17–28 (2002).

6.	Fayed, N., Modrego, P. J., Rojas-Salinas, G. & Aguilar, K. Brain glutamate levels are decreased in alzheimer's disease: A magnetic resonance spectroscopy study. *Am. J. Alzheimers. Dis. Other Demen.* **26**, 450–456 (2011).

7.	Steen, R. G., Hamer, R. M. & Lieberman, J. A. Measurement of brain metabolites by 1H magnetic resonance spectroscopy in patients with schizophrenia: A systematic review and meta-analysis. *Neuropsychopharmacology* vol. 30 1949–1962 (2005).

8.	Fjermestad, I. Spectral editing of brain metabolites using weighted Nuclear Magnetic Resonance. (University of Bergen, 2019).

9.	Wishart, D. S. *et al.* HMDB 4.0: The human metabolome database for 2018. *Nucleic Acids Res.* **46**, D608–D617 (2018).

10.	ChemDraw – Chemical Communications Software | PerkinElmer. https://www.perkinelmer.com/no/category/chemdraw.

11.	Govindaraju, V., Young, K. & Maudsley, A. A. Proton NMR chemical shifts and coupling constants for brain metabolites. *NMR Biomed.* **13**, 129–153 (2000).

12. Tiwari, P., Dwivedi, S., Singh, M. P., Mishra, R. & Chandy, A. Basic and modern concepts on cholinergic receptor: A review. *Asian Pacific J. Trop. Dis.* **3**, 413–420 (2013).

13. Eglen, R. M. Muscarinic receptor subtypes in neuronal and non-neuronal cholinergic function. *Autonomic and Autacoid Pharmacology* vol. 26 219–233 (2006).

14. Blüml, S., Seymour, K. J. & Ross, B. D. Developmental changes in choline- and ethanolamine-containing compounds measured with proton-decoupled 31P MRS in in vivo human brain. *Magn. Reson. Med.* **42**, 643–654 (1999).

15. Lange, T. *et al.* Pitfalls in lactate measurements at 3T. *Am. J. Neuroradiol.* **27**, 895–901 (2006).

16. Inventor, S., Bottomley, P. A. & Park, C. *United States Patent (19) Bottomley (54) (75) (73) (21) 22) (51) (52) (58) 56) SELECTIVE VOLUMEMETHOD FOR PERFORMING LOCALZED NMR.* (1982).

17. Moonen, C. T. W. *et al.* Comparison of single-shot localization methods (steam and press) for In vivo proton NMR spectroscopy. *NMR Biomed.* **2**, 201–208 (1989).

18. Mescher, M., Merkle, H., Kirsch, J., Garwood, M. & Gruetter, R. Simultaneous in vivo spectral editing and water suppression. (1998).

19. Deelchand, D. K., Auerbach, E. J. & Marjańska, M. Apparent diffusion coefficients of the five major metabolites measured in the human brain in vivo at 3T. *Magn. Reson. Med.* **79**, 2896–2901 (2018).

20. Valette, J., Ligneul, C., Marchadour, C., Najac, C. & Palombo, M. Brain metabolite diffusion from ultra-short to ultra-long time scales: What do we learn, where should we go? *Front. Neurosci.* **12**, (2018).

21. Palombo, M., Shemesh, N., Ronen, I. & Valette, J. Insights into brain microstructure from in vivo DW-MRS. *Neuroimage* **182**, 97–116 (2018).

22. Ronen, I. & Valette, J. Diffusion-Weighted Magnetic Resonance Spectroscopy. in *eMagRes* vol. 4 733–750 (John Wiley & Sons, Ltd, 2015).

23. Landheer, K. *et al.* Diffusion-weighted J-resolved spectroscopy. *Magn. Reson. Med.* **78**, 1235–1245 (2017).

24. Friebolin, H. Basic one- and two-dimensional NMR spectroscopy. (2011).

25. Keeler, J. Understanding NMR Spectroscopy, 2nd Edition | Wiley. *Wiley* 190–200 (2010).

26. Sørgård, H. N. Wetting in Porous Media : A Nuclear Magnetic Resonance Wetting in Porous Media : A Nuclear Magnetic Resonance Study . (University of Bergen, 2020).

27. Pascal's Triangle - Chemistry LibreTexts. https://chem.libretexts.org/Bookshelves/Physical_and_Theoretical_Chemistry_Textbook_Maps/Supplemental_Modules_(Physical_and_Theoretical_Chemistry)/Spectroscopy/Magnetic_Resonance_Spectroscopies/Nuclear_Magnetic_Resonance/NMR%3A_Experimental/NMR_-_Interpre.

28. Help on 1H NMR. http://www.che.hw.ac.uk/teaching/cheak2/B18OA1/Webtest/1HNMR-Help.html.

29. University of Ottawa NMR Facility Blog: Excitation Profiles for Shaped Pulses. http://u-of-o-nmr-facility.blogspot.com/2011/01/excitation-profiles-for-shaped-pulses.html.

30. Nilsson, M. Introduction to diffusion NMR. (2018).

31. Near, J., Evans, C. J., Puts, N. A., Barker, P. B. & Edden, R. A. J-difference editing of GABA: simulated and experimental multiplet patterns. *Magn. Reson. Med.* **70**, 1183–1191 (2013).

32. Stagg, C. J. & Rothman, D. L. Magnetic Resonance Spectroscopy: Tools for Neuroscience Research and Emerging Clinical Applications. *Magn. Reson. Spectrosc. Tools Neurosci. Res. Emerg. Clin. Appl.* 1–359 (2013) doi:10.1016/C2011-0-09647-3.

33. Harris, A. D., Saleh, M. G. & Edden, R. A. E. Edited 1H magnetic resonance spectroscopy in vivo: Methods and metabolites. *Magn. Reson. Med.* **77**, 1377–1389 (2017).

34. Bjørnerud, A. The Physics of Magnetic Resonance Imaging FYS-KJM 4740. (2008).

35. Stejskal, E. O. & Tanner, J. E. Spin Diffusion Measurements: Spin Echoes in the Presence of a Time-Dependent Field Gradient. *J. Chem. Phys.* **42**, 288 (2004).

36. ParaVision 360 User Manual Innovation with Integrity • PCI.

37. Haase, A., Frahm, J., Matthaei, D., Hänicke, W. & Merboldt, K. D. FLASH imaging: Rapid NMR imaging using low flip-angle pulses. *J. Magn. Reson.* **213**, 533–541 (2011).

38. Haase, A., Frahm, J., Hanicke, W. & Matthaei, D. 'H NMR chemical shift selective (CHESS) imaging? *Phys. Med. Biol* **30**, 341–344 (1985).

39. Harris, A. D. *et al.* Normalizing data from GABA-edited MEGA-PRESS implementations at 3 Tesla. *Magn. Reson. Imaging* **42**, 8–15 (2017).

Appendix A – Calibration curve experimental data

Experiment 1 - GABA/NAA p1

PRESS-acquisition

Solution	Metabolite	c, mM	Peak	Theoretical SI	SI	Diff %
A	NAA	12,57	H$_A$	1,0000	1,0000	0,00
	GABA	0,00	H$_C$	None	None	None
		0,00	H$_A$	None	None	None
B	NAA	12,57	H$_A$	1,0000	1,0000	0,00
	GABA	2,06	H$_C$	0,1091	0,1055	-3,30
		2,06	H$_A$	0,1091	0,1091	0,00
C	NAA	12,57	H$_A$	1,0000	1,0000	0,00
	GABA	4,38	H$_C$	0,2326	0,2010	-13,57
		4,38	H$_A$	0,2326	0,1923	-17,31
D	NAA	12,57	H$_A$	1,0000	1,0000	0,00
	GABA	6,40	H$_C$	0,3396	0,2944	-13,30
		6,40	H$_A$	0,3396	0,2915	-14,16
E	NAA	12,57	H$_A$	1,0000	1,0000	0,00
	GABA	7,87	H$_C$	0,4178	0,3857	-7,68
		7,87	H$_A$	0,4178	0,3829	-8,35
F	NAA	12,57	H$_A$	1,0000	1,0000	0,00
	GABA	10,09	H$_C$	0,5351	0,4719	-11,81
		10,09	H$_A$	0,5351	0,4728	-11,64

MEGA-PRESS acquisition

Solution	Metabolite	c, mM	Peak	Theoretical SI	SI	Diff %
A	NAA	12,57	H_A	1,0000	1,0000	0,00
	GABA	0,00	H_C	None	None	None
			H_A	None	None	None
B	NAA	12,57	H_A	1,0000	1,0000	1,00
	GABA	2,06	H_C	0,1091	0,1385	26,97
			H_A	0,1091	0,0863	-20,90
C	NAA	12,57	H_A	1,0000	1,0000	0,00
	GABA	4,38	H_C	0,2326	0,2413	3,76
			H_A	0,2326	0,1683	-27,63
D	NAA	12,57	H_A	1,0000	1,0000	0,00
	GABA	6,40	H_C	0,3396	0,3340	-1,64
			H_A	0,3396	0,2339	-31,12
E	NAA	12,57	H_A	1,0000	1,0000	0,00
	GABA	7,87	H_C	0,4178	0,4276	2,35
			H_A	0,4178	0,3175	-24,00
F	NAA	12,57	H_A	1,0000	1,0000	0,00
	GABA	10,09	H_C	0,5351	0,4946	-7,57
			H_A	0,5351	0,3813	-28,74

Experiment 2 – GABA/NAA p2

[NAA] = 13,01 mM

Solution	Metabolite	c (mM)	Peak	Theoretical SI	Incomplete Refocusing		Complete refocusing	
					SI	Diff %	SI	Diff %
B	GABA	2,29	HC	0,1173	0,0477	-59,3	0,1112	-5,2
			HA	0,1173	0,0639	-45,5	0,1258	7,2
C	GABA	3,96	HC	0,2027	0,0581	-71,3	0,1707	-15,8
			HA	0,2027	0,0815	-59,8	0,1891	-6,7
D	GABA	5,86	HC	0,3001	0,0876	-70,8	0,2513	-16,3
			HA	0,3001	0,1209	-59,7	0,2820	-6,0
E	GABA	8,15	HC	0,4174	0,1204	-71,2	0,3376	-19,1
			HA	0,4174	0,1426	-65,8	0,3842	-8,0
F	GABA	9,97	HC	0,5108	0,1262	-75,3	0,4318	-15,5
			HA	0,5108	0,1811	-64,5	0,4758	-6,9
Avg	GABA		HC			**-69,6**		**-14,4**
			HA			**-59,1**		**-4,1**

Experiment 3 – GABA/NAA/Cr p1

PRESS

Solution	Metabolite	Peak	Theoretical SI	SI	Diff %
A	NAA	H_A	1,0000	1,0000	0,00
	GABA	H_C	None	None	None
	Cr	H_A	0,5449	0,5598	2,73
B	NAA	H_A	1,0000	1,0000	0,00
	GABA	H_C	0,1087	0,1006	-7,45
	Cr	H_A	0,5449	0,5746	5,45
C	NAA	H_A	1,0000	1,0000	0,00
	GABA	H_C	0,2278	0,1982	-12,99
	Cr	H_A	0,5449	0,5731	5,17
D	NAA	H_A	1,0000	1,0000	0,00
	GABA	H_C	0,3364	0,3085	-8,29
	Cr	H_A	0,5449	0,5843	7,23
E	NAA	H_A	1,0000	1,0000	0,00
	GABA	H_C	0,4848	0,4328	-10,73
	Cr	H_A	0,5449	0,5680	4,23
F	NAA	H_A	1,0000	1,0000	0,00
	GABA	H_C	0,5809	0,5075	-12,64
	Cr	H_A	0,5449	0,6008	10,25

MEGA-PRESS

[NAA] = 19,98 mM

Solution	Metabolite	c (mM)	Peak	Theoretical SI	SI	Diff %
B	GABA	2,60	H_C	0,0867	0,0142	-83,63
			H_A	0,0867	0,0364	-58,03
	Cr	10,17	H_A	0,3333	0,3518	5,54
C	GABA	4,42	H_C	0,1476	0,0981	-33,52
			H_A	0,1476	0,0799	-45,85
	Cr	10,17	H_A	0,3333	0,3335	0,05
D	GABA	5,74	H_C	0,1916	0,1400	-27,12
			H_A	0,1916	0,1500	-23,00
	Cr	10,17	H_A	0,3333	0,3461	3,83

E	GABA	8,81	H_C	0,2938	0,2125	-27,67
			H_A	0,2938	0,1307	-55,52
	Cr	10,17	H_A	0,3333	0,3799	13,97
F	GABA	10,86	H_C	0,3600	0,2800	-24,01
			H_A	0,3600	0,1900	-47,63
	Cr	10,17	H_A	0,3333	0,3607	8,21
Avg.	GABA		H_C			**-39,19**
			H_A			**-46,01**
	Cr		H_A			**6,32**

GABA/NAA/Cr p2 *Siemens* calibration curve

Theoretical
$y = 0,0341x - 0,0072$
$R^2 = 0,9968$

Linear HA
$y = 0,017x + 0,0057$
$R^2 = 0,8918$

Linear HC
$y = 0,0269x - 0,0219$
$R^2 = 0,9711$

GABA concentration in mmol/L

- GABA HC
- GABA HA
- Theoretical SI
- Lineær (GABA HC)
- Lineær (GABA HA)
- Lineær (Theoretical SI)
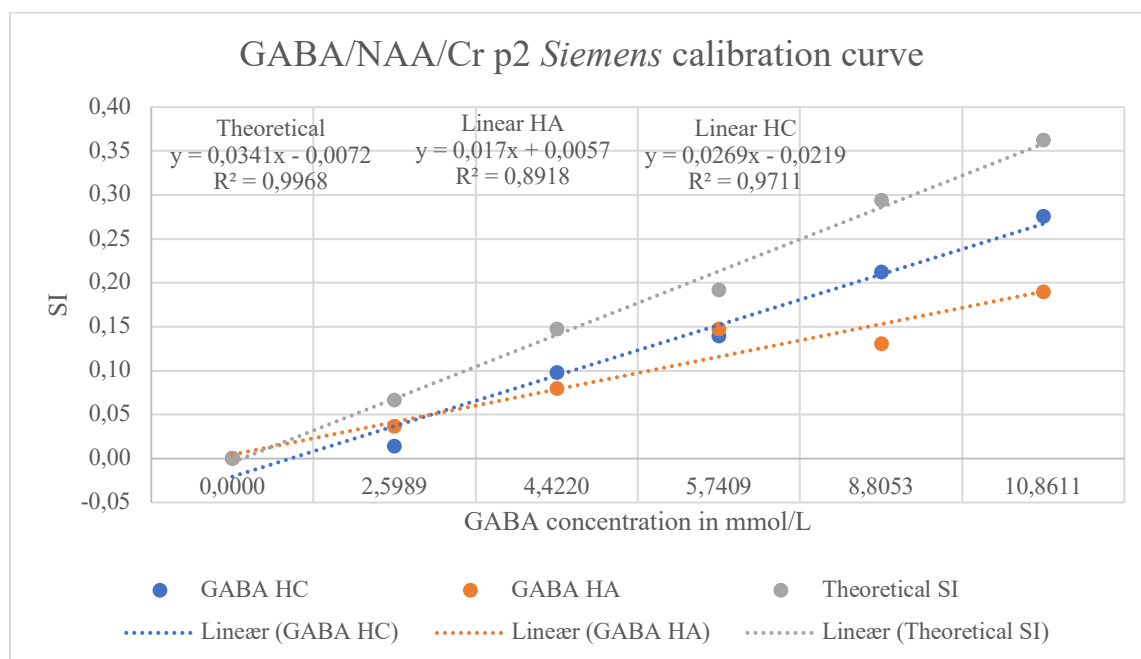
Experiment 4 – GABA/NAA/Cr p2

[NAA] = 12,38 mM

Solution	Metabolite	c (mM)	Peak	Theoretical SI	SI	Diff %
B	GABA	2,02	H_C	0,1087	0,1270	16,84
			H_A	0,1087	0,0820	-24,56
	Cr	10,12	H_A	0,5449	0,5566	2,14
C	GABA	4,23	H_C	0,2278	0,2488	9,22
			H_A	0,2278	0,1936	-15,01
	Cr	10,12	H_A	0,5449	0,5627	3,26
D	GABA	6,25	H_C	0,3364	0,3187	-5,26
			H_A	0,3364	0,2371	-29,52

	Cr	10,12	H_A	0,5449	0,5885	8,00
E	GABA	9,00	H_C	0,4848	0,5092	5,03
			H_A	0,4848	0,3796	-21,70
	Cr	10,12	H_A	0,5449	0,5747	5,46
F	GABA	10,78	H_C	0,5809	0,5660	-2,56
			H_A	0,5809	0,4274	-26,42
	Cr	10,12	H_A	0,5449	0,5989	9,90
Avg.	GABA		H_C			**4,65**
			H_A			**-23,44**
	Cr	10,12	H_A			**5,75**

GABA (NAA&Cr) p1 *Siemens* Calibration Curve, PRESS

Linear (Theoretical)
y = 0,1183x - 0,1244
R² = 0,9978

Linear (HC)
y = 0,0474x + 0,003
R² = 0,999

GABA (NAA&Cr) p1 *Siemens* Cal. Curve, MEGA-PRESS

Linear (Theoretical)
y = 0,1183x - 0,1244
R² = 0,9978

Linear GABA (HA)
y = 0,0878x - 0,0874
R² = 0,9855

Linear GABA (HC)
y = 0,1156x - 0,1097
R² = 0,9859
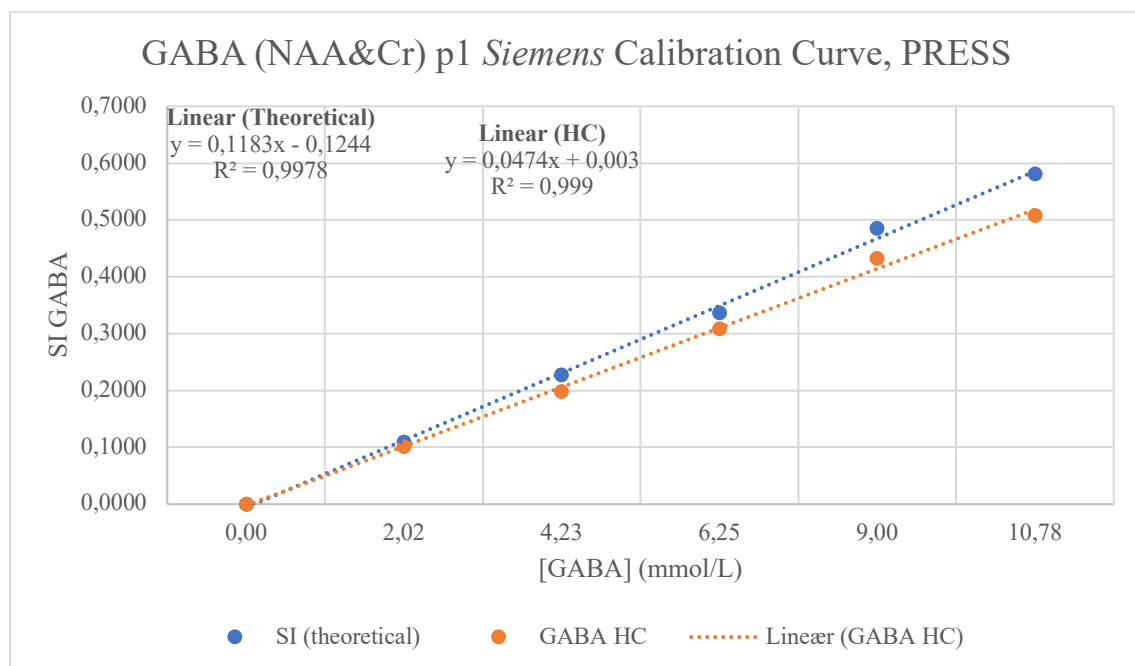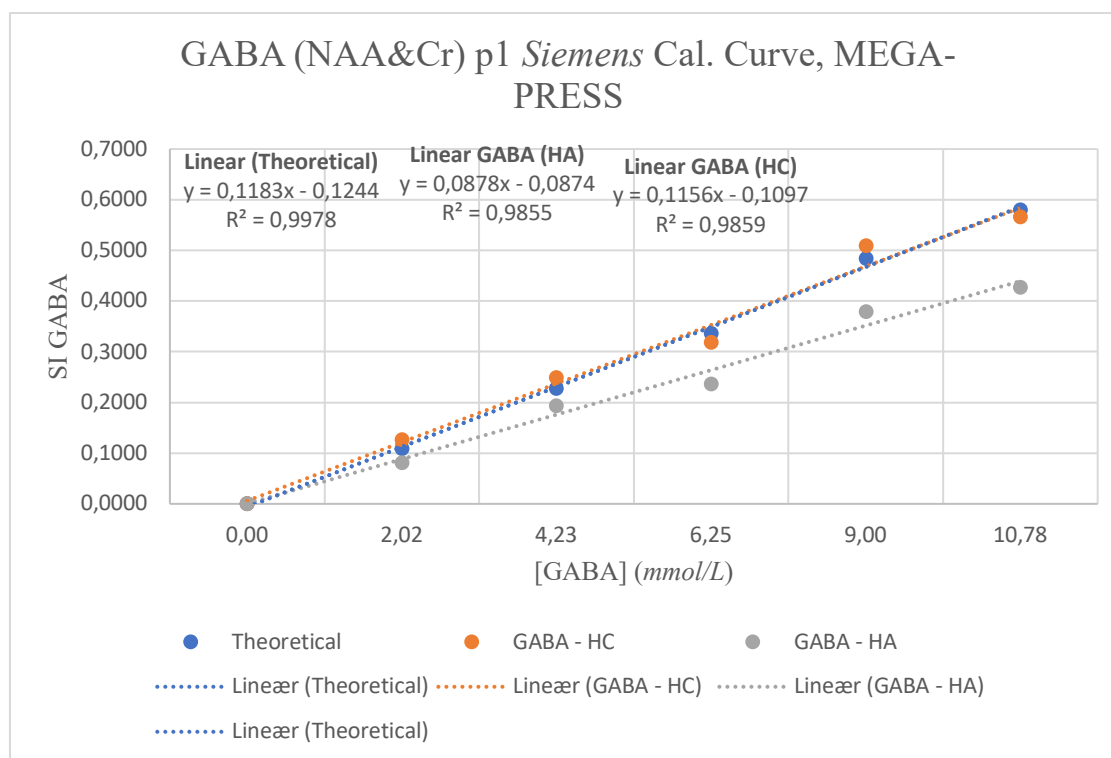
Experiment 5 – Full metabolite solution

Metabolite	c (mM)
Cr	10,24
Cho	3,05
NAA	12,63
mIns	0,76
Glu	12,50
Lac	5,20

Solution	Metabolite	c (mM)	Peak	Theoretical SI	SI	Diff %
B	GABA	2,480	HC	0,1311	0,1878	43,2
			HA	0,1311	0,1375	4,9
C	GABA	4,150	HC	0,2191	0,2356	7,5
			HA	0,2191	0,1941	-11,4
D	GABA	5,860	HC	0,3093	0,3163	2,3
			HA	0,3093	0,2781	-10,1
E	GABA	7,870	HC	0,4158	0,3936	-5,3
			HA	0,4158	0,3624	-12,8
F	GABA	10,320	HC	0,5448	0,4909	-9,9
			HA	0,5448	0,4710	-13,5
Avg	GABA		HC			**7,6**
			HA			**-8,6**

Appendix B – Diffusion measurements experimental data

Experiment 6 – GABA/NAA/Cr/Glu Sp1

Metabolite	Molarity (mmol/L)
NAA	12,61
GABA	5,39
Cr	10,41
Glu	13,06

Signal	Interval (ppm)	ADC	SE	R2	Adj. R2	Outliers removed
Water	(4.5-4.9)	2,0269E-09	5,5316E-11	0,993	0,993	
NAA	(1.89-1.99)	6,4359E-10	3,3424E-11	0,976	0,974	
Cr	(2.85-3.05)	7,7719E-10	2,5289E-11	0,991	0,990	
Cr	(3.76-3.96)	7,5336E-10	3,3556E-11	0,982	0,981	
Glu	(3.6-3.75)	7,4440E-10	6,0497E-11	0,956	0,949	7, 9
GABA	(2.2-2.5)	7,1509E-10	3,0525E-11	0,987	0,986	1, 7
GABA	(2.85-3.05)	6,7072E-10	1,1070E-10	0,860	0,836	3, 5, 9
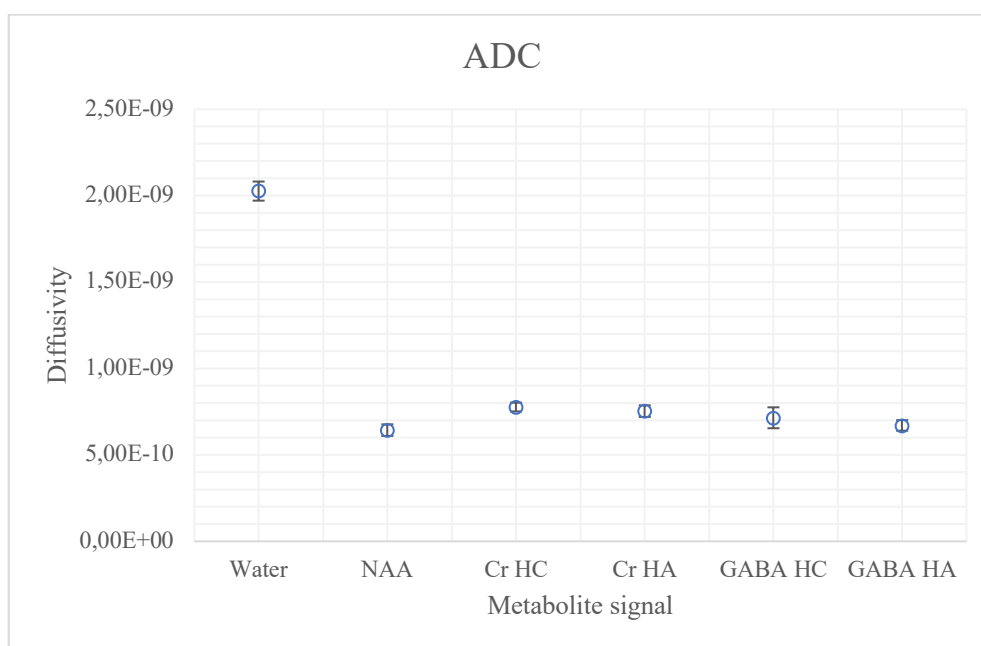
Experiment 7 – GABA Sp1

Metabolite	Molarity (mmol/L)
GABA	6,52

Signal	Interval (ppm)	ADC	SE	R2	Adj. R2	Outliers removed
Water	(4.5-4.9)	1,9012E-09	4,5772E-11	0,995	0,994	
GABA	(2.1-2.35)	6,7487E-10	8,6792E-11	0,896	0,881	6, 9
GABA	(2.8-3.0)	1,2336E-09	1,5004E-10	0,894	0,881	3
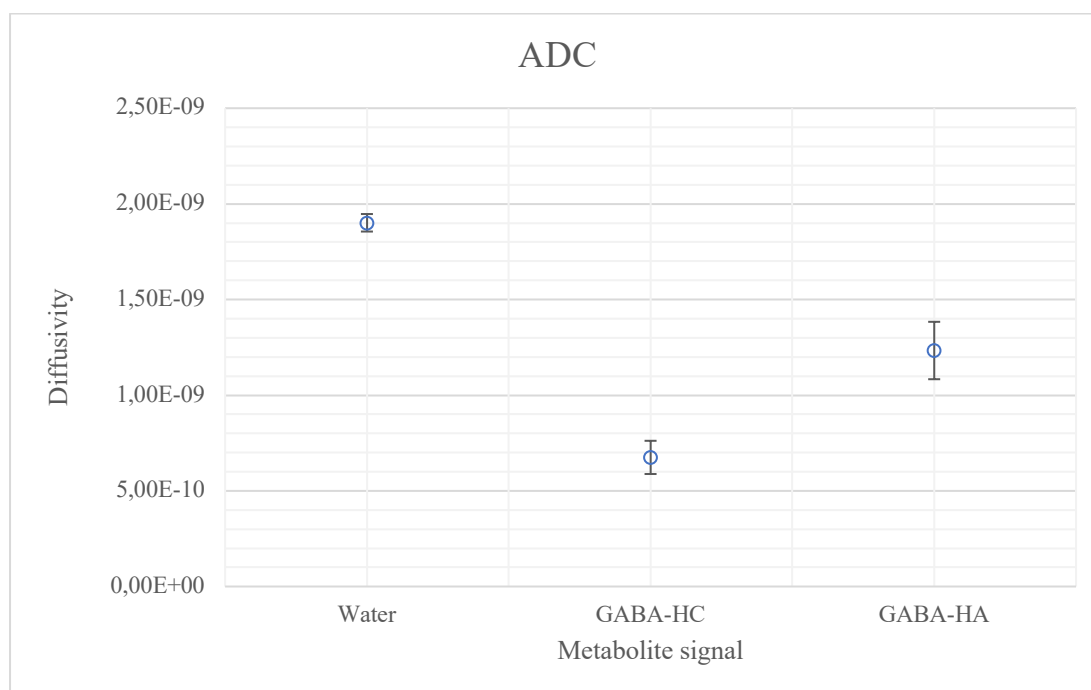
Experiment 8 – GABA/NAA Sp1

Metabolite	Molarity (mmol/L)
GABA	6,17
NAA	12,77

Signal	Interval (ppm)	ADC	SE	R2	Adj. R2	Outliers removed
Water	(4.6-4.8)	2,0589E-09	4,6528E-11	0,995	0,995	
NAA	(1.85-1.95)	6,5579E-10	1,9385E-11	0,992	0,991	
GABA	(2.1-2.35)	5,5430E-10	1,0153E-10	0,788	0,762	7
GABA	(2.8-3.0)	8,0011E-10	9,3519E-10	0,891	0,878	
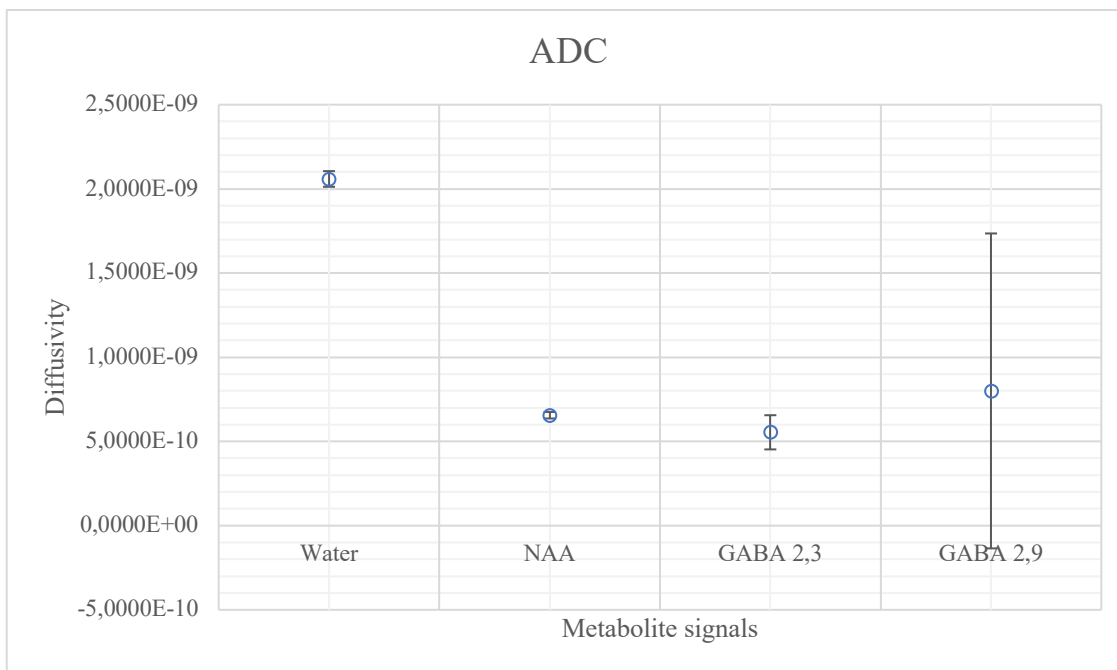
Experiment 9 – GABA/NAA/Cr Sp1

Metabolite	Molarity (mmol/L)
GABA	6,21
NAA	13,86
Cr	10,30

Signal	Interval (ppm)	ADC	SE	R2	Adj. R2	Outliers removed
Water	(4.6-4.8)	2,0110E-09	4,0404E-11	0,996	0,996	
NAA	(1.85-1.95)	6,4991E-10	2,5670E-11	0,986	0,985	
Cr HC	(2.85-3.00)	7,4441E-10	1,8332E-11	0,995	0,994	
Cr HA	(3.7-3.9)	7,4418E-10	2,8164E-11	0,987	0,986	
GABA HC	(2.1-2.2)	8,3635E-10	5,5624E-11	0,970	0,966	3, 6
GABA HA	(2.8-2,95)	9,8646E-10	1,7534E-10	0,819	0,793	7, 8
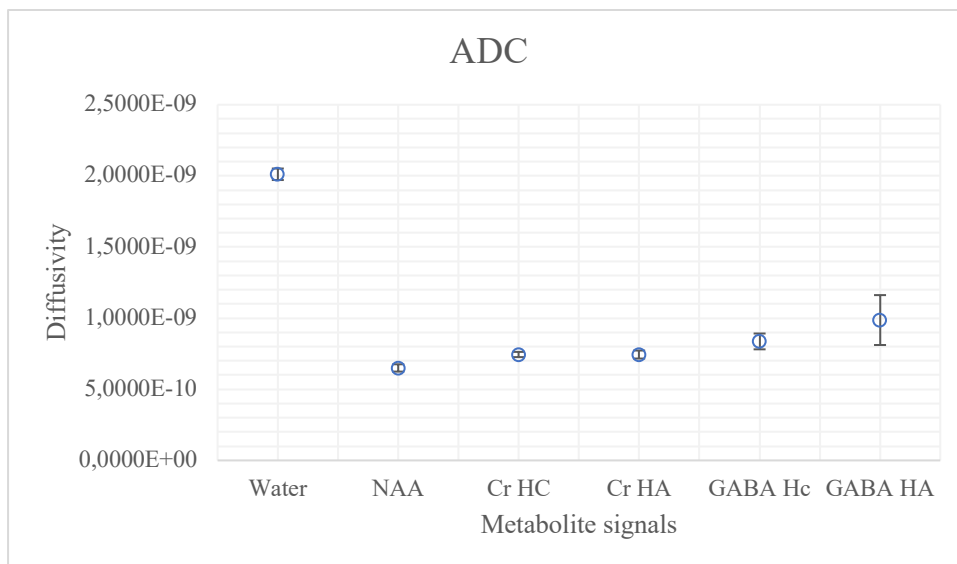
Experiment 10 – GABA/NAA Op1

Metabolite	Molarity (mmol/L)
GABA	7,95
NAA	13,06

Signal	Interval (ppm)	ADC	SE	R2	Adj. R2	Outliers removed
Water	(4,65-4,75)	1,8299E-09	9,1409E-11	0,990	0,988	None
NAA	(1.85-1.95)	5,0438E-10	6,2745E-12	0,999	0,999	None
GABA Hc	(2.1-2.25)	6,3031E-10	2,3575E-11	0,994	0,993	None
GABA Ha	(2.85-2.95)	6,4647E-10	1,7020E-11	0,997	0,997	None
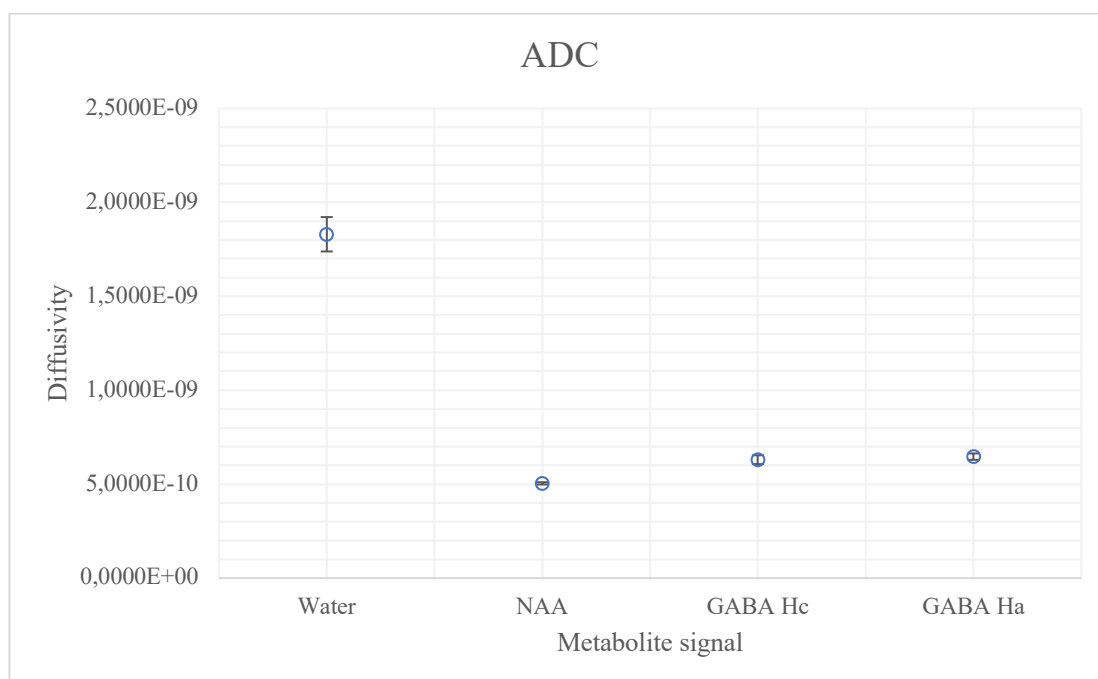
Experiment 11 – GABA/NAA/Cr Sp2

Metabolite	Molarity (mmol/L)
NAA	12,20
Cr	9,71
GABA	9,43

Signal	Interval (ppm)	ADC	SE	R2	Adj. R2	Outliers removed
Water	(4,65-4,75)	1,5182E-09	3,5945E-11	0,996	0,995	1
NAA	(1.85-1.95)	5,2363E-10	9,3708E-11	0,997	0,997	None
GABA Hc	(2.1-2.25)	6,0972E-10	2,0086E-11	0,996	0,989	None
GABA Ha	(2.85-2.95)	5,9926E-10	5,3800E-11	0,931	0,923	None
Cr Ha	(3.75-3.85)	6,2738E-10	1,8769E-11	0,992	0,991	None
Cr Hb	(2.85-2.95)	6,4096E-10	8,5640E-12	0,998	0,998	None
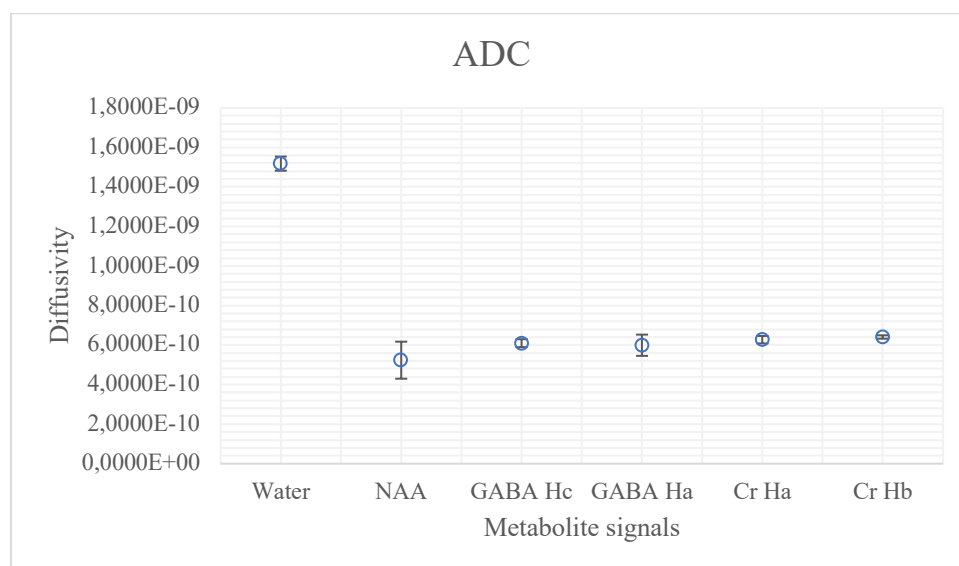
Experiment 12 – GABA/NAA/Cr Sp3

Signal	Interval (ppm)	ADC	SE	R2	Adj. R2	Outliers removed
Water	(4,65-4,75)	1,5300E-09	2,7854E-11	0,997	0,997	None
NAA	(1.85-1.95)	5,2730E-10	7,3995E-11	0,998	0,998	None
GABA Hc	(2.1-2.25)	5,7086E-10	3,0591E-11	0,975	0,972	None
GABA Ha	(2.85-2.95)	6,5436E-10	3,2426E-11	0,978	0,976	None
Cr Ha	(3.75-3.85)	6,5665E-10	2,0675E-11	0,991	0,990	None
Cr Hb	(2.85-2.95)	6,1478E-10	9,2322E-12	0,998	0,998	None

ADC
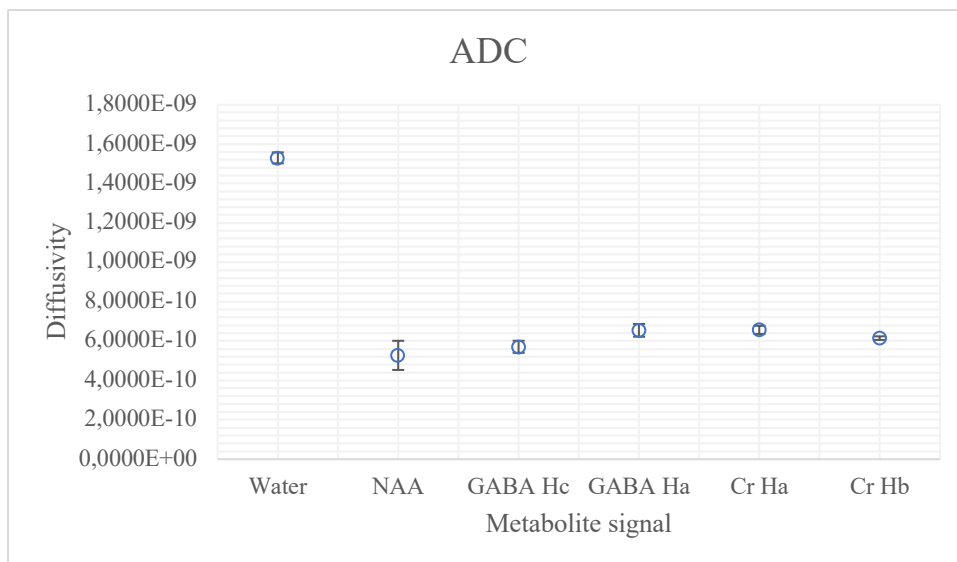
Experiment 13 – GABA/NAA/Cr Op1

Signal	Interval (ppm)	ADC	SE	R2	Adj. R2	Outliers removed
Water	(4,65-4,75)	1,7596E-09	2,1124E-11	0,999	0,999	None
NAA	(1.85-1.95)	5,1977E-10	6,6941E-12	0,999	0,999	None
GABA Hc	(2.1-2.25)	6,4956E-10	1,7018E-11	0,997	0,997	None
GABA Ha	(2.85-2.95)	5,6039E-10	2,0371E-11	0,996	0,996	6
Cr Ha	(3.75-3.85)	6,5670E-10	9,8739E-12	0,999	0,999	None
Cr Hb	(2.85-2.95)	6,5967E-10	1,0282E-11	0,999	0,999	None

ADC
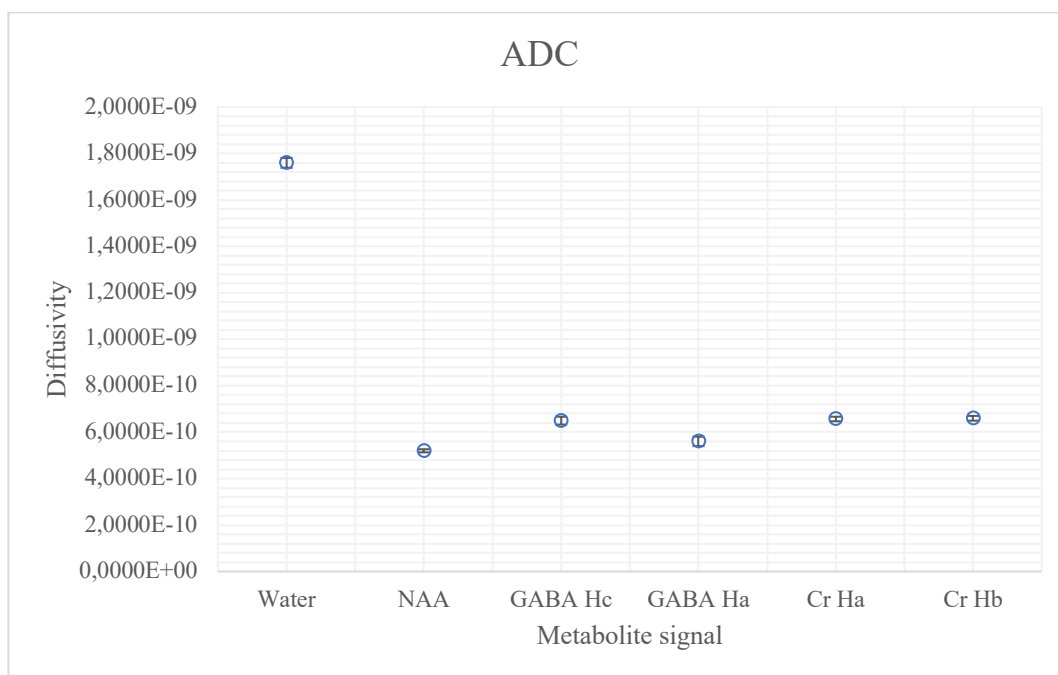
Experiment 14 – GABA/NAA/Cr Op2

Signal	Interval (ppm)	ADC	SE	R2	Adj. R2	Outliers removed
Water	(4,65-4,75)	1,7893E-09	2,3017E-11	1,000	0,999	6
NAA	(1.85-1.95)	5,2793E-10	7,8789E-12	0,999	0,999	None
GABA Hc	(2.1-2.25)	6,4114E-10	1,2082E-11	0,999	0,999	None
GABA Ha	(2.85-2.95)	6,8593E-10	1,3073E-11	0,999	0,998	None
Cr Ha	(3.75-3.85)	6,3489E-10	4,8591E-12	1,000	1,000	None
Cr Hb	(2.85-2.95)	6,6299E-10	1,2603E-11	0,999	0,998	None
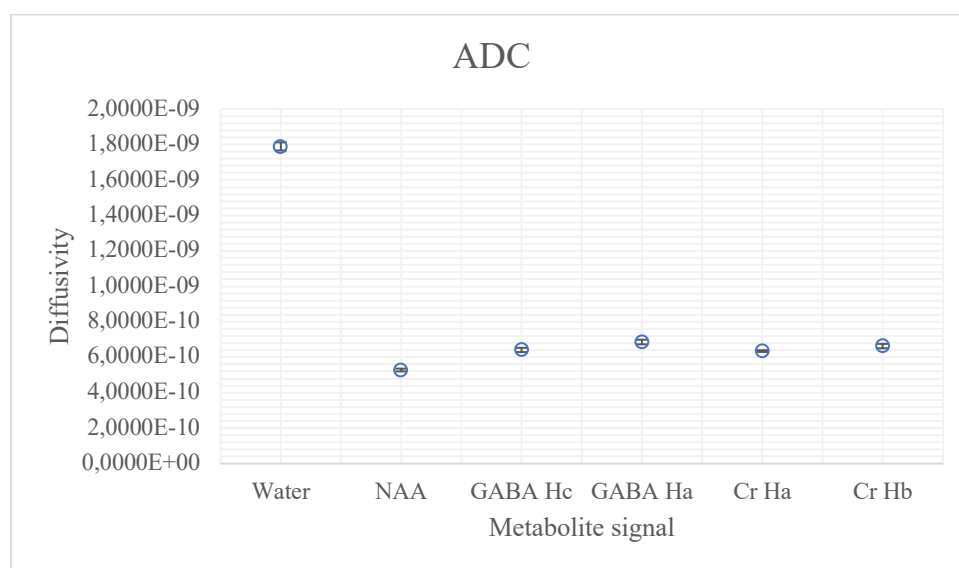
Experiment 15 – Full metabolite solution Op1

Metabolite	Molarity (mmol/L)
NAA	12,20
Cr	9,71
GABA	9,43

Signal	Interval (ppm)	ADC	SE	R2	Adj. R2	Outliers removed
Water	(4,65-4,75)	1,8455E-09	2,9070E-11	1,000	0,999	1, 6
NAA	(1.85-1.95)	5,1774E-10	6,6234E-12	0,999	0,999	None
GABA Hc	(2.1-2.25)	6,9216E-10	3,8140E-11	0,988	0,985	None
GABA Ha	(2.85-2.95)	8,3960E-10	3,0573E-11	0,995	0,993	None
Cr Ha	(3.75-3.85)	6,3295E-10	1,3248E-11	0,999	0,998	6
Cr Hb	(2.85-2.95)	6,4413E-10	6,5731E-12	1,000	0,999	None
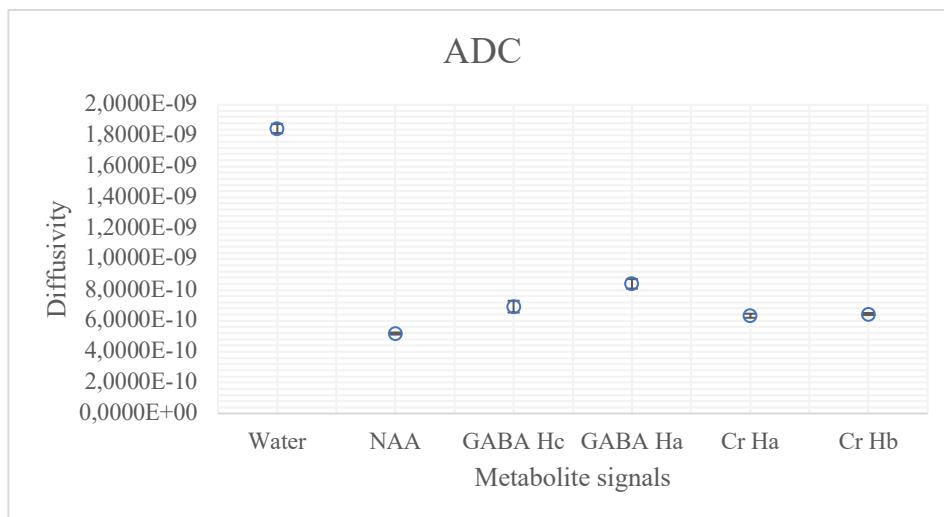
Experiment 16 – Full metabolite solution Op2

Signal	Interval (ppm)	ADC	SE	R2	Adj. R2	Outliers removed
Water	(4,65-4,75)	1,8545E-09	6,9789E-11	0,994	0,993	None
NAA	(1.85-1.95)	5,0484E-10	6,8097E-12	0,999	0,999	None
GABA Hc	(2.1-2.25)	7,3134E-10	4,1053E-11	0,988	0,984	None
GABA Ha	(2.85-2.95)	9,1737E-10	1,1699E-10	0,939	0,924	None
Cr Ha	(3.75-3.85)	6,2555E-10	5,9819E-12	1,000	1,000	None
Cr Hb	(2.85-2.95)	6,4424E-10	5,2712E-12	1,000	1,000	None
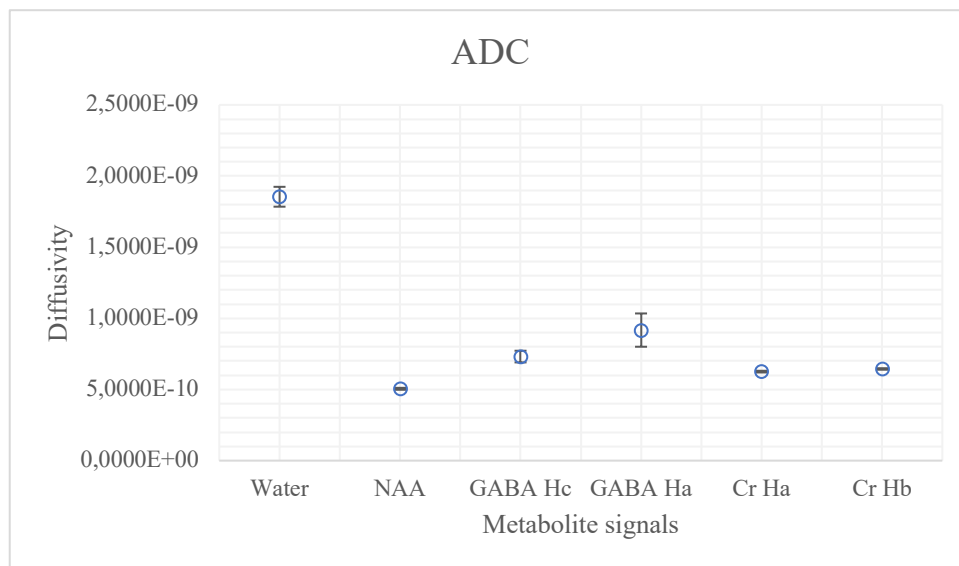
Experiment 17 – Full metabolite solution Sp1

Signal	Interval (ppm)	ADC	SE	R2	Adj. R2	Outliers removed
Water	(4,65-4,75)	1,6353E-09	1,8136E-11	0,999	0,999	None
NAA	(1.85-1.95)	4,9819E-10	1,3962E-11	0,993	0,992	None
GABA Hc	(2.1-2.25)	4,7840E-10	4,9976E-11	0,920	0,910	5
GABA Ha	(2.85-2.95)	5,2857E-10	6,1826E-11	0,924	0,911	5, 8, 9
Cr Ha	(3.75-3.85)	7,2095E-10	2,4920E-11	0,989	0,988	None
Cr Hb	(2.85-2.95)	6,7374E-10	2,4668E-11	0,988	0,987	None
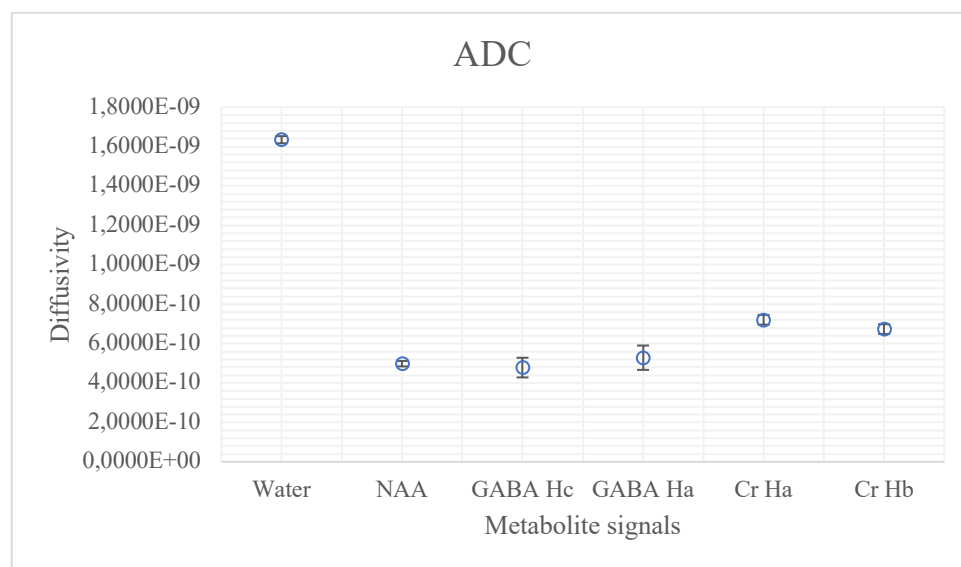
Experiment 18 – Full metabolite Sp2

Signal	Interval (ppm)	ADC	SE	R2	Adj. R2	Outliers removed
Water	(4,65-4,75)	1,6390E-09	1,5549E-11	0,999	0,999	None
NAA	(1.85-1.95)	4,8230E-10	1,7547E-10	0,988	0,987	None
GABA Hc	(2.1-2.25)	4,8006E-10	5,8694E-11	0,893	0,880	1
GABA Ha	(2.85-2.95)	4,9911E-10	9,8449E-11	0,763	0,733	1
Cr Ha	(3.75-3.85)	6,5201E-10	2,5732E-11	0,986	0,985	None
Cr Hb	(2.85-2.95)	6,4500E-10	1,6743E-11	0,994	0,993	None
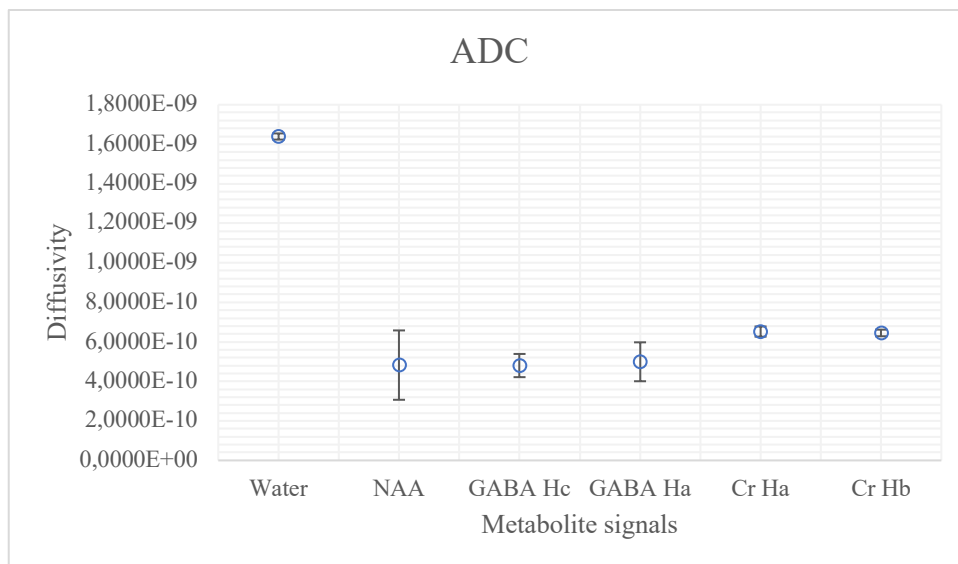
Experiment 19 – GABA/NAA/Cr Op3

Metabolite	Molarity (mmol/L)
NAA	13,16
Cr	10,06
GABA	8,03

Signal	Interval (ppm)	ADC	SE	R2	Adj. R2	Outliers removed
Water	(4.65-4.75)	1,6237E-09	5,4775E-11	0,995	0,994	None
NAA	(1.85-1.95)	5,1579E-10	4,0555E-12	1,000	1,000	None
GABA Hc	(2.1-2.25)	6,3064E-10	5,1038E-12	1,000	1,000	None
GABA Ha	(2.85-2.95)	6,3484E-10	5,2687E-11	0,973	0,966	None
Cr Ha	(3.75-3.85)	6,5105E-10	1,2955E-11	0,998	0,998	None
Cr Hb	(2.85-2.95)	6,1572E-10	1,0212E-11	0,999	0,999	None
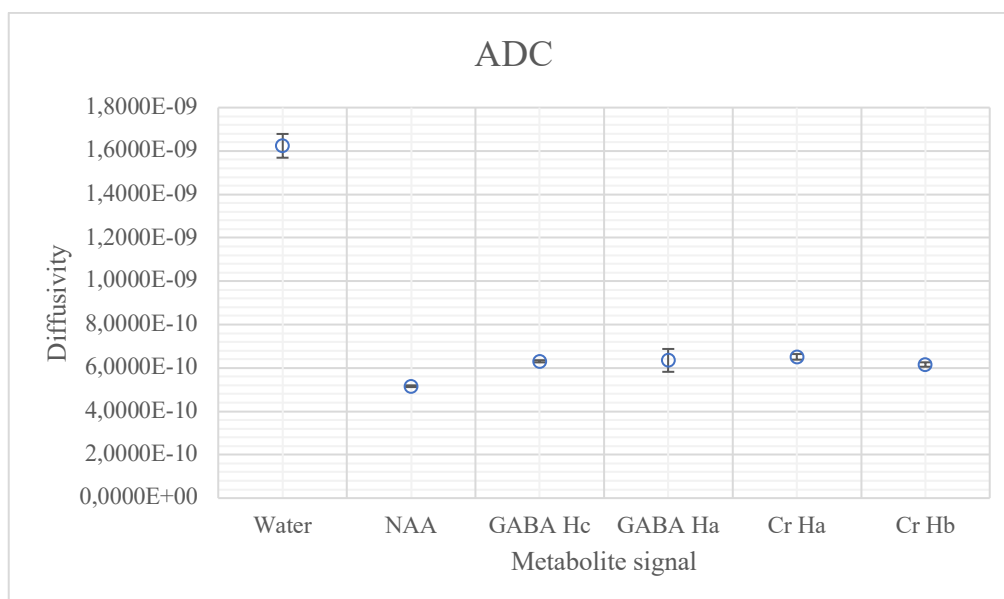
Experiment 20 - GABA/NAA/Cr Op4

Signal	Interval (ppm)	ADC	SE	R2	Adj. R2	Outliers removed
Water	(4,65-4,75)	1,7826E-09	3,5056E-11	0,998	0,998	None
NAA	(1.85-1.95)	5,2154E-10	5,7675E-12	1,000	0,999	None
GABA Hc	(2.1-2.25)	5,4987E-10	2,2575E-11	0,993	0,922	None
GABA Ha	(2.85-2.95)	6,9847E-10	2,8624E-11	0,993	0,992	None
Cr Ha	(3.75-3.85)	6,6113E-10	6,7540E-12	1,000	0,999	None
Cr Hb	(2.85-2.95)	6,4427E-10	7,1855E-12	1,000	0,999	None
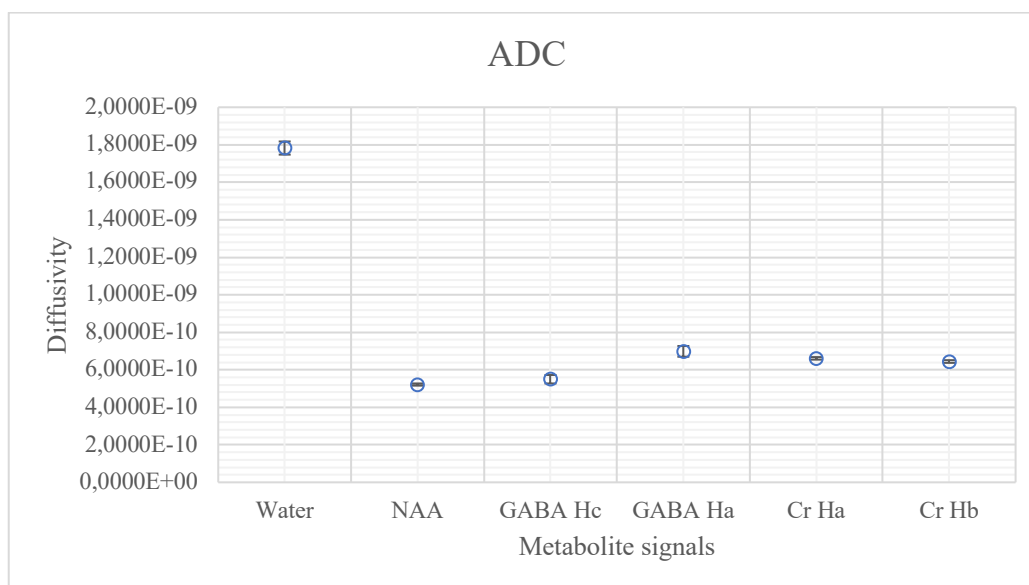
Experiment 21 - GABA/NAA Op2

Metabolite	Molarity (mmol/L)
NAA	12,68
GABA	9,58

Signal	Interval (ppm)	ADC	SE	R2	Adj. R2	Outliers removed
Water	(4.65-4-75)	1,4354E-09	5,4967E-11	0,994	0,993	None
NAA	(1.85-1.95)	5,1463E-10	7,8331E-12	0,999	0,999	None
GABA Hc	(2.1-2.25)	6,3373E-10	5,8699E-12	1,000	1,000	6
GABA Ha	(2.85-2.95)	6,8266E-10	2,7177E-11	0,994	0,992	None
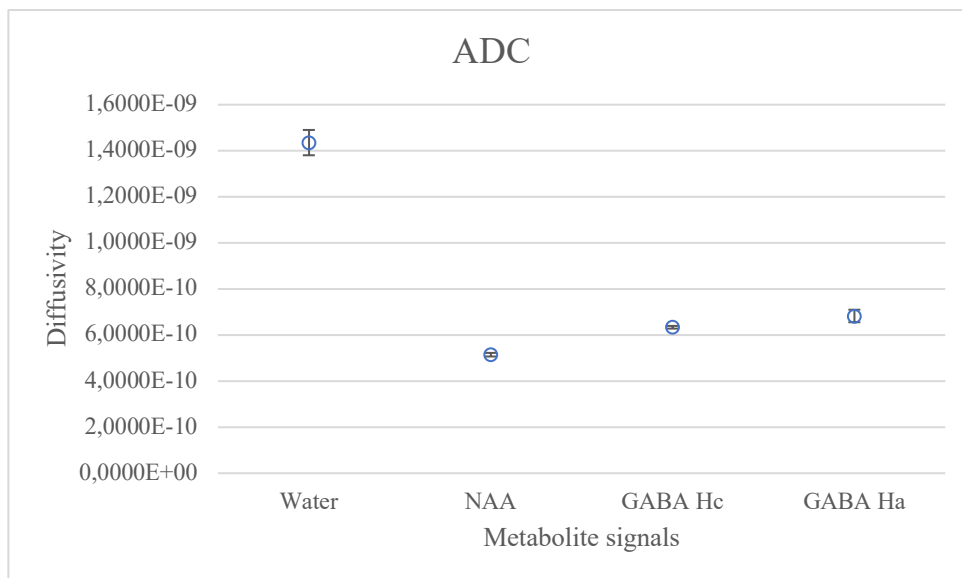
Experiment 22 – GABA/NAA Op3

Signal	Interval (ppm)	ADC	SE	R2	Adj. R2	Outliers removed
Water	(4.65-4-75)	1,6234E-09	1,6175E-11	1,000	1,000	2, 6
NAA	(1.85-1.95)	5,1298E-10	5,4061E-12	1,000	1,000	None
GABA Hc	(2.1-2.25)	6,4026E-10	1,0276E-11	0,999	0,999	None
GABA Ha	(2.85-2.95)	6,3068E-10	2,3413E-11	0,996	0,995	6